A Study Of Impact Parameters in the Channel $Z^0 \to \tau^+\tau^- \to e^\pm\nu_e\mu^\mp\bar{\nu}_\mu\nu_\tau\bar{\nu}_\tau$ from $p\bar{p}$ Collisions at $\sqrt{s} = 1.96$ TeV at DØ

Simon J.H. Dean

2004

THE UNIVERSITY
of MANCHESTER

Particle Physics Group

Department of Physics and Astronomy

A thesis submitted to The University of Manchester for the degree of

Doctor of Philosophy in the Faculty of Science and Engineering

Contents

List of Figures

List of Tables

Abstract

In this thesis, work undertaken on the DØ Silicon Microstrip Tracker is described before a study of signed impact parameters in the channel $Z^0 \to \tau^+\tau^- \to e^{\pm}\nu_e\mu^{\mp}\bar{\nu}_\mu\nu_\tau\bar{\nu}_\tau$ is presented. The performance of the Silicon Microstrip Tracker is demonstrated to be good for devices unaffected by grassy noise, which is shown to affect the performance of F-wedges in particular. Merged clusters are shown to cause problems in tracking. A study of signed impact parameters in the channel $Z^0 \to \tau^+\tau^- \to e^{\pm}\nu_e\mu^{\mp}\bar{\nu}_\mu\nu_\tau\bar{\nu}_\tau$ is presented. The matrix method is used to estimate the distributions of p_T and the absolute sum of signed impact parameters in signal $Z^0 \to \tau^+\tau^- \to e^{\pm}\nu_e\mu^{\mp}\bar{\nu}_\mu\nu_\tau\bar{\nu}_\tau$ events. The absolute sum of signed impact parameters is shown to be a reasonable lifetime-based discriminating variable for τ events. Using 141.4 pb^{-1} of data collected at DØ at $\sqrt{s} = 1.96$ TeV between 4th October 2002 and 7th September 2003, the production cross-section of the Z^0 boson multiplied by the branching fraction to two τs is measured in the channel $Z^0 \to \tau^+\tau^- \to e^{\pm}\nu_e\mu^{\mp}\bar{\nu}_\mu\nu_\tau\bar{\nu}_\tau$ to be

$$\sigma(p\bar{p} \to Z^0).\mathrm{Br}(Z^0 \to \tau^+\tau^-) = (319 \pm 66(\mathrm{stat.}) \pm 98(\mathrm{syst.}) \pm 21(\mathrm{lum.})) \text{ pb}$$

This measurement constitutes a test of the structure functions of the proton.

Declaration

No portion of the work referred to in this thesis has been submitted in support of an application for another degree or qualification of this or any other university or other institute of learning.

Copyright in text of this thesis rests with the Author. Copies (by any process) either in full, or of extracts, may be made only in accordance with instruction given by the Author and lodged in the John Rylands University Library of Manchester. Details may be obtained from the Librarian. This page must form part of any such copies made. Further copies (by any process) of copies made in accordance with such instructions may not be made without the permission (in writing) of the Author.

The ownership of any intellectual property rights which may be described in this thesis is vested in the University of Manchester, subject to any prior agreement to the contrary, and may not be made available for use by third parties without the written permission of the University, which will prescribe the terms and conditions of any such agreement.

Further information on the conditions under which disclosures and exploitation may take place is available from the Head of the Department of Physics and Astronomy.

Acknowledgements

Dedicated to Anne Robinson (1950–2004)

Your laughter will remain with us forever

Chapter 1

Introduction

The work presented in this thesis took place at the DØ experiment in the Fermi National Accelerator Laboratory (FNAL) in the USA. After a brief account of the current best description of particle physics, the Standard Model, the following chapters describe the apparatus used (Chapter 2) and work done in two main areas.

Chapter 3 presents service work undertaken with the DØ Silicon Microstrip Tracker (SMT) that took place between September 2001 and February 2003. The SMT event display described in Section 3.4 was created by Gavin Hesketh [1] and was maintained and developed by the author. All other work presented in Chapter 3 was originated by the author, including the creation and development of the SDAQ Browser mentioned in Section 3.3.

Chapters 4, 5 and 6 present work undertaken between February 2003 and September 2004 to investigate lifetime effects in τ events using signed impact parameters. This involves precise vertex measurements and follows on well from the work done on the SMT. As part of the signed impact parameters study, a first measurement of $\sigma(p\bar{p} \to Z^0).\mathrm{Br}(Z^0 \to \tau^+\tau^-)$ in the channel $Z^0 \to \tau^+\tau^- \to e^\pm \nu_e \mu^\mp \bar{\nu}_\mu \nu_\tau \bar{\nu}_\tau$ is presented.

1.1   The Standard Model

The Standard Model is a gauge theory that provides the current best description of the fundamental particles and their interactions. It is based on the group $SU(3)_C \otimes SU(2)_L \otimes U(1)_Y$ and takes into account the theories of electroweak and strong interactions. What follows is a brief overview of the Standard Model and the interested

16

reader is directed to [2], [3] and [4] for more information.

Fermions				Charge
Leptons	$\begin{pmatrix} e^- \\ \nu_e \end{pmatrix}$	$\begin{pmatrix} \mu^- \\ \nu_\mu \end{pmatrix}$	$\begin{pmatrix} \tau^- \\ \nu_\tau \end{pmatrix}$	-1 0
Quarks	$\begin{pmatrix} u \\ d \end{pmatrix}$	$\begin{pmatrix} c \\ s \end{pmatrix}$	$\begin{pmatrix} t \\ b \end{pmatrix}$	$+\frac{2}{3}$ $-\frac{1}{3}$

Table 1.1: The fundamental fermions of the Standard Model.

The fundamental particles are assumed to be point-like and have no internal structure. Other particles observed are then assumed to be composite objects made from different configurations of these fundamental particles. There are twelve fundamental spin-$\frac{1}{2}$ fermions in the Standard Model; six leptons and six quarks. These are given in Table 1.1. As shown, the leptons and quarks are separated into three 'generations' which have similar properties apart from the particle masses. The charges shown are expressed in multiples of the electron charge $e = 1.602 \times 10^{-19}$ C. Every particle in Table 1.1 has a corresponding antiparticle whose quantum numbers are of opposite sign.

The interactions between particles are mediated by the exchange of spin 1 gauge bosons. These interactions are described in the following sections.

1.1.1 The Electroweak Theory

Quantum Electrodynamics (QED) is the quantum theory describing electromagnetic interactions between particles. The mediating gauge boson in QED is the charge neutral photon (γ) which couples to electric charge. QED has an infinite range because the γ is massless.

The weak interaction is a force mediated by the three vector bosons W^+, W^- and Z^0, where the superscript indicates the charge held by each. The Ws have measured masses of (80.425 ± 0.038) GeV/c^2 and the Z^0 has a measured mass of (91.1876 ± 0.0021) GeV/c^2 [5], restricting the weak interaction to short range. The three vector bosons couple to all fermions as well as themselves.

The electroweak theory unifies QED and the weak interaction by considering the group $SU(2)_L \otimes U(1)_Y$. The weak interaction violates parity as evidenced by the fact that neutrinos are only observed in left-handed helicity states. The electroweak theory deals with this by describing left-handed fermions in $SU(2)_L$ isospin doublets and right-handed fermions in isospin singlets.

The electroweak theory is a gauge theory, where conserved quantities are the result of invariance under space-time transformations. This gauge invariance demands that the force-mediating bosons are massless, contrary to observation. The Higgs mechanism is a formalism that allows the bosons to inherit mass by spontaneous symmetry breaking. This introduces a new field which, in addition to producing the mass of the fundamental particles, leads to a neutral spin-0 boson. There has yet to be an experimental confirmation of the existence of the Higgs boson.

1.1.2 The Strong Interaction

Quantum Chromodynamics (QCD) is the quantum theory describing the strong interaction based on the gauge group $SU(3)_C$. The eight mediating bosons in QCD are called gluons and they couple to 'colour', a quantum number that can take the values red (r), green (g) and blue (b). Quarks take a single colour value while the gluons themselves carry a colour-anticolour combination. Leptons do not interact via the strong interaction as they do not possess colour. Gluons are massless and, like photons, therefore have an infinite range of interaction. Unlike photons, however, gluons can interact with other gluons leading to the properties of 'colour confinement' and 'asymptotic freedom'. Colour confinement is the confinement of quarks to bound hadronic states due to the fact that observed quark states must be 'colourless', implying the combination rgb or $\bar{r}\bar{g}\bar{b}$ for baryons and $r\bar{r}$, $g\bar{g}$ or $b\bar{b}$ for mesons. This effect does not allow free quarks to be observed in nature. Asymptotic freedom comes from the fact that the strong interaction is stronger between quarks that have a greater separation. Quarks therefore act as though free at very small separations.

1.1.3 Relevant Processes

The process $Z^0 \rightarrow \tau^+\tau^- \rightarrow e^\pm \nu_e \mu^\mp \bar{\nu}_\mu \nu_\tau \bar{\nu}_\tau$ is of particular interest in this analysis. For ease of reading, the neutrinos will be left out of further references to this process. The underlying interactions for $Z^0 \rightarrow \tau^+\tau^- \rightarrow e^\pm \mu^\mp$ are represented by Feynman diagrams in Figures 1.1 and 1.2. Feynman diagrams are visual representations of particle physics processes with space and time expressed on separate axes. For the diagrams shown here, space is along the vertical axis and time is along the horizontal axis. Feynman diagrams are also useful mathematical tools. The lines and vertices on a Feynman diagram represent mathematical terms that can be combined to construct the amplitude of the featured process. This amplitude can then be used to calculate the decay rate or scattering cross-section.
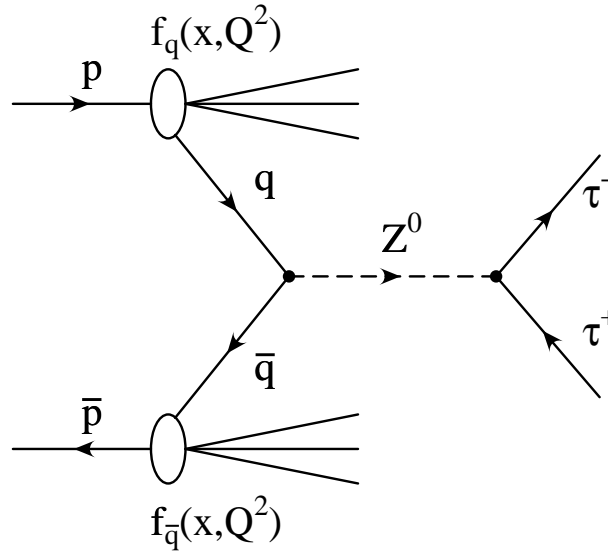
Figure 1.1: Feynman diagram showing the process $q\bar{q} \rightarrow Z^0 \rightarrow \tau^+\tau^-$ produced in a $p\bar{p}$ collision.

Figure 1.1 shows a $p\bar{p}$ interaction producing the process $q\bar{q} \rightarrow Z^0 \rightarrow \tau^+\tau^-$. This involves the annihilation of a quark-antiquark pair to produce a Z^0 boson. The Z^0 then decays to produce a pair of τ leptons. The colliding protons and antiprotons contain the valence quarks uud and $\bar{u}\bar{u}\bar{d}$ respectively. The overall structure of the proton and antiproton are represented mathematically by structure functions based on the Parton Distribution Functions (PDFs). The contribution of PDFs are indicated in Figure 1.1.

The removal of the quark from the proton causes the remainder of the proton (the

'proton remnant') to hadronise. Hadronisation involves the production of quarks and gluons from energy fluctuations which then form into hadrons. These groups of hadrons are collimated in the direction of the original quarks in the proton and are called 'jets'. This explanation is also true of antiquarks in antiprotons. The jets from the proton remnant are produced mainly in the forward region of the DØ detector, although jets in the central region of the detector are also very common. These jets often come from gluons radiated in the $p\bar{p}$ interaction. Such events are referred to as 'QCD' events in the rest of this thesis.
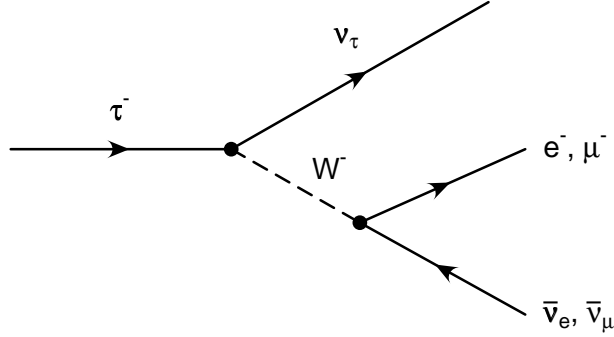
Figure 1.2: Feynman diagram showing the process $\tau^- \to l^- \bar{\nu}_l \nu_\tau$.

Figure 1.2 shows the weak decay of a τ^- lepton to a τ neutrino, producing either an electron or a muon and the corresponding neutrino via an intermediate W boson. This decay happens for both of the τ leptons in Figure 1.1 to produce two charged leptons in the final state.

Chapter 2

Experimental Apparatus

The work presented in this thesis makes use of data collected in the DØ detector. DØ is provided with $p\bar{p}$ collisions with a centre-of-mass energy of 1.96 TeV by the Tevatron accelerator. The Tevatron is currently the world's highest energy accelerator and will remain so until the Large Hadron Collider (LHC) begins operating in 2007. The physics program at DØ is therefore full of opportunities to make important contributions to the worldwide physics effort in fields such as top, bottom and electroweak physics. The high centre-of-mass energy also provides a good platform for observing new phenomena and Higgs processes.

The following sections provide more information about the Tevatron (Section 2.1) and the DØ detector (Section 2.2).

2.1   The Tevatron Accelerator

The Tevatron provides the final stage of a multi-stage process to accelerate protons and antiprotons to an energy of 980 GeV. Antiprotons are also produced during the process and accelerated to an energy of 980 GeV. The full process is illustrated in Figure 2.1. The stages of acceleration are as follows [6],[7]:

Cockcroft-Walton The Cockcroft-Walton accelerator ionizes hydrogen by adding electrons to neutral hydrogen atoms. The resulting negative charge allows the ions to be accelerated to 750 keV before being passed to the Linac.

LINAC The **LIN**ear **AC**celerator is approximately 130 m long and accelerates the
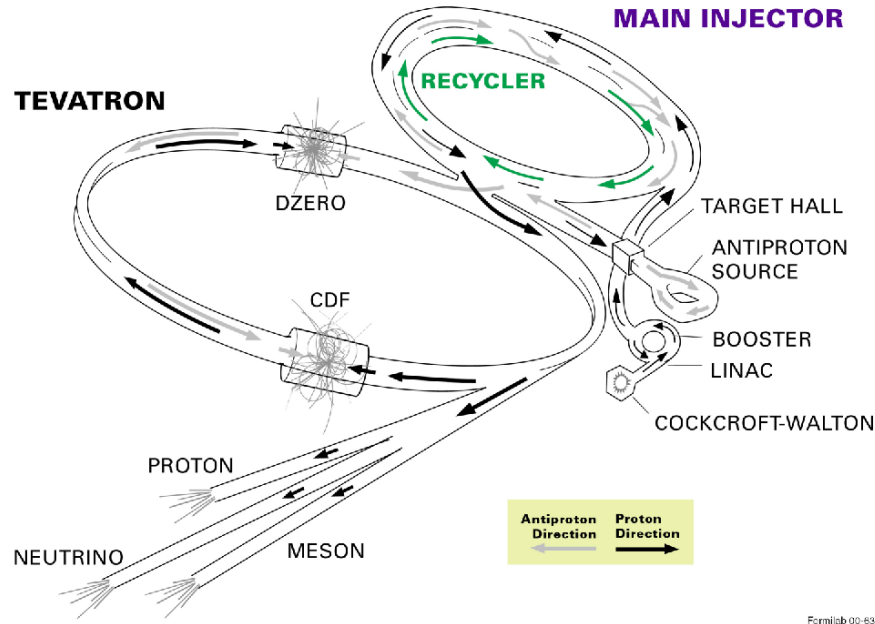
Figure 2.1: Schematic drawing of the accelerator chain at FNAL.

hydrogen ions to 400 MeV by means of an oscillating electric field. The ion beam is shielded from the electric field for half of each phase, allowing acceleration in only one direction. After acceleration, the beam is passed through a carbon foil to remove the two electrons from each ion, leaving only the proton.

Booster The Booster is a synchrotron with a circumference of 475 m that accelerates protons to an energy of 8.9 GeV.

Main Injector The Main Injector is a circular accelerator that takes 8.9 GeV protons from the Booster and accelerates them to 150 GeV. Before they are fully accelerated, some of the protons are extracted at 120 GeV and sent to the Antiproton Source.

Antiproton Source The Antiproton Source is a combination of devices to produce antiprotons. 120 GeV protons are received from the Main Injector and fired at a nickel target. Among the many products are antiprotons, which are focussed at 8.9 GeV. These antiprotons are kept in a storage ring called the Antiproton Accumulator and stochastically cooled before injection into the Main Injector after sufficient antiprotons have been collected. The Main Injector then accelerates

the antiprotons to 150 GeV.

Recycler The Recycler is a storage ring in the same beam tunnel as the Main Injector that is used to store antiprotons. Protons are more readily available than antiprotons so it is important to keep antiproton production rates high. This is achieved by emptying the antiprotons from the Antiproton Accumulator into the Recycler when it reaches capacity. These antiprotons are stored at 8.9 GeV and then accelerated to 150 GeV by the Main Injector for injection into the Tevatron when required.

Tevatron The Tevatron receives 150 GeV protons and antiprotons from the Main Injector or the Recycler and accelerates them to 980 GeV. It has a radius of 1 km and uses superconducting bending magnets. Conventional magnets dissipate electrical power due to their resistance so a lot of power is saved in the Tevatron by using superconductors. When viewed from above, protons travel clockwise around the Tevatron while antiprotons travel anti-clockwise.

Once beams of 980 GeV protons and antiprotons have been produced, they are focussed together at specified collision points. The DØ detector is built around one such collision point. The resulting $p\bar{p}$ interactions are detected and analysed.

The proton and antiproton beams in the Tevatron have a structure containing three 'superbunches' per rotation. Each superbunch contains 12 bunches separated by 396 ns. The superbunches are separated by gaps of 2.2 μs. The Tevatron is designed to provide a luminosity of 2×10^{32}cm^{-2}s^{-1} in Run II.

2.2 The DØ Detector

The DØ detector is a general purpose detector designed for exploring physics from $p\bar{p}$ collisions at the Tevatron energy scale. It combines a wide angular coverage with good identification of electrons, muons, jets and missing transverse energy ($\not{E}_{\mathrm{T}}$) and good tracking and vertexing. The layout of the detector is shown in Figure 2.2.

Moving outwards from the interaction point, particles experience the central tracker, the preshower detectors, the calorimeters and the muon detectors. These are described in the following sections, but it is useful first to define the coordinate system used at

23
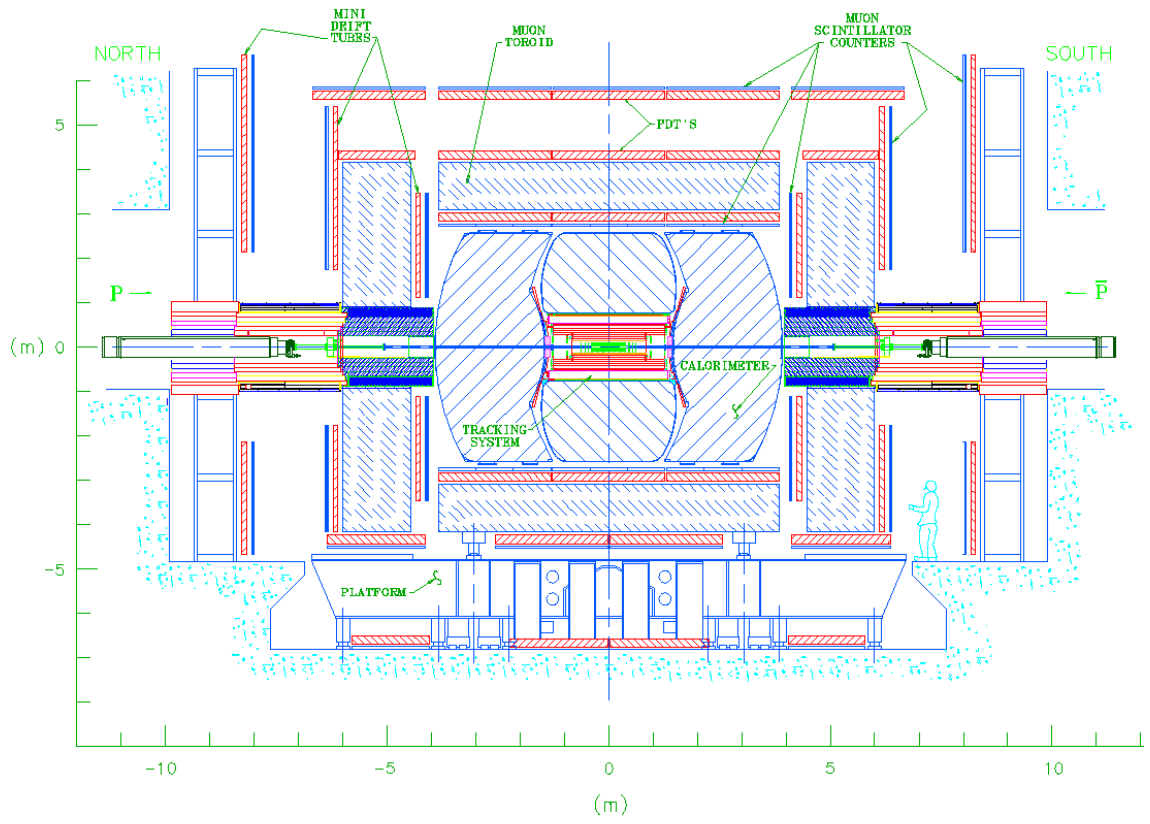
Figure 2.2: Cross-section of the DØ detector in the rz-plane.

DØ. A right-handed coordinate system is used with the positive z-axis defined along the proton beam direction (pointing to the right in Figure 2.2). The x-axis is defined in the direction towards the centre of the Tevatron ring. The rapidity of a particle is defined as

$$\tanh^{-1}\left(\tfrac{p_z}{E}\right)$$

where p_z is the z-component of momentum and E is the total particle energy. Rapidity is a useful quantity because it changes by a constant amount under a Lorentz boost so rapidity differences between particles are relativistically invariant. The pseudorapidity, η, is an approximation to rapidity and is defined as

$$\eta = -\ln\,\tan(\tfrac{\theta}{2})$$

where θ is the polar angle given by

$$\theta = \tan^{-1}(\tfrac{\sqrt{x^2+y^2}}{z})$$

The transverse momentum (p_T) is a quantity used very often in particle physics. The transverse momentum is given by

$$p_{\mathrm{T}} = \sqrt{p_x^2 + p_y^2}$$

where p_x and p_y are the components of momentum in x and y respectively.

2.2.1 The DØ Central Tracker

The central tracker is the innermost component of the DØ detector and provides precision p_{T} measurement for charged particles. Figure 2.3 illustrates the different components of the central tracker.
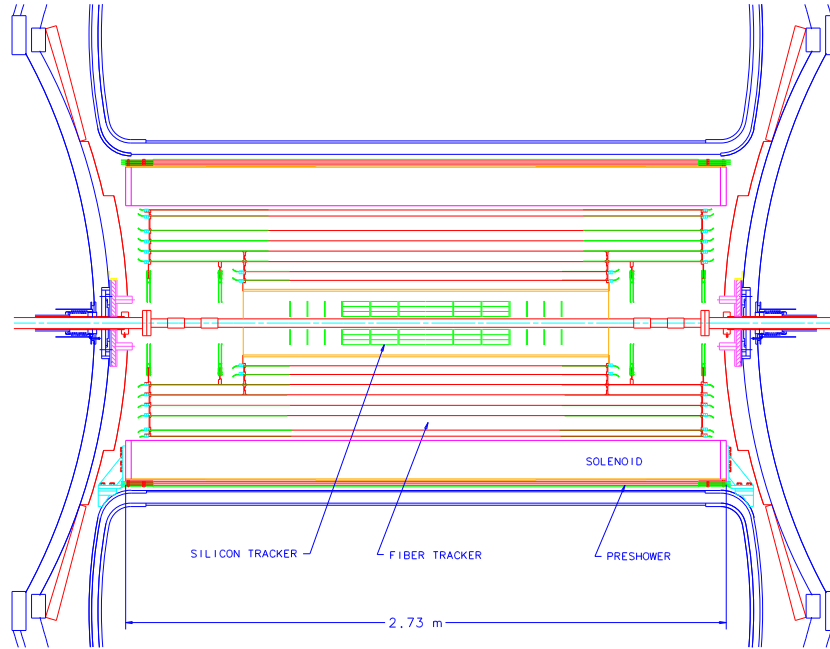
Figure 2.3: Cross-section of the DØ central tracker in the rz-plane.

A superconducting solenoid magnet surrounds the central tracker and immerses it in a 2 Tesla magnetic field to cause bending of charged particle trajectories in the $r\phi$ plane. The Silicon Microstrip Tracker (SMT) is located next to the beampipe and provides precise measurements of charged particles close to the interaction point in each event. The SMT has coverage out to an η of roughly 3 and is described in detail in Chapter 3. The Central Fibre Tracker (CFT) surrounds the SMT and is decribed in the following section. The SMT and CFT combine to measure tracks in the central tracking volume.

Central Fibre Tracker

The CFT [8] consists of eight concentric cylindrical superlayers with radii between roughly 20 cm and roughly 50 cm. Each superlayer contains two doublet layers of scintillating fibres. The inner doublet layer in each superlayer contains fibres arranged parallel to the z-axis (the 'axial' direction.) The fibres in the outer doublet layer in each superlayer are arranged at an angle of $\pm 2°$ to the axial fibres depending on the superlayer. This provides stereo information to allow measurement in the z direction.

Each scintillating fibre has a radius of 835 μm and a length of 1.66 m in the two inner superlayers or 2.52 m in the six outer superlayers. The fibres are each connected via a clear fibre waveguide to a Visible Light Photon Counter (VLPC). The pitch of the scintillating fibres is in the range 900–1000 μm and when the information from both doublet layers in a superlayer are combined, a position resolution of order 100 μm is achieved.

The CFT contains approximately 77,000 scintillating fibres and has coverage over the range $|\eta| < 2$.

2.2.2   DØ Preshower Detectors

The preshower detectors at DØ ([10],[11]) work as both trackers and sampling calorimeters. The Central Preshower (CPS) detector covers the range $|\eta| < 1.2$ while the Forward Preshower (FPS) detector provides additional coverage in the range $1.4 < |\eta| < 2.5$.

The position of the CPS is indicated in Figure 2.3. The CPS is cylindrical and sits outside the solenoid at a radius of roughly 70 cm. Just before the CPS, a lead absorber is added to give a combined total of two radiation lengths of material with the solenoid. The CPS itself consists of three layers of scintillating strips, each of which is read out via a wavelength-shifting fibre to a VLPC. The inner radial layer consists of axial strips while the two outer layers have stereo strips at roughly $+23°$ and $-23°$. This configuration enables precise position measurement for tracking but also measures particle showers from the solenoid and lead absorber combination. Energy measurements and particle identification are therefore also possible.

The FPS is located in the forward region and is disk-shaped. It consists of wedge-shaped modules arranged uniformly in ϕ. The FPS has two inner layers of scintillating strips at stereo angles of $+11.25°$ and $-11.25°$ to give a relative offset of $22.5°$. At slightly higher z is a layer of lead absorber that provides 2 radiation lengths of material before two outer layers of scintillating strips. These have the same stereo properties as the two inner layers. As with the CPS, the strips are each read out using a wavelength-shifting fibre connected to a VLPC. Precise position measurement and shower sampling are also possible with the FPS.

2.2.3 Calorimetry at DØ

The DØ calorimeters [12] are liquid argon sampling calorimeters and provide excellent coverage in η. The liquid argon is housed in three cryostats, each weighing about 300 metric tons in total and containing roughly 15,000 litres (about 26 metric tons) of liquid argon. The arrangement of the cryostats can be seen in Figure 2.2. One cryostat surrounds the central tracker in radius and contains the Central Calorimeter (CC). The two remaining cryostats are in the forward regions and contain the two End Calorimeters (ECs).

The CC has three concentric regions of calorimeter cells. Working outwards from the beampipe, these are the electromagnetic, fine-hadronic and coarse-hadronic regions. The ECs have an electromagnetic region close to the beampipe at low $|z|$, covering the region $1.4 < |\eta| < 4.1$. The rest of the ECs are composed of a mixture of fine-hadronic cells closer to the DØ origin and coarse-hadronic cells further away, taking the coverage out to $|\eta| < 5.2$.

Electromagnetic cells and fine-hadronic cells both contain uranium absorber plates. These have a thickness of 3–4 mm in the electromagnetic cells and a thickness of 6 mm in the fine-hadronic cells. The coarse-hadronic cells in the CC contain copper absorber plates while the coarse-hadronic cells in the ECs contain steel absorber plates. Both copper and steel absorber plates have a thickness of 47 mm. The absorber plates are aligned parallel to the beampipe in the CC and mostly perpendicular to the beampipe in the ECs. Throughout the calorimeters, the absorber plates are grounded and interspersed with signal boards that have a high voltage applied. This sets up an electric field that causes charge from ionisation in the liquid argon to drift onto the

signal boards. The charge is then read out and used to calculate the energy deposited in the calorimeter.
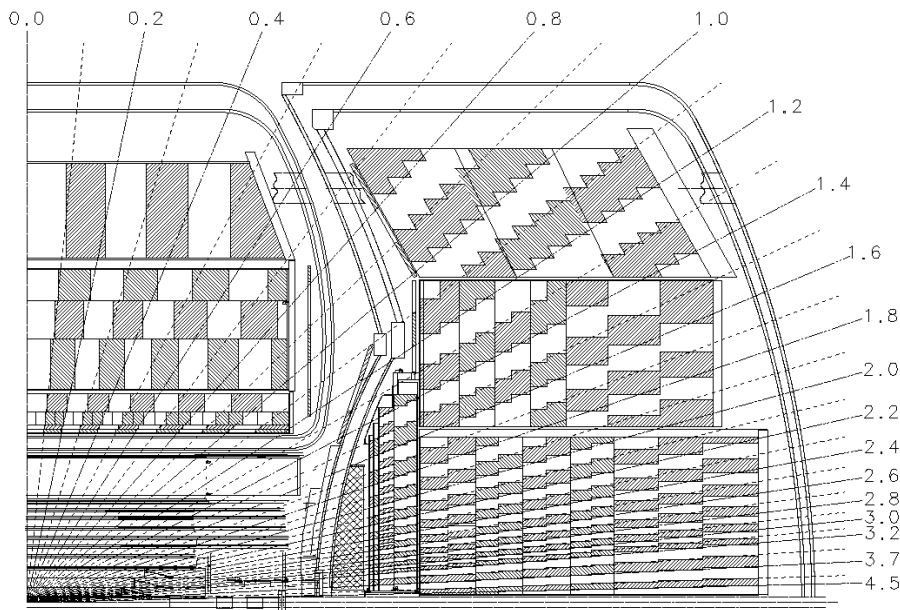
Figure 2.4: Schematic diagram of one quarter of the DØ calorimeter. The arrangement of calorimeter cells into projective towers in η is shown.

The calorimeter cells are arranged such that they form 'towers' projecting out from the DØ origin with a granularity of 0.1×0.1 rads in $\Delta\eta \times \Delta\phi$. This granularity can be seen in Figure 2.4. There are four layers of electromagnetic cells in both the CC and the ECs. The third electromagnetic layer has a granularity of 0.05×0.05 rads in $\Delta\eta \times \Delta\phi$ to improve the position resolution for photons and electrons. Depending on η, the calorimeter has 7–9 interaction lengths of material.

The gaps between the cryostats in the region $0.8 < |\eta| < 1.4$ (the 'inter-cryostat region') are problematic as the lack of instrumentation degrades the energy resolution. To deal with this, 'massless gaps' and the Inter-Cryostat Detector (ICD) are employed. The massless gaps are actually signal boards with no accompanying absorber plates located close to the surface of the cryostat in the inter-cryostat region. The ICD consists of scintillating tiles located in the gap between the cryostats in the inter-cryostat region. Both the massless gaps and the ICD help to sample the energy lost by particles travelling through the inter-cryostat region.

Tests with single-particle beams of electrons and pions were performed during Run I to measure the electromagnetic and hadronic response of the calorimeter [9]. The

energy resolution was found to be of the form

$$\left(\frac{\sigma}{E}\right)^2 = \left(\frac{N}{E}\right)^2 + \frac{S^2}{E} + C^2$$

where E and σ are the energy and associated uncertainty of an incident particle and N, S and C are noise, sampling and constant terms respectively. The tests with electrons yielded values of N $=$ 0.14 GeV, S $=$ 0.135 $\sqrt{\text{GeV}}$ and C $=$ 0.014, while the tests with pions yielded values of N $=$ 1.3 GeV, S $=$ 0.41 $\sqrt{\text{GeV}}$ and C $=$ 0.032. The calorimeter electronics were replaced for Run II and a new calibration was found for the electromagnetic calorimeter by looking at $Z^0 \rightarrow e^+e^-$ data [37]. The parameters obtained were N $=$ 0.29 GeV, S $=$ 0.15 $\sqrt{\text{GeV}}$ and C $\simeq$ 0.04.

2.2.4   The DØ Muon System

The layout of the DØ muon system [10] is shown in Figure 2.2. In the central ($|\eta| < 1$) and forward ($1 < |\eta| < 2$) regions, there are three layers labelled A, B and C working outwards from the DØ origin. There is a toroidal magnet system between the A and B layers that bends tracks in the rz-plane. This enables momentum measurement for charged particles crossing the muon detectors by using the A-layer and the central tracker to calculate the particle direction before encountering the magnetic field and using the B and C layers to calculate the particle direction afterwards. The resulting track measured locally in the muon system is referred to as a 'local muon'.

In the central region, all three layers contain Proportional Drift Tubes (PDTs). Each PDT contains an anode wire which collects drifting charge produced by an incident charged particle. Position measurements can be made both transverse and longitudinally to the wire by looking at the timing information from collected charge. The A and C layers also contain scintillator counters. The scintillators in the C layer do not yield particularly good position information but are used for timing information during triggering. The scintillators in the A layer have a size of $0.2 \times 4.5°$ in $\Delta\eta \times \Delta\phi$. Underneath the central muon system, some areas are uninstrumented due to mechanical supports for the detector. Where possible, there are additional scintillators in the B layer to compensate for this loss.

In the forward region, all three layers contain Mini-Drift Tubes (MDTs). MDTs are much narrower than PDTs making the drift time much smaller. They are arranged

perpendicular to the beampipe with the anode wires roughly following the magnetic field lines around the beampipe. This gives the PDTs a position resolution of approximately 350 μm in r for good η measurement. All three layers also have scintillator counters in the forward region. These are finely segmented with a size of $0.1 \times 4.5°$ in $\Delta\eta \times \Delta\phi$.

As muons are minimum ionising particles, the muon system works on the principle that they are the only charged particle that can escape the calorimeters and be detected. Proton and antiproton fragments at high $|\eta|$ can interact with the calorimeter casing or the beampipe itself to produce charged particles that register in the forward muon detectors. For this reason, shielding is placed around the beampipe between the calorimeters and the accelerator tunnel in z.

2.2.5   The DØ Luminosity Monitor

The DØ Luminosity Monitor (LM) [16] is used to accurately determine the amount of total integrated luminosity collected during data-taking. It consists of two arrays of 24 scintillator wedges arranged uniformly in ϕ around the beampipe at $z = \pm140$ cm and provides coverage in the range $2.7 < |\eta| < 4.4$. Charged particles in proton or antiproton remnants create signals in the scintillators which are used to calculate timing information. Coincident signals from both arrays indicate an inelastic $p\bar{p}$ collision. An approximate primary vertex z-position can also be calculated by comparing times from both scintillator arrays. By counting $p\bar{p}$ collisions, the LM determines the integrated luminosity of 'luminosity blocks', periods of data-taking of 60 s or less. Luminosity blocks are categorised as good or bad to indicate whether or not they can be correctly normalised to give an accurate integrated luminosity [14]. The LM currently gives an uncertainty of 6.5% [15] on the integrated luminosity of good luminosity blocks.

2.2.6   The DØ Trigger System

It is unfeasible to record all of the roughly 2 million events produced per second during data-taking at DØ. The trigger system [13] is a three-stage process of identifying and recording the most interesting fraction of these events by making fast physics decisions.

The Level 1 trigger takes information from the calorimeter, preshower detectors, CFT, muon system and Luminosity Monitor and takes up to 4.2 μs to make the decision to accept or reject an event. The Level 1 trigger accepts events at a rate of approximately 1.5 kHz. At Level 1, calorimeter cells are grouped together into trigger towers with a granularity of $\Delta\eta \times \Delta\phi = 0.2 \times 0.2$. Level 1 calorimeter decisions are then made locally based on the energy deposited in each trigger tower, or globally based on summed information from all towers. The total energy and missing transverse energy are examples of quantities that can be used in a global Level 1 calorimeter decision.

Level 1 decisions in the CFT are based on matching the output from the eight superlayers with expected hit patterns for tracks in different p_{T} ranges. This matching only uses axial hit information and the Level 1 CFT decisions are based on p_{T}, charge, isolation, ϕ and matching hits in the preshower detectors.

The Level 1 muon triggers are based on information from the scintillator and drift tube detectors. Scintillator hits can be used individually to make decisions at Level 1 whereas drift tube hits do not have accurate enough timing information to associate them to a particular event. They therefore require a matching scintillator hit. CFT trigger tracks can also be matched to Level 1 muons to provide p_{T} information. High p_{T} Level 1 muons can be rejected as cosmic ray muons using scintillator timing information.

The readout crates for each subdetector have buffer space to store Level 1 information for up to 32 events, allowing a decision time much larger than the bunch crossing time. After a Level 1 accept is issued, the event is stored in one of 16 event buffers to wait for a Level 2 decision.

At Level 2, the readout systems for the individual subdetectors contain preprocessors that refine the Level 1 information and send it to a global processor. This finds correlations between the separate trigger objects. An example of this is a Level 2 electron being found by matching track, preshower and calorimeter information. The Level 2 trigger system has a 100 μs decision time and an accept rate of 1 kHz.

At Level 3, events are reconstructed on a dedicated farm of CPUs using a fast version of the full offline event reconstruction. The full physics information for each event can therefore be used in a Level 3 trigger decision. The Level 3 trigger system has an accept rate of 50 Hz. When an event is accepted at Level 3, all digitized output from

the detector subsystems is saved to tape. The full offline reconstruction is then run on this detector output at a later stage.

There are two types of detector simulation employed in Monte Carlo at DØ. These are

Full Simulation The fully digitized detector output is simulated by modelling the DØ detector fully in GEANT and then simulating the readout response. The full offline event reconstruction is then applied to this output to measure physics objects.

Fast Simulation The measurement of physics objects is simulated by directly smearing generator-level information to reproduce detector effects. This is performed by the Parameterised Monte Carlo Simulation (PMCS) package and is much faster than the full detector simulation.

Chapter 3

The DØ Silicon Microstrip Tracker

As part of the DØ upgrade for Run II, the central tracking system was replaced to improve the overall physics capabilities of the detector. The innermost component of the Run II tracking system is the Silicon Microstrip Tracker (SMT). The SMT provides high resolution measurements close to the interaction point.
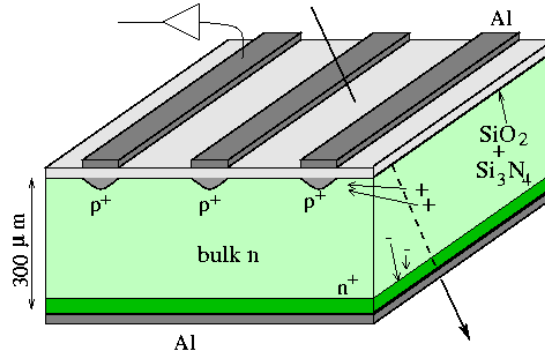
Figure 3.1: The layout of a single-sided silicon detector.

The SMT is composed of silicon microstrip detectors. A brief description of the physics of silicon microstrip detectors follows but for a more detailed explanation see [19]. A single-sided detector is a wafer of n-type silicon with implanted parallel strips of p^+-type silicon, as shown in Figure 3.1. The '+' denotes a much higher concentration of charge carriers than is usual in doped silicon. The strips are referred to as p-side strips. The resulting pn junctions have a high reverse voltage applied in order for the detector volume to become fully depleted. Single-sided detectors, as shown in Figure 3.1, have a uniform layer of n^+-type silicon on the opposite side of the wafer. The voltage is applied through this layer and the strips. The high density of charge

carriers means that the material remains conductive even when the detector is fully depleted. Biasing the strips sets up an electric field. Charged particles crossing the silicon create electron-hole pairs by ionisation. The holes drift onto the nearest strips and the collected charge is read out. The distribution of charge across the strips then indicates where the charged particle passed through the detector.

Double-sided detectors have strips of n^+-type silicon instead of a uniform layer. These collect the negative charge from the electrons and are referred to as n-side strips. The n-side strips are usually offset by a constant angle to the p-side strips so that information from both sides of the device can be combined for a 2 dimensional measurement. The offset angle is known as the stereo angle.

The silicon wafers used in the SMT are 300 μm thick and the silicon strips have a width of 10 μm. Charge carriers in silicon detectors have a high drift speed so the charge in an event can be collected very quickly. Silicon detectors are therefore ideal for use in Run II where the collision rate is high.

What follows is a more complete overview of the SMT. Section 3.1 provides a description of the SMT geometry. Section 3.2 then describes the system for reading out SMT data. Secondary Data Acquisition is introduced in Section 3.3 before the SMT event display is presented in Section 3.4. Some common causes of noise in the SMT are described in Section 3.5 and finally, a performance study for the SMT hardware is performed in Section 3.6.

3.1 Geometry

The design of the SMT incorporates the main physics goals of DØ during Run II. A detailed presentation of DØ physics in relation to the SMT design can be found in [17] but a brief summary is given here. The main physics goals include top physics studies at high transverse momentum and bottom physics and QCD studies at lower transverse momentum. These two different kinematic regimes place different requirements on the geometry of the SMT, which is shown in Figure 3.2.

The high mass of the top quark implies that narrow jets with a large number of tracks are produced in the central region of the detector. High position resolution for good track discrimination is therefore essential. b-jet identification is an important part of

34
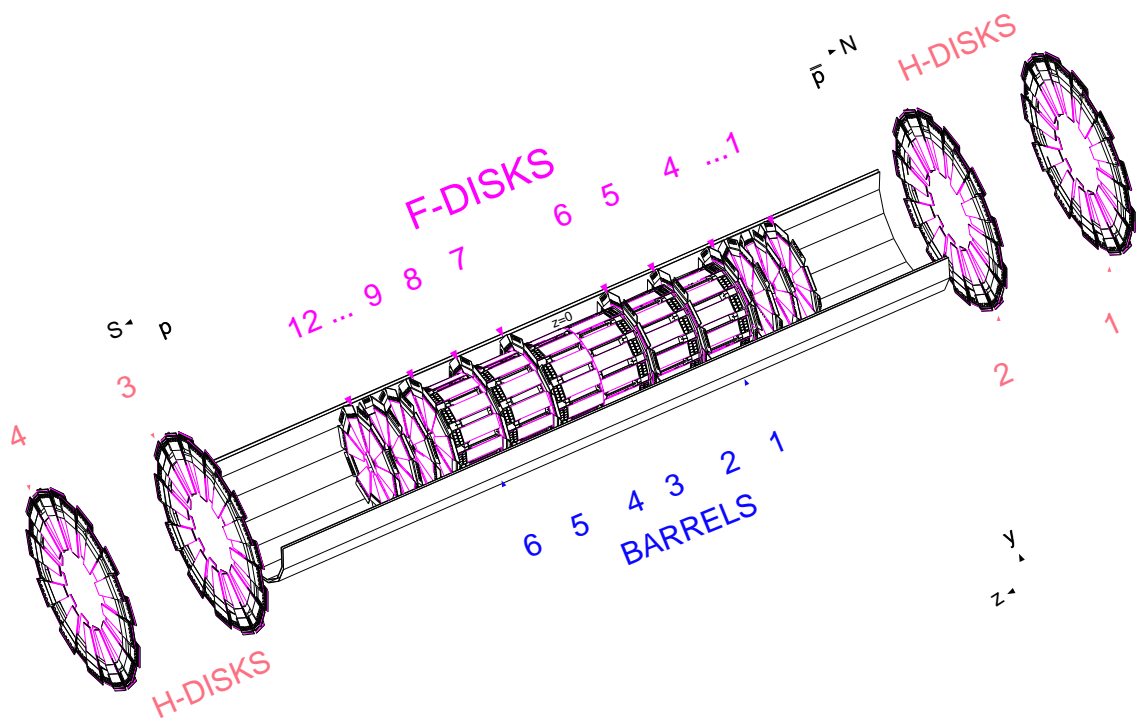
Figure 3.2: The geometry of the DØ SMT. The barrel, F-disk and H-disk regions are shown, extending out to $|z| < 38.4$ cm, $|z| < 54.8$ cm and $|z| < 120$ cm respectively.

top physics as top quarks decay primarily to bottom quarks in the Standard Model. Techniques for b-tagging involve secondary vertices and impact parameters, requiring high precision tracking in order to be used effectively.
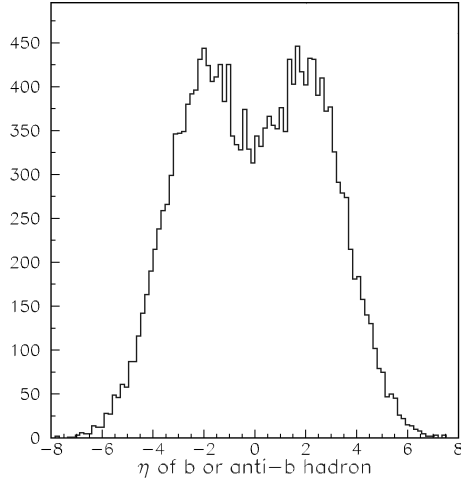
Figure 3.3: The production cross-section of B mesons as a function of η with arbitrary units on the vertical axis. The plot shows generator-level information from the Pythia event generator. Taken from [20].

B-physics studies typically make use of large event samples with tracks at much lower transverse momentum covering a wider angular region. Direct production of B-mesons extends out to high $|\eta|$ as shown in Figure 3.3, so good tracking for b-tagging in the forward region of the detector is also very important. B_s mixing studies heavily depend on lifetime measurements so good lifetime resolution is crucial. To achieve this, good 3-dimensional vertex reconstruction is used.

It is therefore clear that the design of the SMT must allow high resolution measurements over the full η acceptance of the DØ detector. An additional factor is the shape of the interaction region. When a charged particle crosses a silicon detector, the position measurement is most precise if the track is normal to the surface of the detector. This limits the spread of charge which minimises the width of the charge distribution on the strips. With a point-like interaction region, the SMT would ideally require a roughly spherical geometry to ensure normal incidence for tracks coming from the primary vertex. This could be approximated in practice by a hybrid geometry featuring a short barrel region at low $|\eta|$ with a disk structure covering the remaining angular space. The interaction region in the Tevatron actually has a Gaussian width of approximately 25 cm along the beam direction. This leads to the SMT geometry shown in Figure 3.2 where an elongated barrel structure surrounds the interaction region at low $|\eta|$ while an array of disks extends coverage out to $|\eta| \simeq 3$.

The barrels and disks are described in more detail in the next two sections. Detailed information about the layout of the SMT can be found by consulting [17],[22] and [23]

3.1.1 Barrels

The silicon detectors in the barrels are called ladders. The ladders are arranged so that p-side strips run parallel to the beam direction. This is called the axial direction. Each ladder consists of two pieces of 6 cm-long detector wire-bonded together for an active strip length of 11.7 cm. The p-side strips have a pitch of 50 μm which can provide a good position resolution of 10 μm or less. The n-side strips in double-sided ladders have a stereo angle of either 2° or 90°. 2° strips are set at a pitch of 62.5 μm while 90° strips have a pitch of 153.5 μm.

Ladders are arranged radially in layers as shown in Figure 3.4. The layout shown is drawn in the $r\phi$ plane. There are eight layers arranged evenly between radii of 2.7 cm
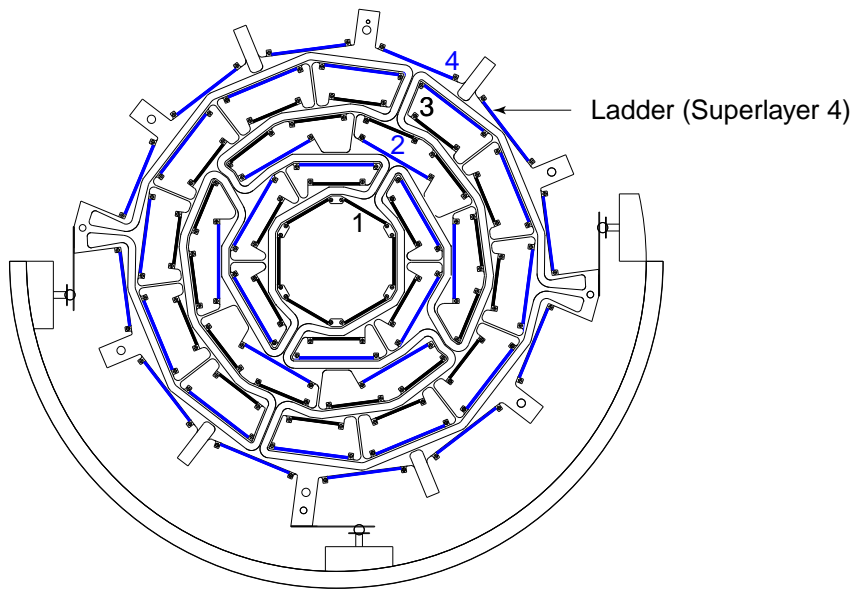
Figure 3.4: SMT barrel layout in the $r\phi$ plane. The silicon layers cover the radii 2.7–9.4 cm.

and 9.4 cm and are numbered from 1 to 8 with increasing radius. Each adjacent pair of layers is called a superlayer and provides complete angular coverage in ϕ. The superlayers are numbered 1 to 4 with increasing radius.

There are six SMT barrels in total. As shown in Figure 3.2, they are numbered from 1 to 6 going from the North end of the detector to the South end. Superlayers 2 and 4 in all barrels contain double-sided detectors with n-side strips at a stereo angle of $2°$. Superlayers 1 and 3 contain single-sided detectors in the two outer barrels (1 and 6) and double-sided detectors with n-side strips at a stereo angle of $90°$ in the four inner barrels (2 to 5).

It is useful to define a naming convention for ladders. References to specific ladders will be of the form

$$\text{B}barrel\text{ - }layer\text{ - }ladder$$

where *barrel* is the barrel number, *layer* is the layer number and *ladder* is the ladder number within the specified layer.

3.1.2 Disks

There are two types of disk in the DØ SMT. As shown in Figure 3.2 F-disks are placed at low $|z|$ and H-disks are further away from the interaction region. The detectors in both types of disk are called wedges and are positioned so as to be perpendicular to the beam direction. The wedges in F-disks and H-disks are referred to as F-wedges and H-wedges respectively.

F-wedges have a length of 7.5 cm with a width that varies from 1.7 cm to 5.7 cm. All F-wedges are double-sided detectors. The p-side strips have a pitch of 50 μm and are set at a stereo angle of $+15°$ with respect to the radial direction. The n-side strips have a pitch of 62.5 μm and have a stereo angle of $-15°$, which means the two sides have an effective stereo of 30° between them. The wedge shape of the detector means that the length of the silicon strips varies.
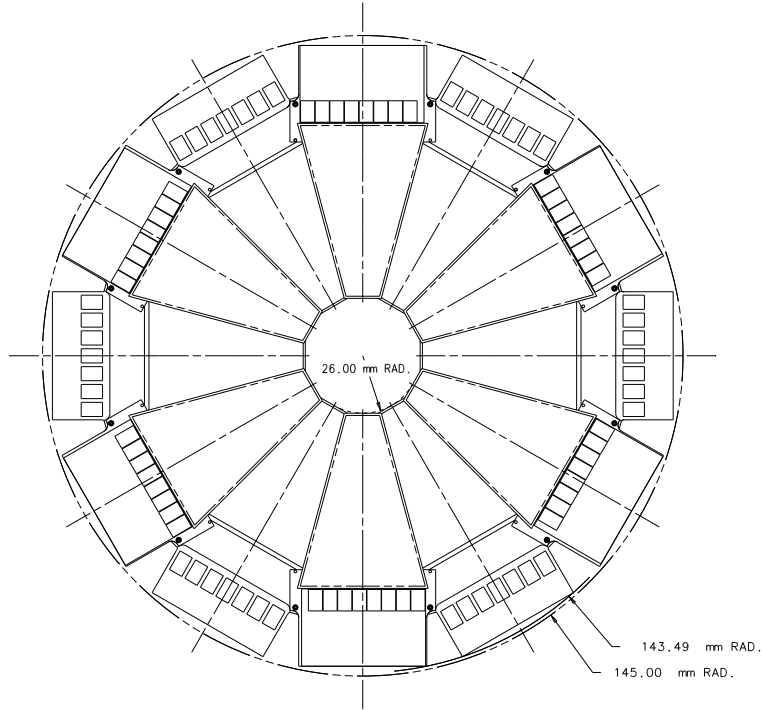
Figure 3.5: F-disk layout in the $r\phi$ plane.

Every F-disk contains 12 wedges as shown in Figure 3.5, which is drawn in the $r\phi$ plane. The wedges are assembled to overlap at the edges. This gives full coverage in ϕ as no dead regions are left. The inner radius of the F-wedges is 2.6 cm.

There are 12 F-disks that are numbered from 1 to 12 going from the North end to the South end of the detector, as shown in Figure 3.2. The first four disks (1 to 4) and

the last four disks (9 to 12) are positioned beyond the end of the barrel region in z. Disks 5 to 8 are located in between the six barrels.

The F-disks are arranged to minimize the gaps between barrels while keeping a small F-disk separation at higher $|z|$. This serves to maintain high tracking efficiency at low $|\eta|$ while maximising the vertex resolution by reducing extrapolation errors at high $|\eta|$. The barrel separation is kept to a minimum by engineering the F-disks to be as thin as possible. This is achieved by mounting the readout electronics at the outer radius of the F-wedges. The gaps between the barrels are further reduced by mounting the readout electronics for ladders on top of the active detector surface. This occupies space between layers rather than barrels.

Each H-wedge is 14.6 cm long with a width that varies from 2.8 cm to 6.5 cm. The detector is assembled by placing two single-sided wedge detectors back-to-back. Each one of these detectors has p-side strips with a pitch of 40 μm. They both have a stereo angle of 7.5° to give an effective stereo of 15° between them. As with F-wedges, the strip length varies across the detector.

H-disks have a similar layout to the F-disks, providing complete angular coverage in ϕ. Each H-disk contains 24 wedges that are arranged to have an inner radius of 9.5 cm. The H-disks are positioned at high $|z|$ and at a higher η than the CFT to provide measurements at large displacement from the nominal interaction point for tracks in the forward direction. This improves the momentum resolution for such tracks by increasing the measurement distance in the $r\phi$ plane and provides better discrimination between tracks as they have a greater distance over which to diverge.

As shown in Figure 3.2, the H-disks are numbered from 1 to 4 going from the North to the South end of the detector.

As with ladders, the wedges require a naming convention. References to specific wedges will be of the form

$$\text{F}\mathit{disk} - \mathit{view} - \mathit{wedge}$$

for F-wedges and

$$\text{H}\mathit{disk} - \mathit{view} - \mathit{wedge}$$

39

for H-wedges where *disk* is the disk number, *wedge* is the wedge number on the specified disk and *view* specifies p-side or n-side. *view* = 1 refers to the p-side and *view* = 2 refers to the n-side.

3.2 Readout

Once charge has been collected on the silicon strips, it must then be read out. What follows is a brief description of the readout systems used at DØ to handle this information. More information is available about the readout systems in the form of online documentation [24].

The first step in the readout chain for the SMT is the SVXIIe chip [25]. The SVXIIe chip is a purpose-built readout chip that is used in the CFT as well as the SMT. There are 128 readout channels that each have a preamplifier, 32-stage analogue storage pipeline, analogue to digital converter (ADC) and data sparsifier. The four modes of operation of the chip are Initialisation, Acquisition, Digitization and Readout.

In Initialisation mode, the configuration of the SVX chip is set by downloading run parameters from a database. These include the hit threshold, whose use is explained later. During Acquisition, the charge deposited on each strip is preamplified and stored in the analogue pipeline. The pipeline is a series of capacitors that are used to store signals while waiting for a response from the Level 1 trigger system.

When an event is accepted at Level 1, the chip begins to operate in Digitization mode. During Digitization, the relevant capacitor in the pipeline is accessed and the charge is sent to the ADC. The resulting digitized signal is an integer number between 0 and 255 in units referred to as ADC counts. While each ADC count corresponds to a set amount of deposited charge, any input that corresponds to greater than 255 ADC counts is truncated to this maximum value. The signal is then compared against a hit threshold. The threshold is common to all 128 channels in the SVX chip and any signal that exceeds it is flagged as a hit.

During Readout mode, the channels are read out in one of three ways. For sparse readout, only hit strips are recorded. Sparse readout can be performed in 'Nearest Neighbour' mode which means that the two strips next to each hit strip are kept as well. It is also possible to read out all 128 channels in the SVX. This is called 'Read

All' mode. The style of readout is set when the chip is initialised. Sparse readout mode allows the SMT to operate with a much reduced readout time and event size so it is preferred during normal data-taking. In Read All mode, the SMT must read out approximately 793,000 channels.

During the Digitization and Readout stages, no new data are collected. This time is used to reset the components in the SVX chips. This is necessary as the preamplifier has a reset time of a few hundred nanoseconds and can only otherwise be reset in the gaps between superbunches.

Every channel in the SMT reads out a non-zero digitized signal per event even if no charge is collected from ionisation in the detector. This minimum signal is called the pedestal and represents a 'zero-point'. Pedestals are roughly Gaussian with a steady mean value and a standard deviation of order 2–3 ADC counts. This standard deviation is significantly lower than the amount of charge typically recorded during particle detection. Subtracting the pedestal from the total charge therefore yields approximately the correct amount of useful signal from ionisation.

Data sparsification takes place before pedestal subtraction. It is designed to reject channels with no useful physics information and achieves this by applying a lower threshold for recorded channels. The thresholds used in the SMT are based on up-to-date pedestal and standard deviation values. This calculation will be discussed in more detail in Section 3.3. The standard deviation is referred to as the pedestal error and is caused by effects such as thermal noise in the n-type silicon bulk and electronic fluctuations in the readout chain. Usually the pedestal and error values are similar for all channels in an SVX chip. A single threshold per SVX chip is therefore usually sufficient.

The next components in the readout chain are the sequencer crates. These are responsible for controlling the SVX chips for data acquisition and relaying readout information from the SVX chips to the buffer crates for storage once a Level 1 trigger accept occurs. The sequencers produce signals to control the SVX chips after receiving commands from the Serial Command Link (SCL). These commands dictate which of the four modes described above the SVX chips should be in.

The SCL is a data path that connects the trigger framework to sections of the detector. It conveys Level 1 and 2 decisions from the trigger framework to the detector as well

as timing information. The SCL also informs the trigger framework of sections of the detector that are either busy or experiencing errors.

The buffer crates are used to hold the channel information until a Level 2 decision has been made. For a Level 2 accept, the information is passed to the Level 3 trigger system. For a Level 2 reject, the information is discarded. The buffer crates also house the Secondary Data Acquisition (SDAQ) system which is used for calibration purposes and is described in further detail in Section 3.3.

For online monitoring purposes, the Data Distributor [26] is also an important part of the readout chain. The Data Distributor is a piece of software that has access to the events being written to tape after Level 3 selection. It then distributes them to monitoring applications on request.

3.3   Secondary Data Acquisition

Secondary Data Acquisition (SDAQ) runs [27] are used to calculate pedestals and errors. They are dedicated runs taken between Tevatron stores when there are no collisions. The SVX chips are given an automatic Level 1 accept to force readout in Read All mode for every event. The information reads out to the buffer crates where it is analysed in the local front-end processor rather than being passed to the Level 3 trigger system. For each SVX channel, a pedestal and error are calculated. The pedestal is the mean signal per event during the SDAQ run. The pedestal error is the standard deviation of the signal during the SDAQ run. These values are committed to a calibration database.

The SDAQ Browser is an offline tool for calculating thresholds using the data from SDAQ runs. More information about the SDAQ Browser can be found at [28]. Calibration information for every channel in a ladder or wedge can be displayed using the SDAQ Browser. Threshold values can also be compared with pedestal distributions to allow experts to gauge their effectiveness. The SDAQ Browser does not directly access the calibration database for the pedestals and errors from a particular SDAQ run, but instead they are extracted and stored in the form of ROOT files by a separate program. The ROOT files are then loaded by the SDAQ Browser.

It is necessary to use an up-to-date set of thresholds for optimised particle detection.

The configuration of the SMT or the readout chain may change over time and this can affect the pedestal and noise levels. If the threshold is set too high then the channels will be less efficient at registering ionisation charge from genuine particle detection. If the threshold is set too low then a higher incidence of fake hits (the 'fake rate') will be caused by noise fluctuations. Increased fake rates lead to increased numbers of track combinations in the offline event reconstruction, adding to the processing time per event.

An example window produced by the SDAQ Browser is shown in Figure 3.6. The pedestals and errors for all channels in the ladder B3-6-12 are plotted against channel number in the top and bottom plots respectively. This ladder has six SVX readout chips, three on the p-side and three on the n-side. The pedestal distribution shows the chip structure by a small shift after every 128 channels. At around channel 384, the distribution drops from around sixty ADC counts to around forty ADC counts reflecting the change from p-side to n-side. The first channel in each p-side chip has a pedestal much lower than the surrounding values. This is a feature commonly seen in the SMT output but has not yet been explained. Due to the common threshold per SVX chip, these channels will be less efficient but may still contribute to physics output. As mentioned earlier, it can be seen that in general, the pedestal and error distributions have a high degree of uniformity for channels in the same SVX chip.

The pedestal plots in Figure 3.6 also show two sets of proposed thresholds. The green line represents the current default algorithm for calculating thresholds. This algorithm proceeds as follows:

- A reliable selection of channels is chosen by eliminating those that are noisy or malfunctioning. A noisy channel has a pedestal error greater than six ADC counts and a malfunctioning channel has pedestal of zero ADC counts or above two hundred ADC counts.

- The pedestals and errors for the remaining channels are put into sorted lists in ascending numerical order. The middle 60% of each list is kept.

- The means of the pedestals and pedestal errors in this final selection, μ_{ped} and μ_{error} respectively, are calculated.
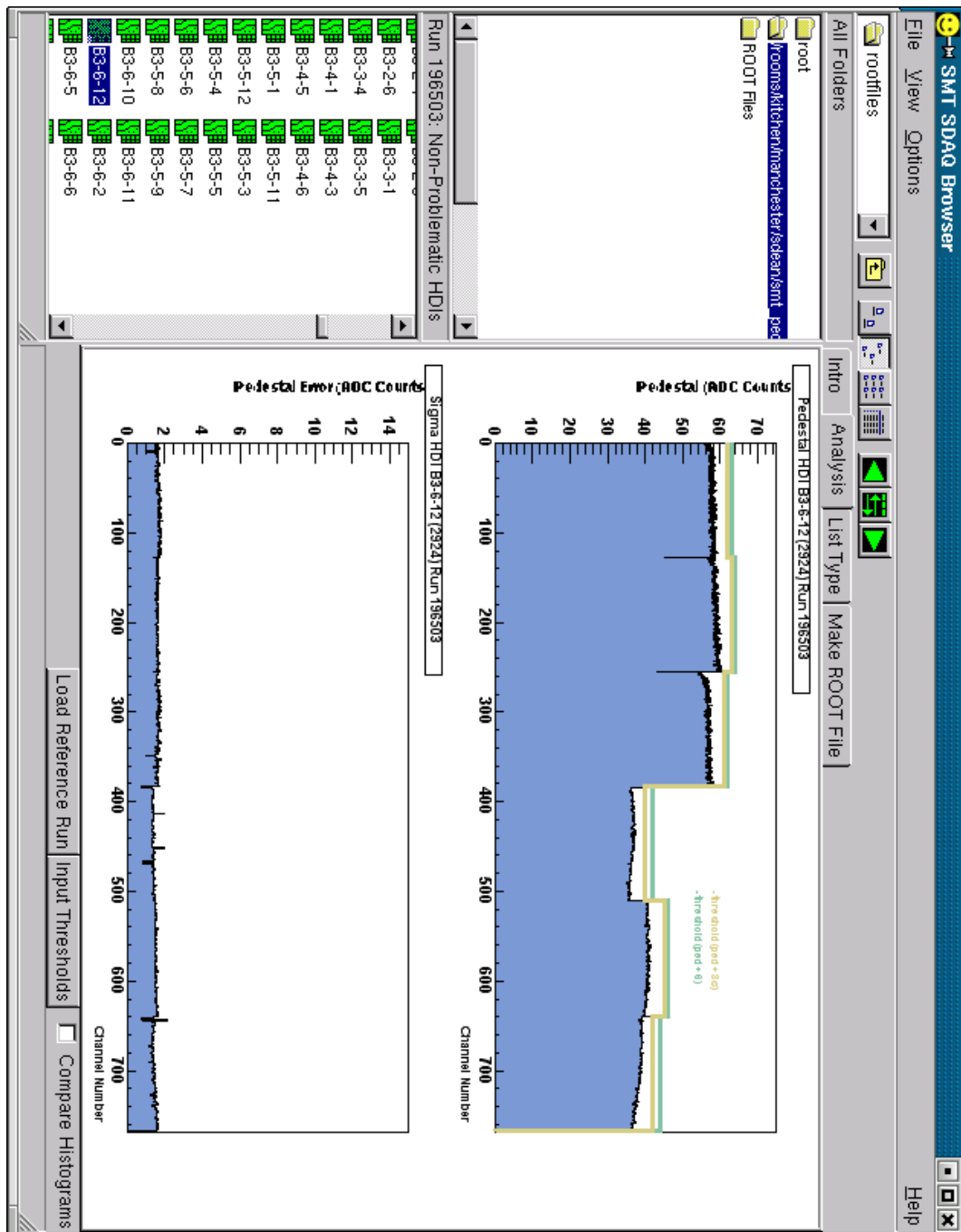
Figure 3.6: The SDAQ Browser main window. Pedestals and errors are plotted against channel number for ladder B3-6-12.

- μ_{ped} and μ_{error} are set to zero if there less than five good channels or more than 100 channels that are noisy or dead.

- The threshold is found by adding six ADC counts to μ_{ped}.

- If the calculated threshold is not in the range 10–230 ADC counts, or if μ_{error} is greater than four ADC counts then the threshold is set to 255 ADC counts. This is equal to the maximum output for an SVX channel so readout is therefore suppressed in sparse mode.

The SDAQ Browser flags problematic detectors. A 'noisy' detector has at least 4% noisy strips and a 'below threshold' detector has a calculated threshold more than 25 ADC counts below the current database threshold. The algorithm for calculating thresholds described above is used as the default but the SDAQ browser allows experts to plot alternative values against the pedestal distribution. These can either be produced by an alternative algorithm or put in by hand. The brown line in Figure 3.6 shows thresholds produced by adding $3\mu_{error}$ to μ_{ped}. The current thresholds can also be extracted from the calibration database and plotted.

The SDAQ browser can commit new thresholds to the calibration database. These come into effect the next time the SVX chips are initialised.

It is also possible to access the threshold history of detectors with the SDAQ browser. An example is shown for wedge F6-1-10 in Figure 3.7. The threshold for the eight p-side SVX chips are shown as a function of time and chip number. The figure indicates that the second SVX chip had a threshold of 255 ADC counts from mid-2002 until the start of 2003, suggesting it was defective during this period.

3.4 The SMT Event Display

The SMT event display is part of the online monitoring at DØ and is described in more detail in [29]. The purpose of online monitoring is to highlight detector problems when they occur to avoid losing good quality physics events. It is important to fix detector problems quickly in order to minimise such losses. If data is recorded during a period when some detector components are malfunctioning, it is usually excluded from physics analyses.
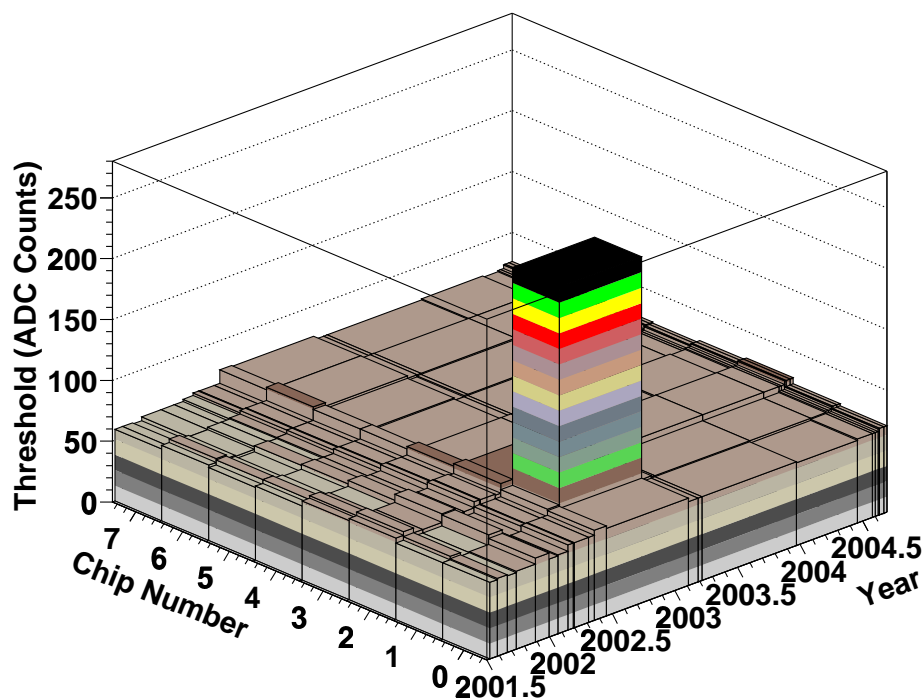
Figure 3.7: Threshold history for the SVX chips in wedge F6-1-10. The chip number is expressed in array indices.

The event display is a piece of software for monitoring the strip-level output of the SMT on an event-by-event basis. It works in parallel with the tools for monitoring the basic operation of the silicon detectors. These provide information such as bias voltages and power supply statuses. The event display also supplements SMT Examine, a tool for monitoring basic histogrammed physics quantities such as cluster charge.

The event display takes input events from the Data Distributor. Signals are unpacked, calibrated and displayed on a graphical representation of the SMT. It is important that this display is clearly presented so that problems can be easily seen and fixed. The layout of the graphical display is shown in Figure 3.8.

There are eight display windows. Six of these each show the readout of one barrel and an adjacent F-disk. One window shows the readout for the remaining F-disks and the H-disks. The eighth window gives a key to the barrel display with layer and ladder numbers and control menus for operating the event display.

Each barrel display is drawn in the $r\phi$ plane, as shown in Figure 3.9. The number of the displayed barrel and F-disk are shown at the top-left of the display window. Ladders are drawn in black or orange to indicate which buffer crate it reads out to.

Figure 3.8: Layout of the SMT event display during normal operation.
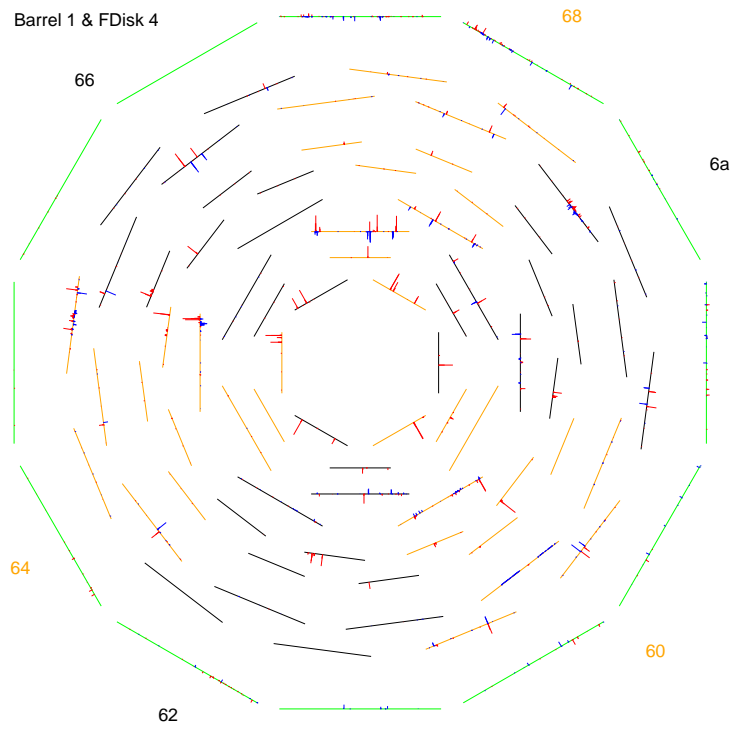
Figure 3.9: A barrel window in the SMT event display. Signals are pedestal subtracted.

The buffer crate number is indicated at the outer edge of the display. The F-disk is drawn outside the barrel. Each F-wedge is represented by a green line.

Strip signals are drawn in red for p-side strips and blue for n-side strips on opposite sides of each detector. The length of each line is proportional to the signal amplitude. Lines representing p-side ladder signals are drawn in the positions that correspond to the physical position of the axial strips in the real SMT. The lines representing the n-side ladder signals and the F-wedge signals cannot be interpreted in the same way because in the real SMT, they are set at a stereo angle to the beam direction. Instead, the lines show the signal position in the readout for the ladder or wedge.

The disk display window shows the readout from the forward F-disks and the H-disks, as shown in Figure 3.10. F-wedges are drawn in green while the H-wedges are drawn in black. The wedges from each disk are drawn colinearly and the number for each F-disk appears above the output. Again, this does not reflect the real SMT geometry but this layout is designed to be compact and clear.

The SMT event display is displayed at all times during data-taking. The display is

48
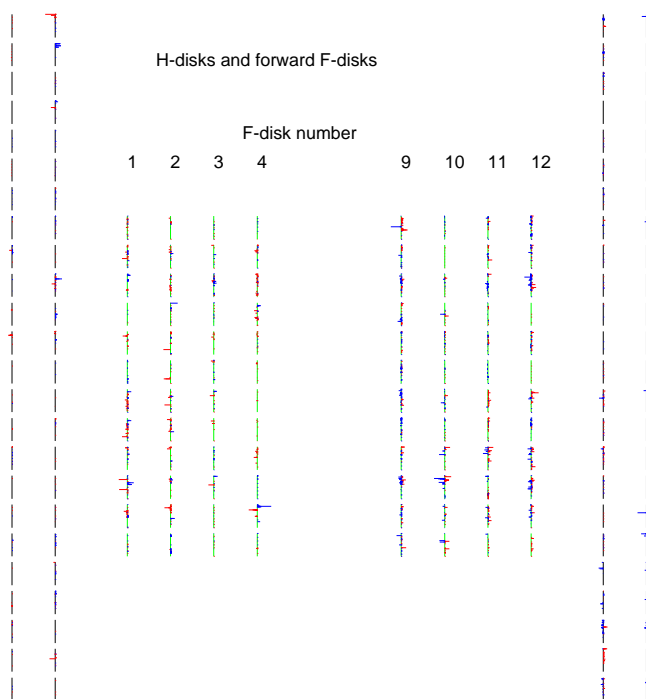
Figure 3.10: Disks window in the SMT event display. Signals are pedestal subtracted.

updated regularly with a default time interval of 5 seconds. This can be changed manually. It is also possible to change the signal calibration. The signals shown in Figure 3.9 are pedestal-subtracted. This gives a feeling for how the data looks during offline reconstruction and it is possible to see hit patterns that may correspond to tracks. During normal operation, it is preferable to display the full readout from each channel as shown in Figure 3.11. This makes detector problems much easier to see. For example, it is obvious from looking at Figure 3.11 that there is no readout from buffer crate 69 in this run.

When detector problems are observed, attempts are made to restore stable data-taking operation. If the problem cannot be fixed then the affected detectors are disabled and do not contribute to the SMT readout.

3.5 Common Noise Problems

As described in Section 3.3, pedestal errors are typically 2–3 ADC counts and come from noise effects in the silicon or the readout chain. At this low level, noise is easily

49
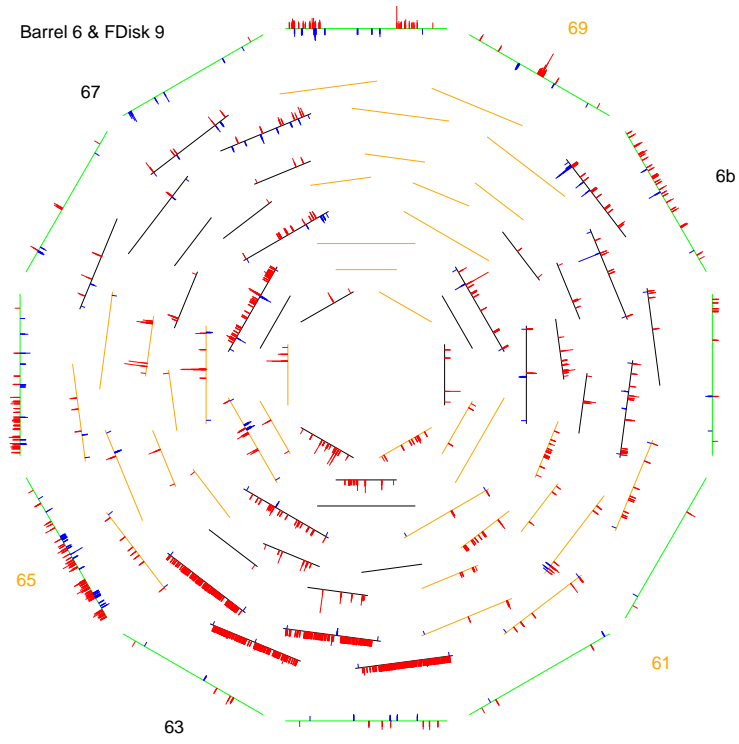
Figure 3.11: A barrel window in the SMT event display. Signals are not pedestal subtracted. Examples of dead electronics (top-right) and coherent noise (bottom-left) can be seen.

dealt with by applying a sensible threshold during sparse readout. Some instances of noise are more difficult to deal with. A few examples are presented here.

The SMT event display in Figure 3.11 shows channel output for barrel 6 and F-disk 9 with no pedestal subtraction. Some of the ladders towards the bottom of the display exhibit coherent noise. This is characterised by a group of adjacent strips experiencing a similar jump in pedestal for individual events. Coherent noise can affect all of the channels in an SVX chip at the same time. While coherent noise increases the pedestal error, the biggest problem is that it causes a sudden increase in the fake rate if the pedestal jump is big enough to exceed the SVX chip threshold.

One of the biggest problems for the DØ SMT is 'grassy noise'. An example of grassy noise is shown in the SDAQ Browser output in Figure 3.12. p-side information for the eight SVX chips in wedge F7-1-6 is displayed. Grassy noise is characterised with many narrow spikes in the pedestal error distribution. There are many noisy strips with a non-uniform distribution. The first and fifth SVX chips are most affected by
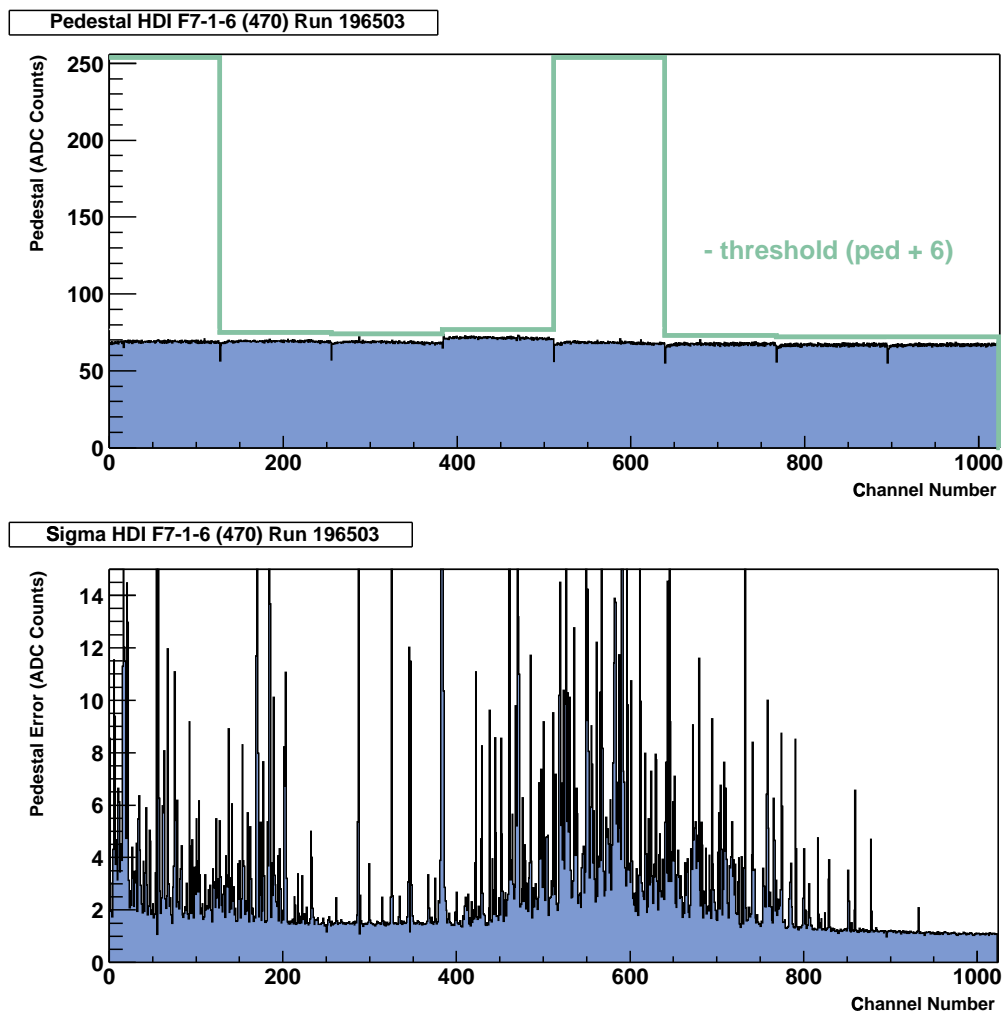
Figure 3.12: Pedestals and errors for wedge F7-1-6. An example of grassy noise can be seen in the pedestal error distribution.

the grassy noise and have μ_{error} greater than 4 ADC counts. The calculated threshold values are 255 ADC counts as a result.

The non-uniform pedestal error distribution means that not all SVX chips experiencing grassy noise will be classified as noisy in this way. The SVX chips in Figure 3.12 with a non-maximum threshold continue to output signals as normal and will experience a high fake rate as a result.

Grassy noise may be caused by the 'micro-discharge effect' [30]. This occurs when the voltage applied to a silicon strip is large enough to cause a strong electric field at the edge of the strip. This can cause an avalanche-like multiplication of charge-pair generation and therefore a jump in the noise level. Grassy noise is predominantly observed in the F-disks.
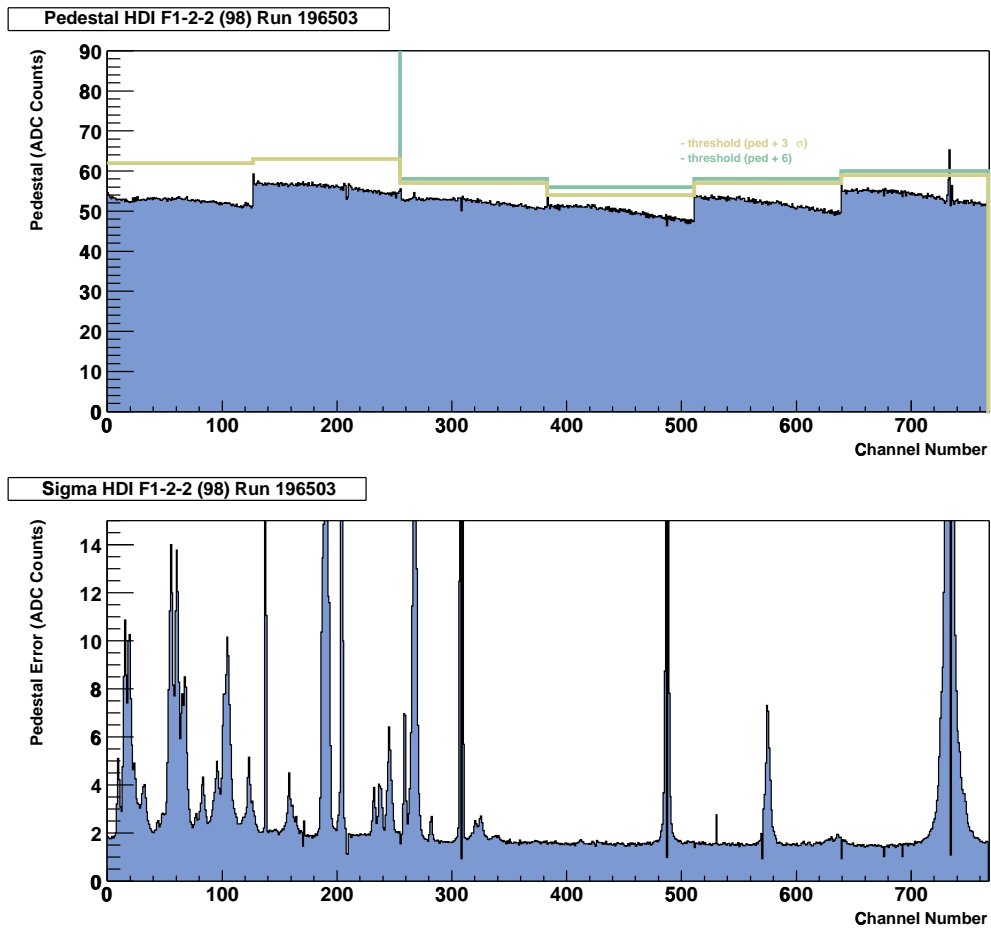
Figure 3.13: Pedestals and errors for wedge F1-2-2. Examples of the pinhole effect can be seen in the pedestal error distribution.

Examples of the 'pinhole effect' are shown in Figure 3.13. This is output from the SDAQ Browser for the six n-side SVX chips in wedge F1-2-2. The most pronounced example is shown at around channel 740 and features a wide spike in pedestal error with an accompanying shift in the pedestal distribution. The spikes at lower channel number may also be smaller versions of the same effect although it is unusual to see so many instances in the same detector. The pinhole effect stems from the fact that the silicon strips are AC-coupled to the readout with a capacitor. If a coupling capacitor shorts then DC current flows directly into the SVX chip and causes the behaviour shown.

3.6 Performance Study for SMT Hardware

The purpose of the DØ central tracker is to reconstruct the path of charged particles through the central volume. The offline track reconstruction involves fitting the parameters for a helix to a collection of 3-dimensional points within the central tracker. These points are referred to as 'global hits' and must be calculated using the output from the SMT and the CFT.

For the SMT, the first step of this process is clustering. Strips are unpacked from the event and assigned a status based on up-to-date calibration information from SDAQ runs (see Section 3.3). All strips are 'good' by default to begin with. If a strip has a pedestal less than 10 ADC counts then it is 'dead' and is discarded. If a strip has a pedestal error greater than 6 ADC counts then it is 'noisy'. The pedestals are subtracted for the good strips while the signal is set to 0 ADC counts for noisy strips.

Good strips with a signal of at least 4 ADC counts are then used for clustering. A cluster is a contiguous group of strips with a total charge of at least 8 ADC counts. Noisy strips do not contribute to the total charge but can still form part of a cluster. Dead strips do not feature in clustering so they can split clusters.

The charge distribution in a cluster indicates the position in one dimension of a charged particle crossing the detector. This position is called a '1d hit' and is calculated by finding the mean of the strip positions weighted by their pedestal-subtracted signal.

The stereo angle between p-side strips and n-side strips in a double-sided silicon detector means that 1d hits from each side of the detector are combined to provide a two dimensional position. This is called a '2d hit'. The 2d hit is then combined with the position and orientation of the detector to provide a global hit.

If a charged particle crosses a double-sided silicon detector that is operating as intended then in most cases, a global hit will be produced. The lower limits on signal amplitude and cluster charge imply small losses in efficiency due to effects like the angle of particle incidence and the distribution for the amount of ionised charge deposited. Hardware effects such as dead or noisy channels or groups of channels are expected to affect the efficiency to a much greater extent.

A good measure of the hardware performance can therefore be gained from the effi-

Surface Type	Strip Pitch (μm)	Resolution (μm)
Axial p-side Barrel	50.0	17.5
2° Stereo n-side Barrel	62.5	22.2
90° Stereo n-side Barrel	153.5	85.4
+15° Stereo p-side F-disk	50.0	25.7
−15° Stereo n-side F-disk	62.5	25.9

Table 3.1: Calculated resolutions for matching a 1d hit to a track.

ciency of finding a hit to match the known crossing point of a charged particle. This can be achieved by looking in fully reconstructed offline data at 1d hits on a detector surface in relation to the crossing point of a track.

To access 1d hits in offline data requires a lot of computing resources as they are not normally included in the available fully reconstructed data. The full reconstruction must therefore be repeated, keeping the 1d hit information. A sample of 21993 minimum bias events have been processed in this way. The data were taken during a period in which the SMT was operating normally.

It is first necessary to find the resolution for matching a 1d hit to a track (σ_{hit}). This value will vary between surfaces with different strip pitches so five different resolutions are calculated for the surface types shown in Table 3.1. When this study was performed, H-disks were not used in the tracking so they were not included.

The resolutions are found by plotting the displacement between 1d hits and the crossing positions of high p_{T} 'no-hit' tracks. A no-hit track has been refitted to exclude any global hit on the detector containing the 1d hit. This avoids biasing the resolution to low values as, by definition, a track will cross a detector very close to a hit that has contributed to the track fit. The high p_{T} requirement excludes tracks with $p_{\text{T}} < 5$ GeV/c. For each surface the track encounters, the displacement is calculated for every 1d hit found.

The displacement plots are shown in Figure 3.14. The resolution values are calculated by fitting a Gaussian distribution added to a uniform background and extracting the Gaussian width. The uniform distribution corresponds to 1d hits that are uncorrelated with the considered track. While the distributions clearly have non-Gaussian features,

the fit is a good approximation for the purpose of this study. The resolutions found are shown in Table 3.1.
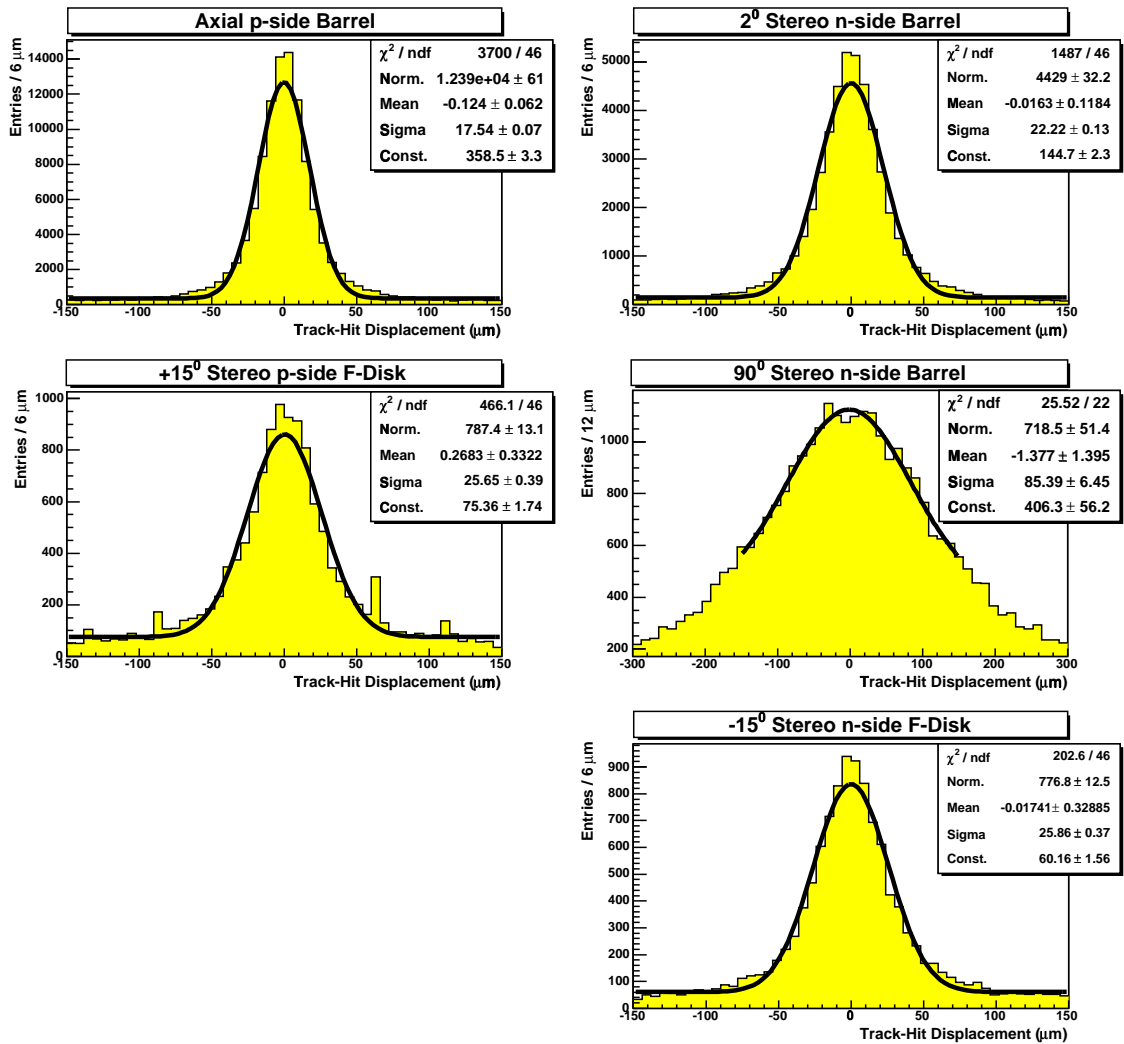
Figure 3.14: Plots of the displacement between 1d hits and no-hit tracks for five different types of detector surface. The Gaussian fit on a uniform background provides a resolution for matching 1d hits to tracks.

In a true Gaussian distribution, 99.9999% of all measurements should fall within $5\sigma_{\text{hit}}$ of the mean value. The displacement of 1d hits from their associated track has been shown to look approximately Gaussian so it is expected that a very high fraction of 1d hits should fall within $5\sigma_{\text{hit}}$ of the no-hit track crossing position unless there are inefficiencies caused by defective hardware.

This assertion is tested by calculating the efficiency per detector of finding a 1d hit within $5\sigma_{\text{hit}}$ of the no-hit track crossing position, denoted ϵ. For the calculation

of ϵ, instances of tracks crossing detectors are limited to those in which the track is sufficiently far from the edge of the active detector surface. This is ensured by demanding that the contour representing 5 times the tracking errors in the plane of the detector surface is completely inside the active detector area. Defining this fiducial region avoids any associated drop in efficiency due to edge effects. Only no-hit tracks with $p_{\mathrm{T}} > 5$ GeV are used, of which there are 41,600 in the data sample. The track must also have at least 2 global SMT hits on other detectors.

If a 'match' is defined as a track crossing with a 1d hit within $5\sigma_{\mathrm{hit}}$ then ϵ for a particular detector is defined by

$$\epsilon = \frac{\mathrm{n(matches)}}{\mathrm{n(crosses)}}$$

where n(matches) is the number of matches and n(crosses) is the number of crosses. ϵ has a binomial error. It is interesting to find the mean ϵ for each layer in the barrels ($\bar{\epsilon}_{layer}$) and the mean ϵ for each disk in the F-disks ($\bar{\epsilon}_{disk}$). The mean values are calculated by excluding any detectors with $\epsilon = 0$ and averaging over the remaining detectors. $\bar{\epsilon}_{layer}$ for all six barrels is plotted in Figure 3.15 (p-side) and Figure 3.17 (n-side) while $\bar{\epsilon}_{disk}$ for all twelve F-disks is plotted in Figure 3.16 (p-side) and Figure 3.18 (n-side).

For both p-side and n-side 1d hits, the barrel plots indicate that $\bar{\epsilon}_{layer}$ increases with layer number, corresponding to an increase in the radius. This is especially noticable for the innermost barrels in z (3 and 4) whose detectors are closest to the nominal interaction point. The trend is not as prominent in the outer barrels in z. In general, the barrel plots contain fluctuations in $\bar{\epsilon}_{layer}$ that are not statistical. The two outer barrels have single-sided detectors in superlayers 1 and 3 so they do not contribute to the n-side plots.

It is difficult to see any trend in the F-disk plots as $\bar{\epsilon}_{disk}$ experiences non-statistical fluctuations. It is worth reiterating that the errors plotted are purely statistical and therefore do not reflect contributions from hardware inefficiencies. $\bar{\epsilon}_{disk}$ has larger statistical uncertainties in the outer F-disks, which is expected as they take measurements at higher $|\eta|$ and the sample consists of high p_{T} tracks.

As there are a number of contributing factors to the efficiencies in data, it is useful to get more information from a study of ϵ in Monte Carlo. The full offline event
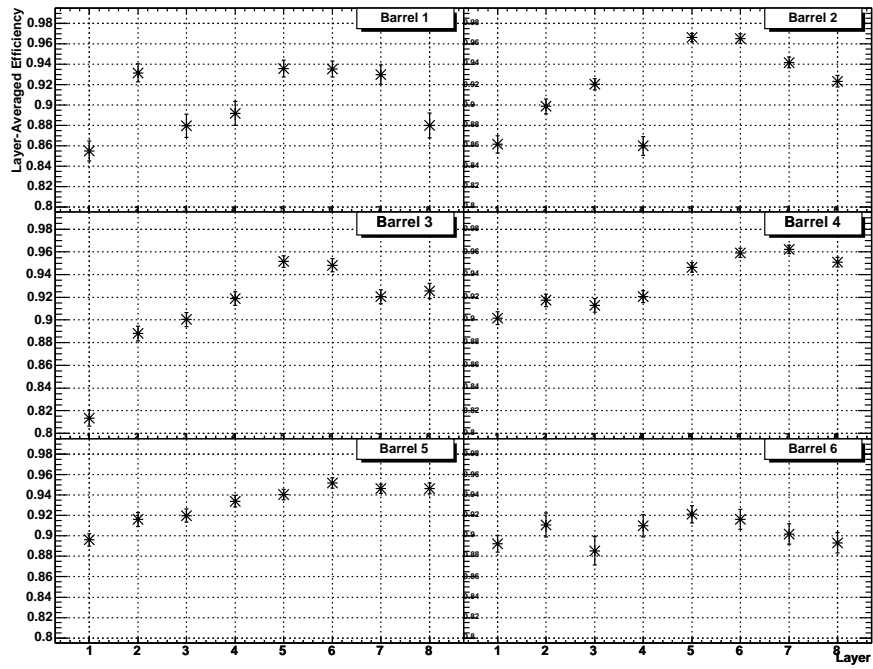
Figure 3.15: Layer-averaged p-side barrel efficiencies in data.
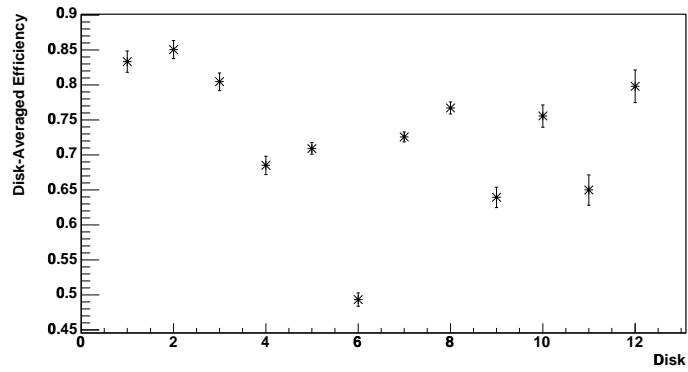
Figure 3.16: Disk-averaged p-side F-disk efficiencies in data.

57
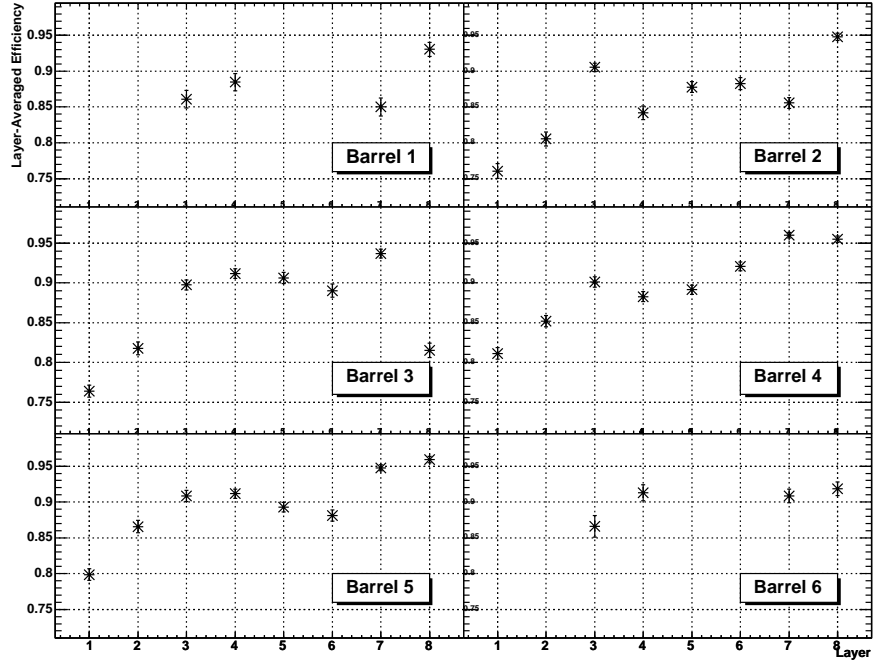
Figure 3.17: Layer-averaged n-side barrel efficiencies in data.
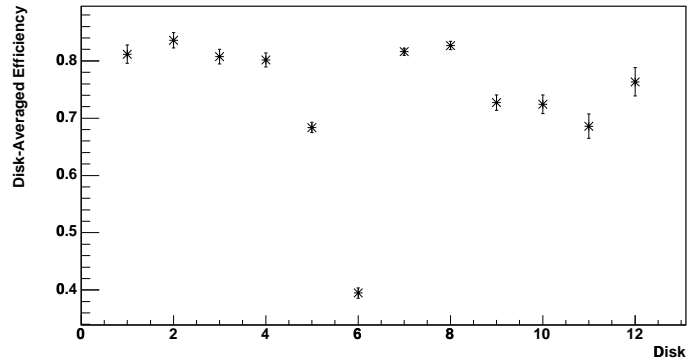
Figure 3.18: Disk-averaged n-side F-disk efficiencies in data.

reconstruction involves simulating the digitized output of the SMT so the efficiencies in Monte Carlo can be obtained by performing the same algorithm previously described for data. The digitization is simulated by modelling the deposited energy for charged particles crossing silicon detectors and then modelling how the resultant 'charge cloud' drifts onto the strips. The charge per strip is then digitized by applying a conversion factor and adjusting to simulate noise with a Gaussian σ of 2 ADC counts [31]. The deposited energy is simulated with Geant.

Process	Number of Events
$W \to \tau \nu$	1,250
$\gamma +$ jets inclusive	4,250
QCD inclusive	8,500
$t\bar{t}$ inclusive	2,000
$Z^0 \to b\bar{b}$	3,750
$Z^0 \to e^+ e^-$	4,750
$Z^0 \to \mu^+ \mu^-$	5,000
Single γ, $p_{\mathrm{T}} = 100$ GeV/c	1,000
All	30,500

Table 3.2: Composition of digitized Monte Carlo sample used to study efficiencies

There were a very small number of digitized Monte Carlo samples available when this study was performed. They were all used to produce a sample of 16,509 events containing 47,270 tracks with $p_{\mathrm{T}} > 5$ GeV/c. The composition of the sample before the p_{T} cut is shown in Table 3.2. There are a greater number of high-p_{T} tracks per event in the Monte Carlo sample than for the data. It is reasonable to attribute this to the different physics processes involved.

The plots obtained in Monte Carlo for $\bar{\epsilon}_{layer}$ are shown in Figure 3.19 (p-side) and Figure 3.21 (n-side) while the plots obtained for $\bar{\epsilon}_{disk}$ are shown in Figure 3.20 (p-side) and Figure 3.22 (n-side). The efficiencies are generally higher than those observed in data and the radial dependence is still present in the barrel plots. The F-disk efficiencies show some z-dependence, with the outer F-disks in $|z|$ having higher values. The efficiencies in both barrels and F-disks therefore show dependence on the distance
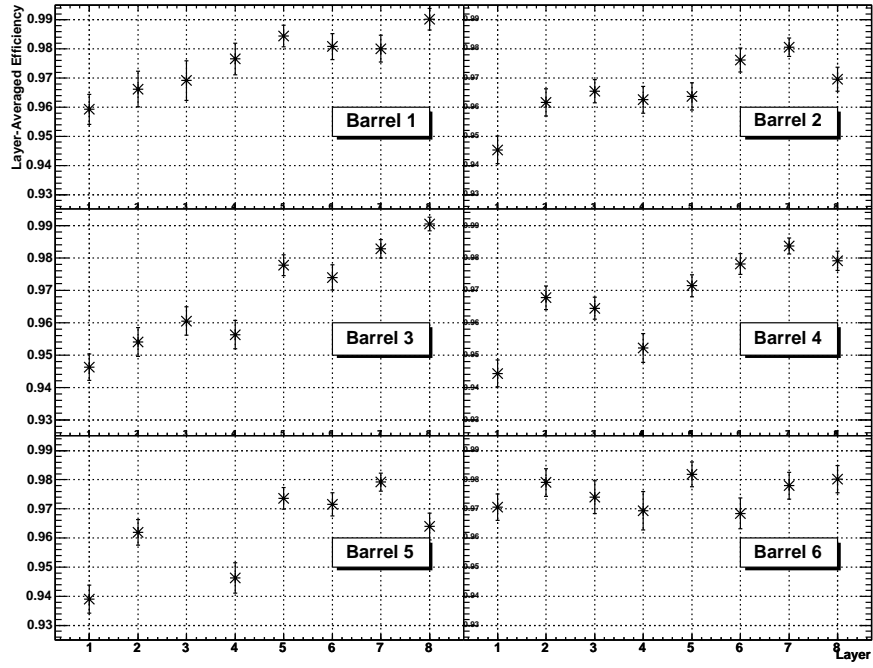
Figure 3.19: Layer-averaged p-side barrel efficiencies in Monte Carlo.
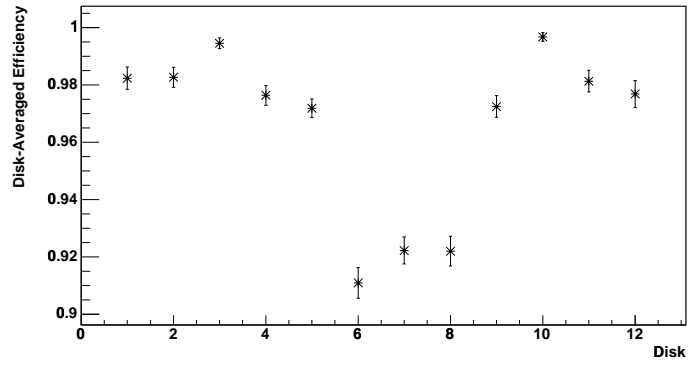
Figure 3.20: Disk-averaged p-side F-disk efficiencies in Monte Carlo.
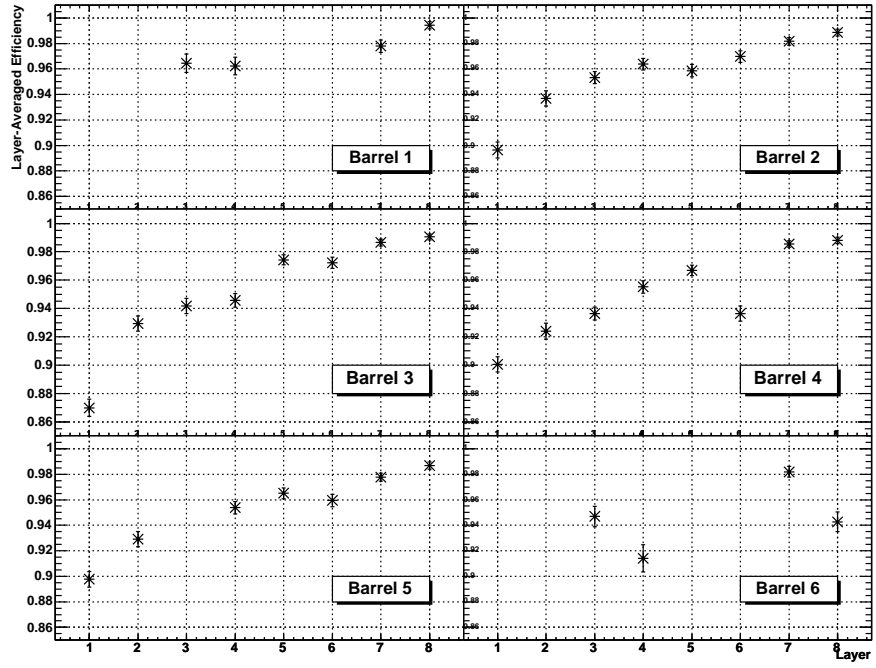
Figure 3.21: Layer-averaged n-side barrel efficiencies in Monte Carlo.
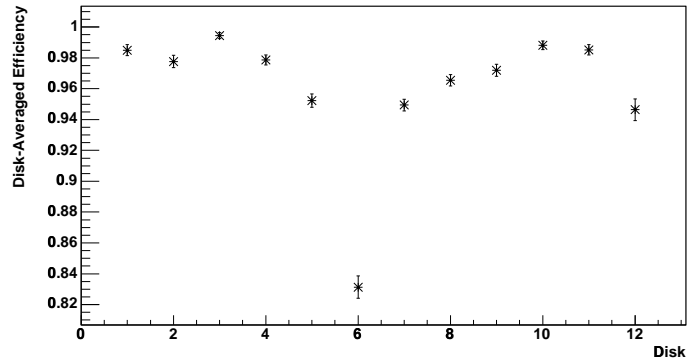
Figure 3.22: Disk-averaged n-side F-disk efficiencies in Monte Carlo.

of the detectors from the nominal interaction point. That said, both barrel and F-disk plots still show non-statistical fluctuations.[1]

The Monte Carlo samples used for this study do not model hardware effects such as dead strips or readout channels. The tracking routines are the same in both samples so comparing Monte Carlo and data distinguishes between effects due to tracking and effects due to hardware problems. The dependency of ϵ on the distance from the nominal interaction point is seen for the barrel plots in both samples so it is reasonable to assume that this comes from the tracking. The z-dependency is seen in the F-disks in Monte Carlo but not in data. This suggests hardware problems in the F-disks.

The increase in efficiency levels between data and Monte Carlo could indicate a contribution from hardware but may also indicate that Monte Carlo is not correctly tuned to data. There have been improvements in tracker alignment [32] and the modelling of signal digitization [31] since this study was performed.
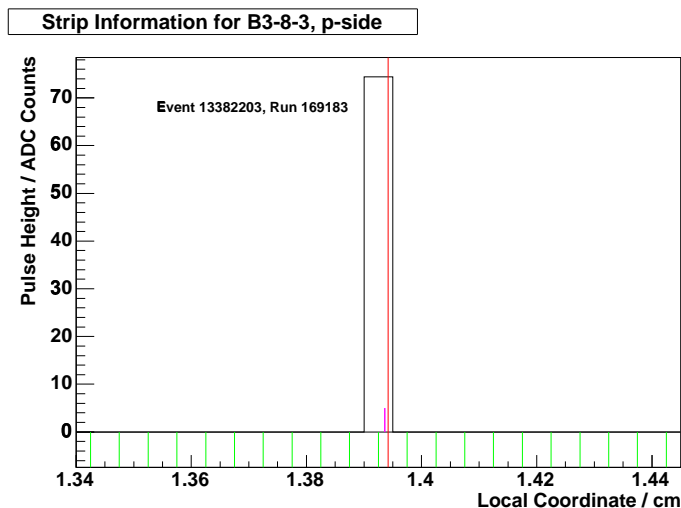
Figure 3.23: Example of a cluster with one strip, efficient crossing.

To get a better understanding of the contributions to ϵ, it is interesting to look at individual instances of tracks intersecting detectors. With access to the strip-level SMT output, it is possible to produce displays such as Figure 3.23. Each bin in the histogram contains the pedestal-subtracted signal for a strip. The signals are plotted as a function of the strip local coordinate, which refers to the position on the detector surface relative to a known fiducial mark. No-hit track crossing positions are

---

[1]The missing points for Barrel 5, Layer 3 are underflows. The values measured for this point are 0.827±0.008 on the p-side and 0.669±0.010 on the n-side.

represented by a red vertical line. The 1d hit position for the cluster is represented by a small pink line above the x-axis. In Figure 3.23, the charge from the track is all deposited in the crossed strip and the resulting 1d hit is within $5\sigma_{hit}$ of the crossing point so this is an efficient measurement. The x-axis has been scaled to highlight the interesting features so there are a small number of strips shown. The strip statuses as used in clustering are indicated by small lines below the x-axis. A green line indicates a good strip, a red line indicates a dead strip and a blue line indicates a noisy strip.
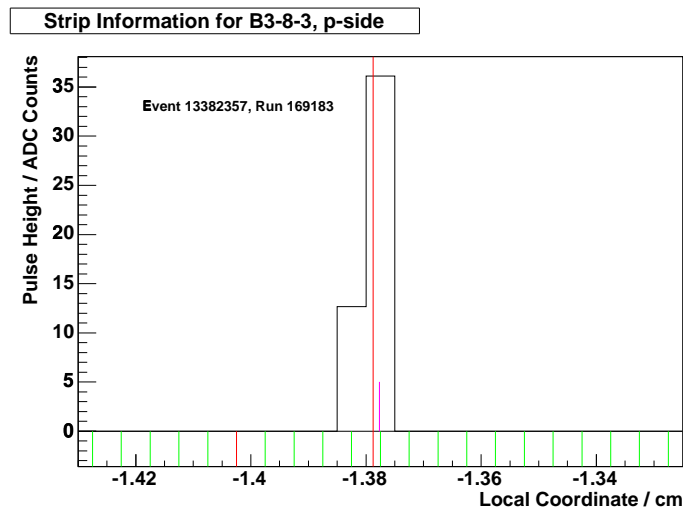
Figure 3.24: Example of a cluster with two strips, efficient crossing.
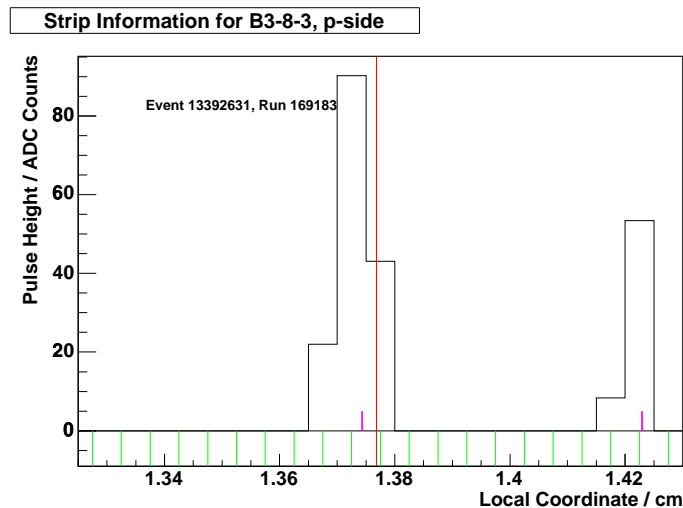
Figure 3.25: Example of a cluster with three strips, efficient crossing.

Examples of efficient crossings in which the charge distribution produces a cluster with two and three strips are shown in Figure 3.24 and Figure 3.25 respectively.

Strip Information for F9-4, p-side

Event 13441008, Run 169183
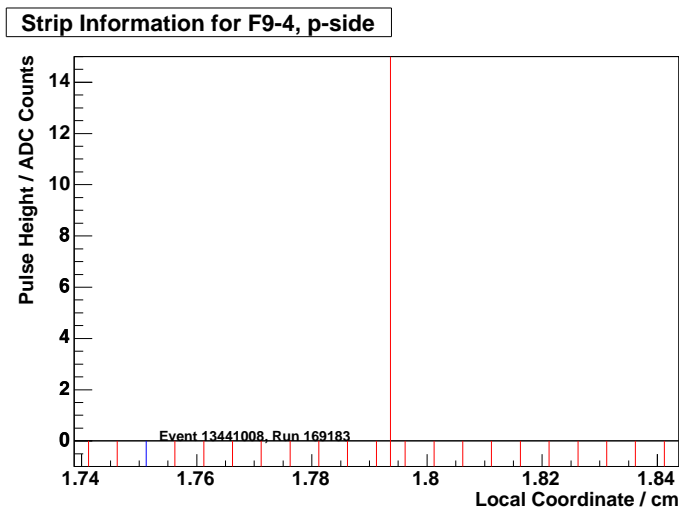
Figure 3.26: Example of a track intersecting dead strips, no cluster.

Inefficient crossings are dominated by those in which the track appears to create no cluster and those in which the track creates a 'wide' cluster. The charge distribution in a wide cluster means that the calculated 1d hit is more than $5\sigma_{hit}$ away from the track crossing point. An example of a track leaving no cluster is shown in Figure 3.26. The entire detector is dead so no useful measurement is made. Detectors containing noisy strips can produce a similar effect. This type of crossing does not feature in the Monte Carlo study.

Strip Information for B4-1-1, p-side

Event 13391440, Run 169183
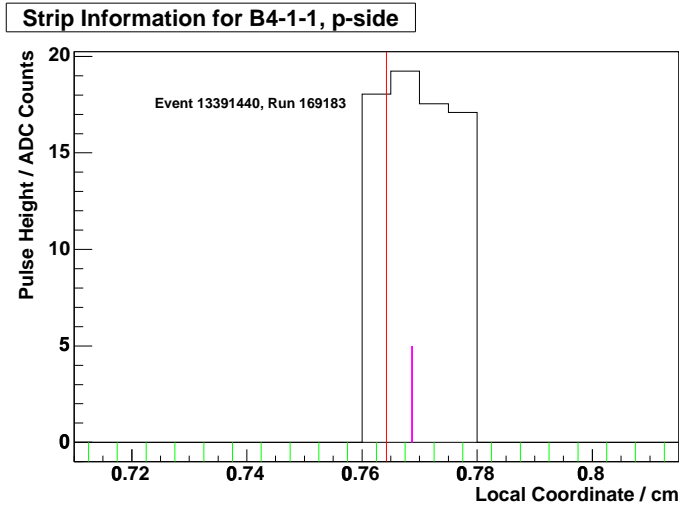
Figure 3.27: Example of a wide cluster with a single maximum, inefficient crossing.

Wide clusters can again be subdivided into two main types. An example of the first type is shown in Figure 3.27. The cluster has a single maximum close to the track
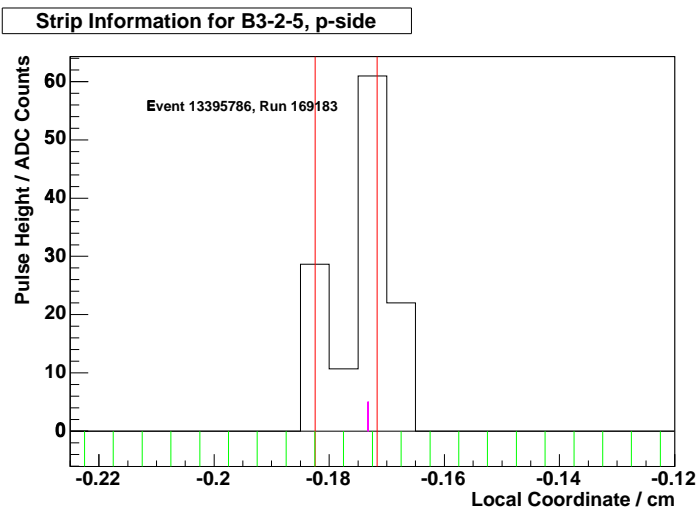
Figure 3.28: Example of a wide cluster with two maxima, inefficient crossing.

crossing position but the charge is spread over four strips so the 1d hit is displaced. It is therefore not matched to the track for the efficiency study. An example of the second type is shown in Figure 3.28. There are two peaks in the charge distribution, both of which appear to be caused by incident charged particles. This implies that the charge distributions from two tracks have been merged into one cluster. The presence of the peak on the right drags the 1d hit away from the peak on the left causing an inefficiency in the 1d hit-finding.

Clusters with multiple charge peaks are also involved in efficient crossings. This is also shown in Figure 3.28. The 1d hit has been calculated close to the charge peak on the right and therefore it is found by the corresponding track. For a typical efficient cluster, the calculated uncertainty on the 1d hit is of order 10 μm. The calculated uncertainty on the 1d hit shown in Figure 3.28 is 40 μm, which is problematic during tracking. The 1d hit error will reduce the contribution of the global hit to the track fit. This represents a loss of information compared to the ideal situation in which each of the two merged charge distributions are considered separately as individual clusters. This is not currently considered in the clustering algorithm.

A small fraction of clusters with multiple charge peaks are obviously not caused by multiple tracks, such as that shown in Figure 3.29. The cluster shown is probably due to hardware problems. Nonetheless, the majority of clusters with multiple charge peaks have a similar form to that shown in Figure 3.28 and will be referred to henceforth as 'merged' clusters.
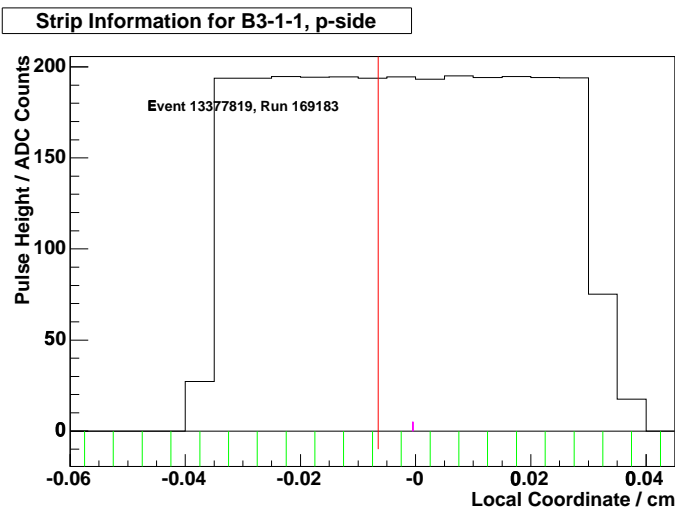
Figure 3.29: Example of a wide cluster with many maxima, efficient crossing.

In order to understand the extent of the problem caused by merged clusters, the fraction of all track crossings with a merged cluster (f_{merged}) are calculated per detector in data. The data sample from the calculation of ϵ is used and only no-hit tracks with $p_{\mathrm{T}} > 5\ \mathrm{GeV}/c$ and at least two other global SMT hits are considered. Edge effects are avoided by requiring that the track stays in the fiducial region described previously. In the barrels, the mean value of f_{merged} is found per layer and plotted in Figure 3.30 and Figure 3.32 for p-side and n-side clusters respectively. In the F-disks, the mean value of f_{merged} is found per disk and plotted in Figure 3.31 and Figure 3.33 for p-side and n-side clusters respectively.

The barrel plots for f_{merged} show a clear dependency on layer number. f_{merged} decreases as radius increases. This makes sense when considering that detectors closer to the interaction region cover a wider angular range. Clusters from tracks coming from the interaction point are therefore closer together and subsequently more likely to overlap. The n-side barrel plots are interesting as f_{merged} in superlayers 1 and 3, corresponding to 90° stereo strips, is generally higher than in superlayers 2 and 4. This also makes sense as the 90° stereo strip pitch is roughly three times bigger than the 2° stereo strip pitch which means that 90° stereo strips cover roughly three times as much angular space.

The p-side F-disk values for f_{merged} shown in Figure 3.31 may also indicate a dependency on the distance from the nominal interaction point. It is difficult to draw any conclusions from the n-side F-disk distribution for f_{merged} shown in Figure 3.33.

66
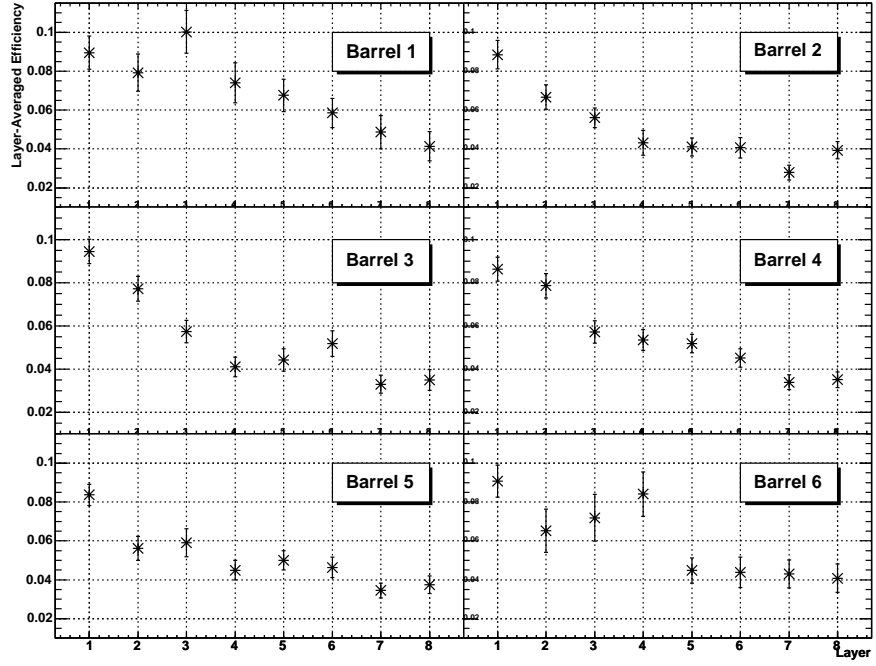
Figure 3.30: Fraction of crosses with merged clusters in data, p-side barrels.
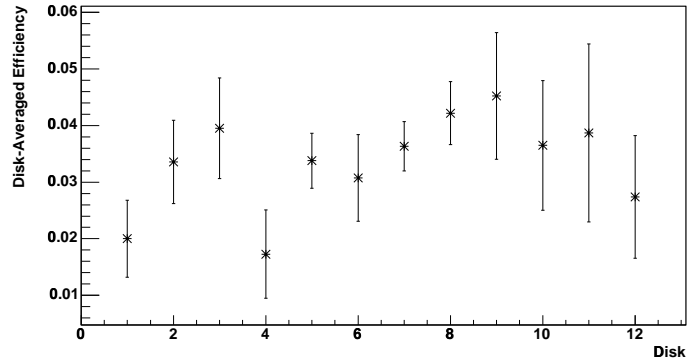
Figure 3.31: Fraction of crosses with merged clusters in data, p-side F-disks.
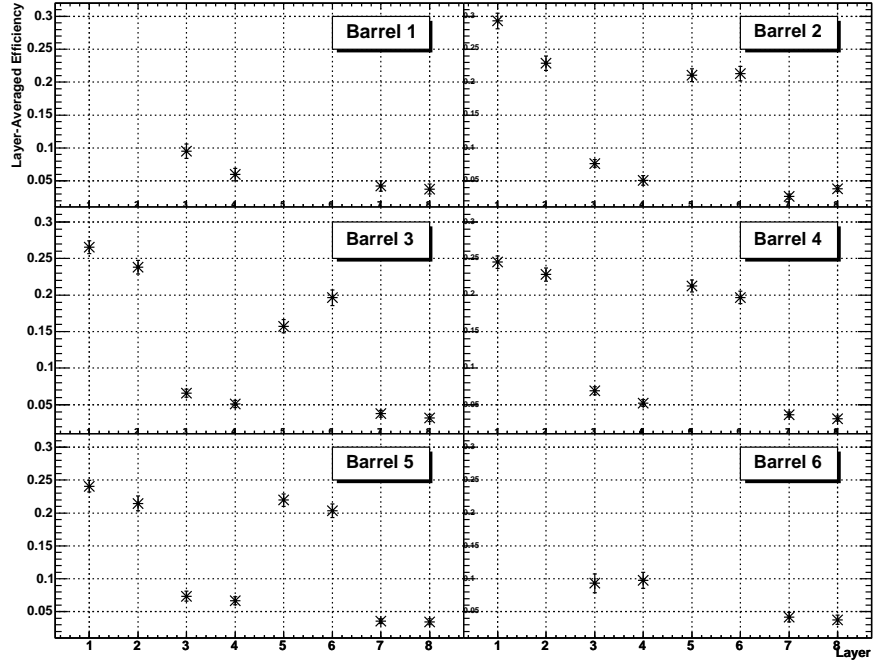
Figure 3.32: Fraction of crosses with merged clusters in data, n-side barrels.
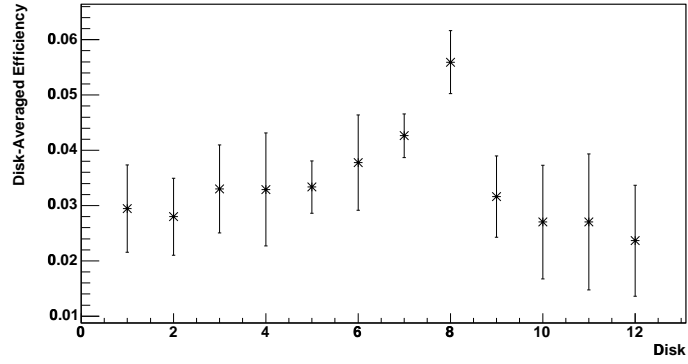
Figure 3.33: Fraction of crosses with merged clusters in data, n-side F-disks.

As merging of clusters is not related to hardware effects, it should also be observed in Monte Carlo. The determination of f_merged in Monte Carlo is performed by repeating the algorithm used for data. The layer-averaged values for f_merged in the barrels are shown in Figure 3.34 (p-side) and Figure 3.36 (n-side) and the disk-averaged values in the F-disks are shown in Figure 3.35 (p-side) and Figure 3.37 (n-side). f_merged decreases with increasing layer number, as in data, although the values are generally lower. Both F-disk distributions also show a clear z-dependence, with higher f_merged at lower $|z|$.

More generally, the Monte Carlo plots show that f_merged is dependent on the distance of a detector from the nominal interaction point and that it is introduced by tracking rather than any hardware effects. The fact that this dependence is observed equally as prominently in the barrels in both data and Monte Carlo, but much more prominently in the F-disks in Monte Carlo than in data, indicates an increased level of hardware problems in the F-disks.

While the values of f_merged in $90°$ stereo devices are typically in the range 20-30%, f_merged is quite low (less than 10%) in most other devices, for both data and Monte Carlo. However, the likelihood of having at least one merged cluster contributing to the track fit will increase with the number of SMT hits along the track.

As f_merged is higher for clusters closer to the nominal interaction point, there should be a corresponding drop in ϵ due to inefficiencies such as that shown in Figure 3.28. The plots showing ϵ for the barrels in data (Figures 3.15 and 3.17) do indeed show a decrease in ϵ at lower radii. However, it is unclear whether hardware inefficiencies like that shown in Figure 3.26 also influence the behaviour of ϵ in these plots.

As a final study, the efficiency of the $5\sigma_\text{hit}$ requirement is calculated for cases where there is a global hit associated with the track on the detector. Hardware efficiencies are then mostly eliminated and the resulting averages are shown in Figures 3.38 and 3.39 (p-side, data) and Figures 3.40 and 3.41 (p-side, Monte Carlo.) Only p-side plots are shown as all highlighted trends are the same for the n-side. In Figure 3.38, $\bar{\epsilon}_{layer}$ has much higher values than shown in Figure 3.15. The trend for decreasing $\bar{\epsilon}_{layer}$ with decreasing layer number is still present and probably corresponds to the behaviour of f_merged.

$\bar{\epsilon}_{disk}$ in Figure 3.39 contains higher values than those in Figure 3.16 as with $\bar{\epsilon}_{layer}$. The
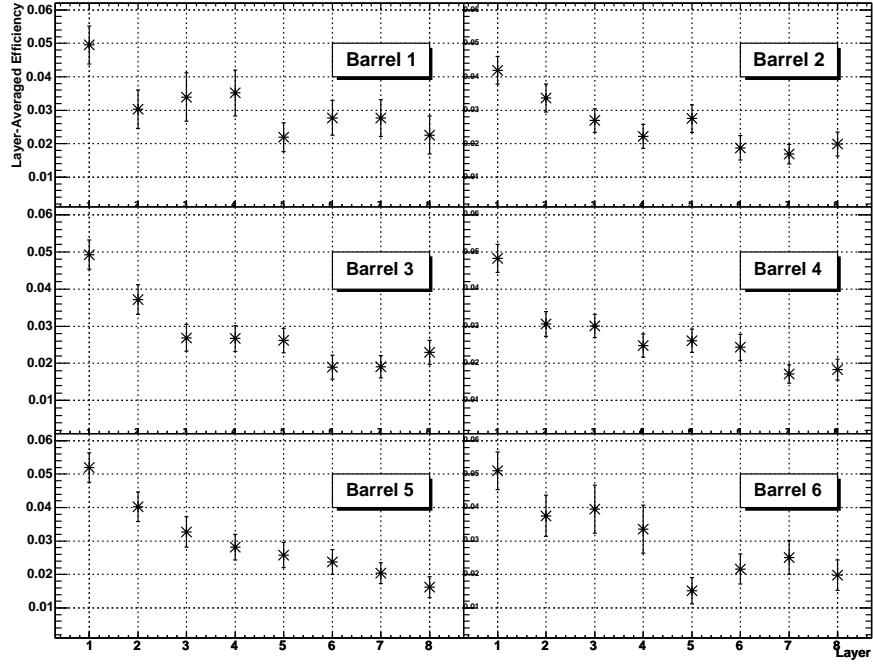
Figure 3.34: Fraction of crosses with merged clusters in Monte Carlo, p-side Barrels.
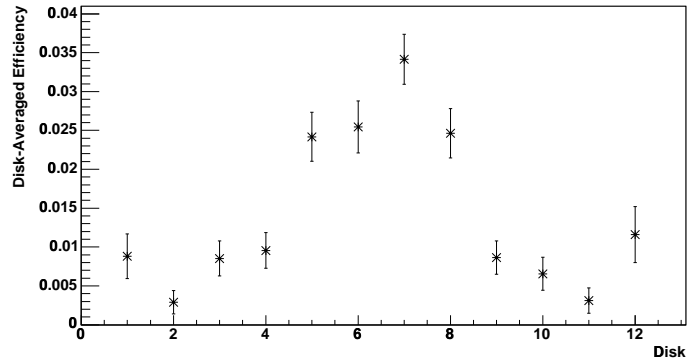
Figure 3.35: Fraction of crosses with merged clusters in Monte Carlo, p-side F-disks.

70
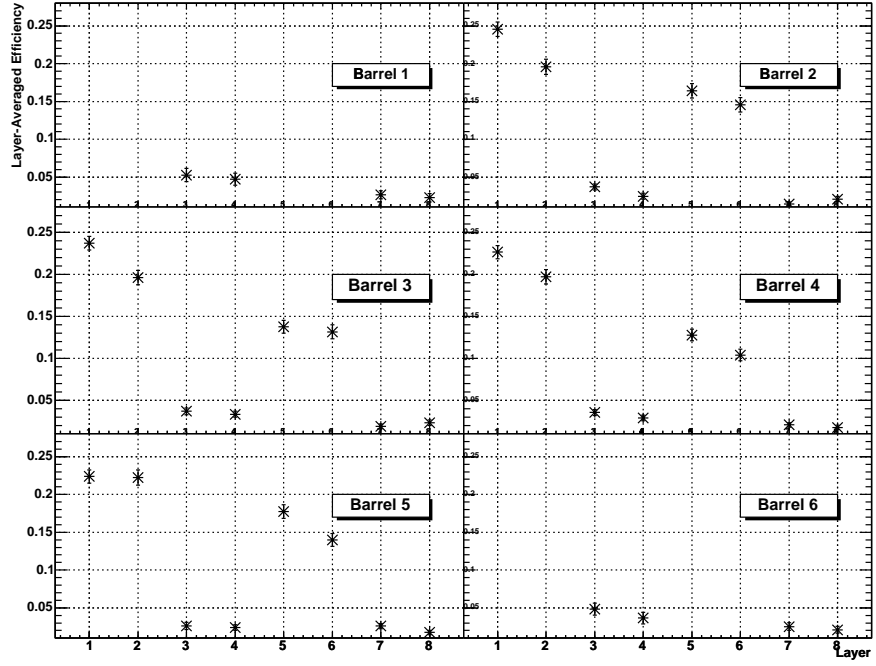
Figure 3.36: Fraction of crosses with merged clusters in Monte Carlo, n-side Barrels.
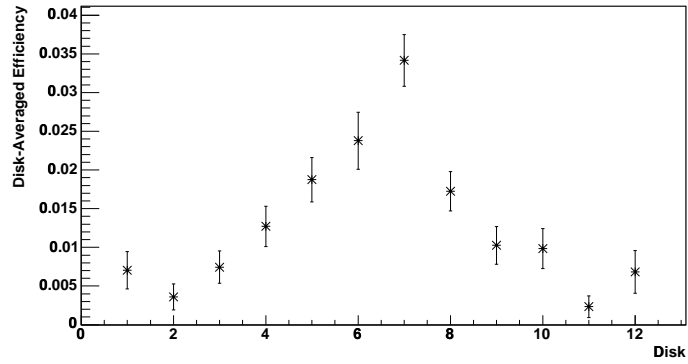
Figure 3.37: Fraction of crosses with merged clusters in Monte Carlo, n-side F-disks.
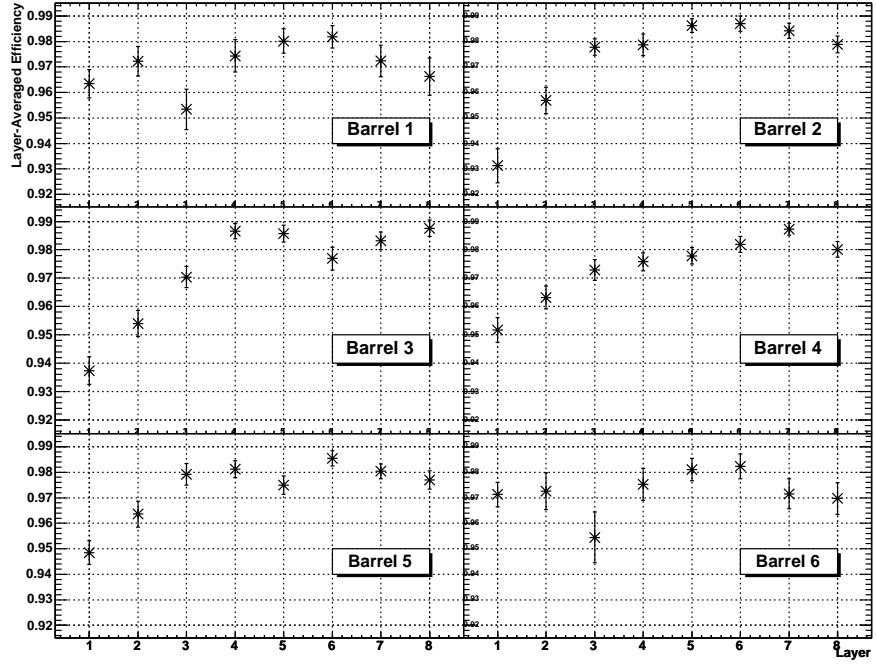
Figure 3.38: Layer-averaged p-side barrel efficiencies in data, associated 1d hits.
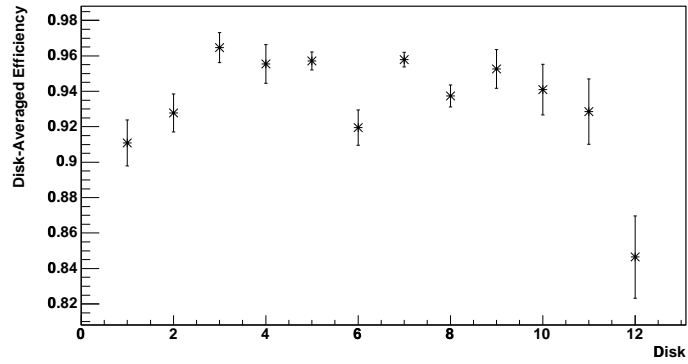
Figure 3.39: Disk-averaged p-side F-disk efficiencies in data, associated 1d hits.
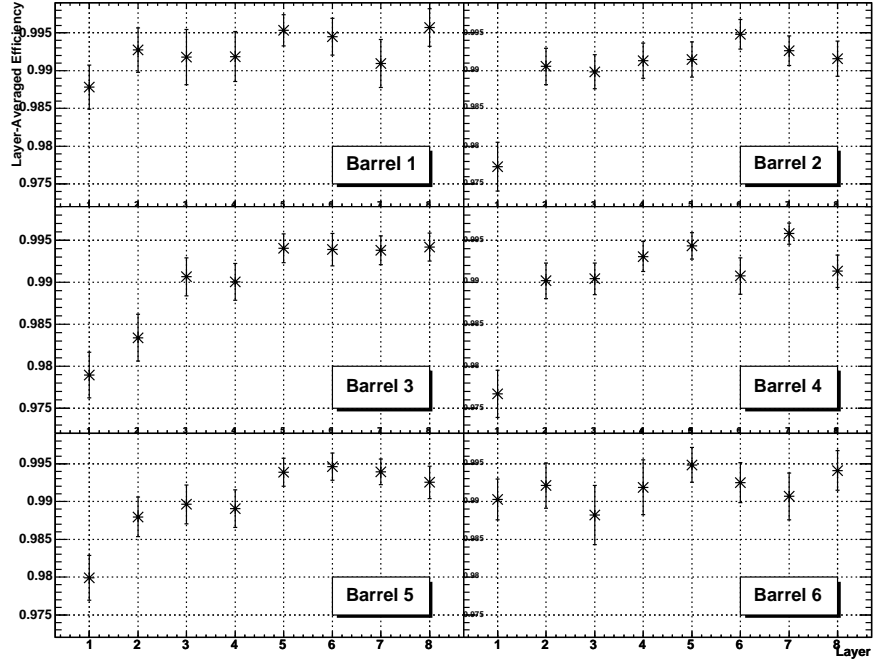
Figure 3.40: Layer-averaged p-side barrel efficiencies in Monte Carlo, associated 1d hits.
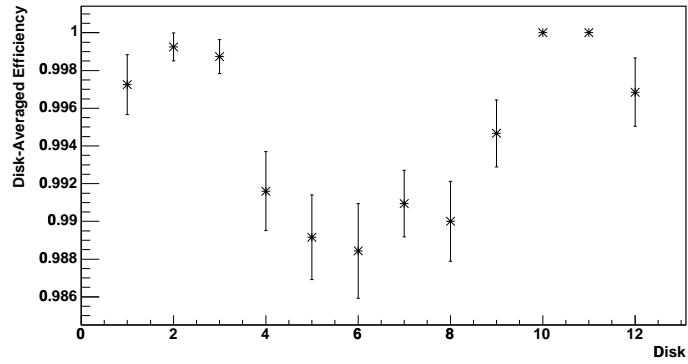
Figure 3.41: Disk-averaged p-side F-disk efficiencies in Monte Carlo, associated 1d hits.

reduction of efficiency with decreasing distance from the nominal interaction point is not reflected. However, the increased size of the error bars indicates that the number of track crossings were reduced by requiring an associated hit and excluding hardware problems. Once more, this suggests hardware problems in the F-disks.

As discussed in Section 3.5, grassy noise is a common problem in the F-disks. This is the most likely explanation for the observed trends in $\bar{\epsilon}_{disk}$ and f_{merged} in the F-disks shown in Figures 3.16, 3.18, 3.31 and 3.33.

The values for ϵ shown in Figures 3.40 and 3.41 are higher than those given in Figures 3.19 and 3.20 with no associated hit requirement. The difference is less pronounced than that shown in data and may come from inefficiencies in the tracking algorithm.

A study of the performance of the DØ SMT has been presented by looking at the behaviour of ϵ, the efficiency per detector of finding a 1d hit within $5\sigma_{\mathrm{hit}}$ of the no-hit track crossing position. As well as presenting values for this efficiency, it has been found that ϵ has a dependency on displacement from the nominal interaction point arising from tracking. On closer inspection, the dependency seems to be linked to f_{merged}, the fraction of track crossings per detector featuring a merged cluster. Combined with Figure 3.28, this observation gives a strong indication that the overall tracking performance is affected by merged clusters.

The performance study also indicates that there are hardware problems in the F-disks. The probable cause for this is grassy noise.

If repeated, the study would benefit from using higher statistics. It would be interesting to investigate the effectiveness of a splitting algorithm for overlapping charge distributions during clustering.

74

Chapter 4

Considerations for a τ-based Analysis

The effective measurement of τ leptons is an important part of the physics program at DØ. As well as forming the basis for current electroweak analyses, τs are expected to contribute to searches for the neutral Standard Model Higgs, the charged Higgs and supersymmetry [41], [10].

The τ lepton has a mass of $1776.99^{+0.29}_{-0.26} MeV/c^2$ and decays with a mean lifetime of (290.6 ± 1.1) fs [5]. The main decays of the τ are shown in Table 4.1. So-called '1-prong' decays feature a single charged particle and represent roughly 85% of all τ decays. The charged particle is either a lepton or a hadron. '3-prong' decays feature three charged particles and are exclusively hadronic. Roughly 15% of all τ decays are 3-prong.

The τ-ID group at DØ currently uses $Z^0 \to \tau^+\tau^-$ events with one hadronic τ decay and one leptonic τ decay to measure $\sigma(\text{p}\bar{\text{p}} \to Z^0)$. $\text{Br}(Z^0 \to \tau^+\tau^-)$ [49], where $\sigma(\text{p}\bar{\text{p}} \to Z^0)$ is the cross-section for Z^0 production and $\text{Br}(Z^0 \to \tau^+\tau^-)$ is the branching ratio to two τs. Lifetime information is not currently used in the event selection and could help to improve the measurement. It is therefore interesting to study the effectiveness of the τ lifetime as a tool for τ identification.

The lifetime of the b-quark is currently used for tagging b-jets at DØ. These methods involve secondary vertices or impact parameters. In τ events, it is only possible to reconstruct a secondary vertex from a 3-prong decay. This would involve the accurate identification of three charged hadrons close together in the calorimeter with well-

Decay	Branching Ratio
1-prong	(85.35 ± 0.07) %
$\tau^- \to \mu^- \bar{\nu}_\mu \nu_\tau +$ anything	(17.36 ± 0.06) %
$\tau^- \to e^- \bar{\nu}_e \nu_\tau +$ anything	(17.84 ± 0.06) %
$\tau^- \to h^- \nu_\tau$	(12.30 ± 0.11) %
$\tau^- \to h^- \nu_\tau +$ neutrals	(36.92 ± 0.14) %
3-prong	(15.19 ± 0.07) %
$\tau^- \to h^- h^- h^+ \nu_\tau$	(10.01 ± 0.09) %
$\tau^- \to h^- h^- h^+ \nu_\tau +$ neutrals	(5.19 ± 0.10) %
5-prong	$(1.00 \pm 0.06) \times 10^{-3}$
$\tau^- \to 3h^- 2h^+ \nu_\tau$	$(8.2 \pm 0.6) \times 10^{-4}$

Table 4.1: Decays of the τ^- lepton.

measured associated tracks. DØ is well equipped to identify electrons and muons, so impact parameters in 1-prong leptonic τ decays are preferred in this analysis.
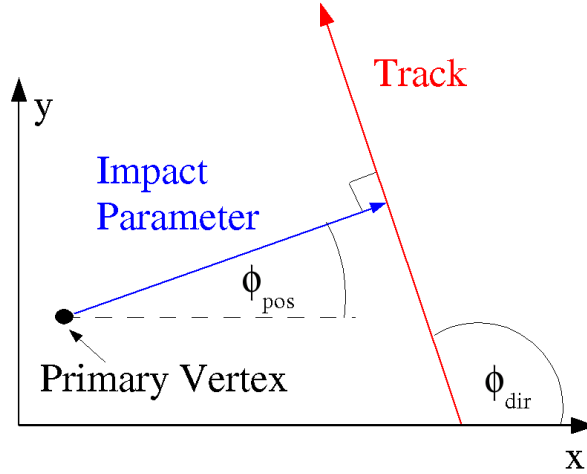
Figure 4.1: Diagram showing the impact parameter of a track calculated with respect to the primary vertex.

By default, tracks at DØ are calculated with a signed impact parameter with respect to the primary vertex. This is illustrated in Figure 4.1. The magnitude of the impact parameter is the distance of closest approach of the track in the $r\phi$ plane to the line parallel to the z-axis that intersects the primary vertex. ϕ_{pos}, as indicated in the

diagram, is the angle between the x-axis and the impact parameter vector pointing from the primary vertex to the track. ϕ_{dir} is also indicated in the diagram and is the angle between the x-axis and the track direction. By definition, the difference between these two angles is a right angle but can have either a positive or negative sign. This sign is given to the impact parameter.

The nature of the impact parameter calculation presents an immediate problem. The primary vertices in fully reconstructed data are more likely to include tracks that have higher p_{T} and are better measured in the central tracker. A well-measured high-p_{T} track produced by a leptonic τ decay is therefore likely to contribute and the lifetime information is lost as the primary vertex is biased towards this track.

The two possible solutions to this problem considered here are

- Performing an event-level refit of the primary vertex, excluding tracks matched to τs.

- Recalculating the impact parameters with respect to the position of the beam.

These solutions are considered in Sections 4.1 and 4.2.

4.1   Refitting of Primary Vertex

If the tracks resulting from τ decays are excluded from a leptonic $Z^0 \to \tau^+\tau^-$ event, only tracks from the underlying event remain. The underlying event refers to the hadronic system made up of the proton and antiproton remnants. Tracks in this system tend towards the forward region and low p_{T} so in general they are less well measured.

It is possible to investigate the effectiveness of refitting the primary vertex to the underlying event by looking at the primary vertices in 'minimum bias' events. Minimum bias events are triggered by requiring a coincidence in the Luminosity Monitors at the two ends of the detector. This trigger has a high efficiency for all inelastic $p\bar{p}$ collisions in which both p and $\bar{p}$ fragment. This means that the triggered events are dominated by softly scattering hadronic events containing proton and antiproton remnants.

All minimum bias events from one run are selected. The first choice primary vertex in reconstructed data has to be of sufficiently low fit χ^2 and have the highest $\Sigma \log(p_{\mathrm{T}})$ [18]

which refers to the p_T in all tracks included in the vertex fit. The primary vertices from all selected minimum bias events are binned according to vertex z in 1 cm bins and the distributions in x and y are plotted.
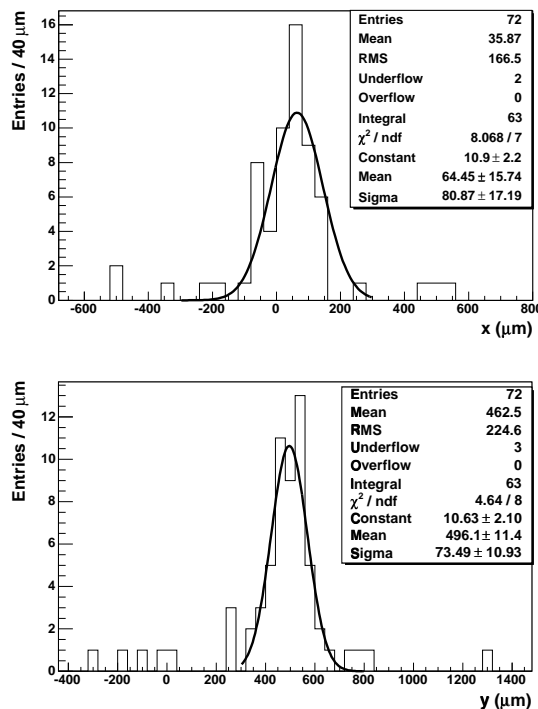
Figure 4.2: x (top plot) and y (bottom plot) position of the primary vertex in minimum bias events, plotted for -3 cm $< z < -2$ cm.

Figure 4.2 shows these distributions for the z-bin -2 cm $< z < -3$ cm. The distributions contain low statistics as a run in general contains more triggered hard scatter events than minimum bias events due to prescaling. However, it is important that all considered minimum bias events are taken from the same run since the beam position may move significantly between runs. The width of these distributions provides a measure of the vertex resolution in these events. The distributions clearly have non-Gaussian contributions, probably resulting from badly-measured vertices. The peaks have widths of roughly 70–80 μm.

4.2 Measurement of Beam Position Per Run

During normal data-taking, the configuration of the beam-focussing magnets is not changed and the beam shape therefore remains approximately constant. A typical run

represents a few hours of data-taking and contains over a hundred thousand events. It is therefore possible to take many primary vertices from the same run to construct an accurate layout of the beam shape and understand whether a measurement of the beam position is useful for calculating impact parameters in events with lifetime.

As many events are available per run, it is no problem to discard those containing badly-measured primary vertices. To find a set of quality cuts for primary vertices, 20,000 events from the same run are examined. Figure 4.3 shows the χ^2 per degree of freedom (χ^2/ndof) for the primary vertex fit against the number of tracks included (n_{track}). At high n_{track}, the χ^2/ndof is well-behaved with values distributed around 1. At low n_{track}, the χ^2/ndof has a much larger range which implies a higher number of less well measured vertices.

Figure 4.4 shows the uncertainty on the primary vertex position in x and y, σ_x and σ_y respectively, plotted against χ^2/ndof. In very badly-measured vertices, σ_x and σ_y are truncated to a value of 100, which can be seen in the plots. It can also be seen that well-measured primary vertices tend towards low σ_x or σ_y and low χ^2/ndof.

From these observations, the following cuts seem reasonable

- $n_{\mathrm{track}} \geq 6$

- $\sigma_x < 40 \ \mu\mathrm{m}$

- $\sigma_y < 40 \ \mu\mathrm{m}$

To see how these cuts improve a sample of primary vertices for the purpose of measuring a beam position, they are applied to a sample of 100,000 events from the same run used to produce Figures 4.3 and 4.4, thus giving a 'before' and 'after' sample. The primary vertices in both samples are binned according to vertex z in 1 cm bins and the distributions in x and y are then plotted. The distributions from both samples in the z-bin -2 cm $< z < -3$ cm are shown in Figures 4.5 and 4.6. All peaks can be seen to follow a Gaussian distribution, indicating that the beam has a Gaussian shape. In the plots for the sample with cuts applied, there are very few badly measured vertices lying away from the peak and the histogram RMS is close to the fitted Gaussian width. The cuts are therefore assumed to be effective.

Having found cuts to improve the primary vertex selection for measuring the beam shape, it is now important to understand whether the measured beam shape can

Number of Tracks in Vertex Fit vs.χ^2/ndof

Entries		17423
Mean x		9.604
Mean y		1.911
RMS x		6.029
RMS y		2.034
0	11	0
0	12936	4181
0	295	0
Integral		1.294e+04
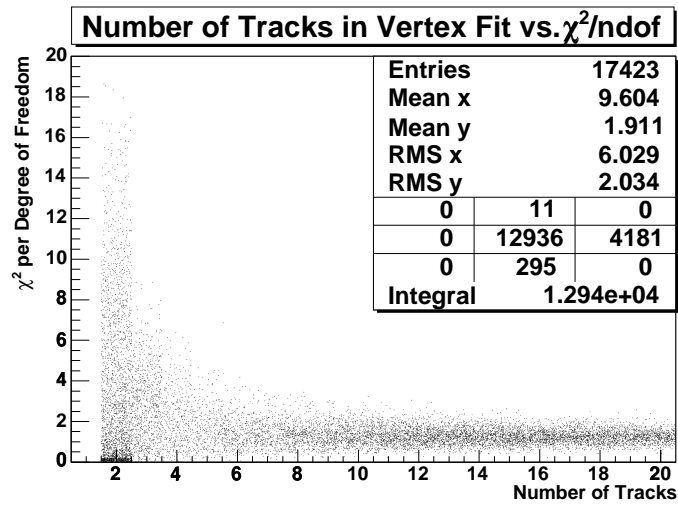
Figure 4.3: Number of tracks associated with primary vertex fit against χ^2 per degree of freedom.

χ^2/ndof vs. Error on Vertex x-position

Entries		17423
Mean x		1.746
Mean y		34.8
RMS x		1.796
RMS y		28.49
0	0	0
295	17117	11
0	0	0
Integral		1.712e+04

χ^2/ndof vs. Error on Vertex y-position

Entries		17423
Mean x		1.746
Mean y		34.54
RMS x		1.796
RMS y		28.29
0	0	0
295	17117	11
0	0	0
Integral		1.712e+04
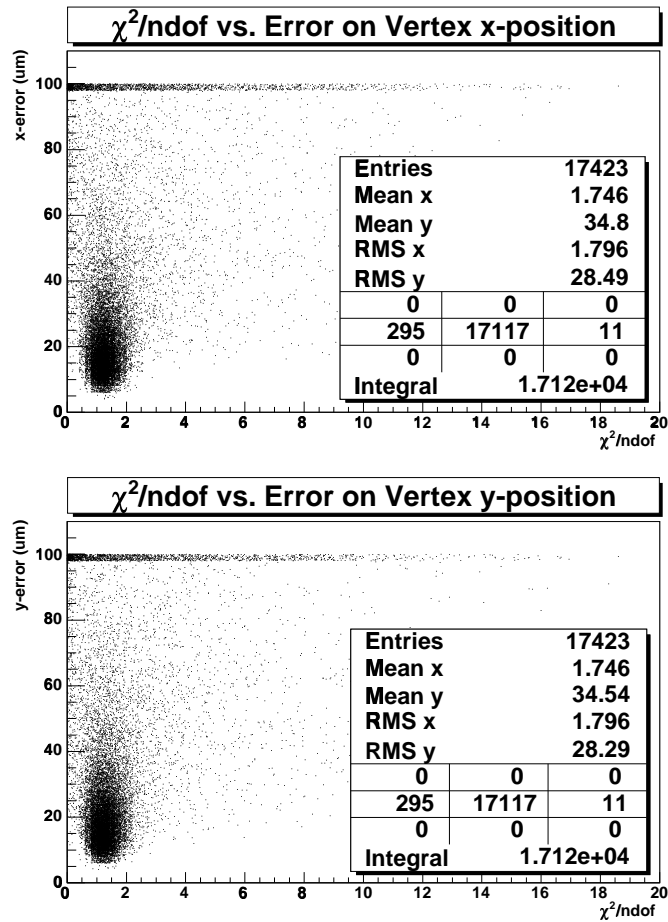
Figure 4.4: Error on primary vertex x-position (top) and y-position (bottom) against χ^2 per degree of freedom.
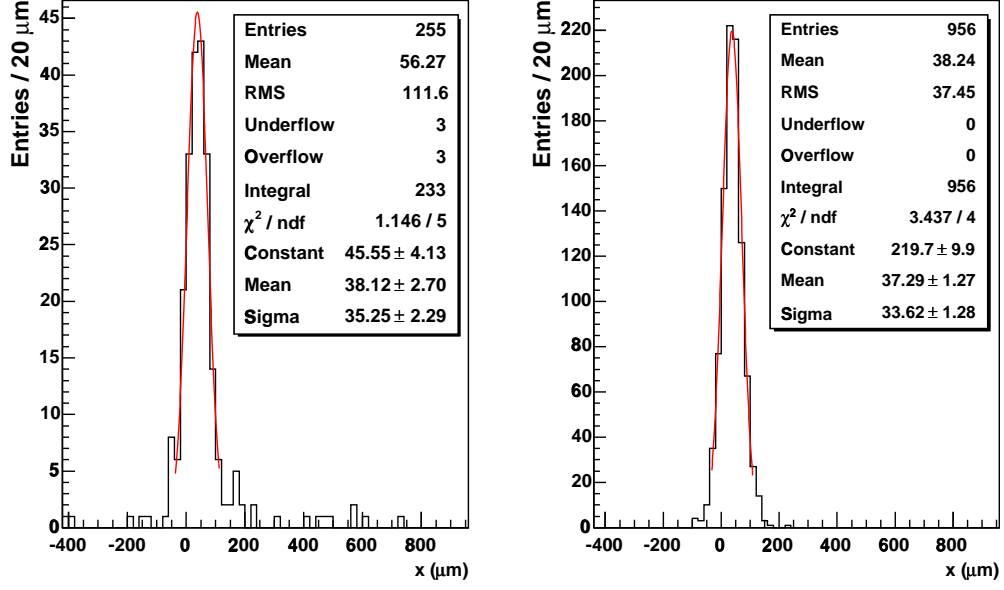
Figure 4.5: Primary vertex x-position in bin -3 cm $< z < -2$ cm with no vertex cuts (left) and with vertex cuts applied (right).
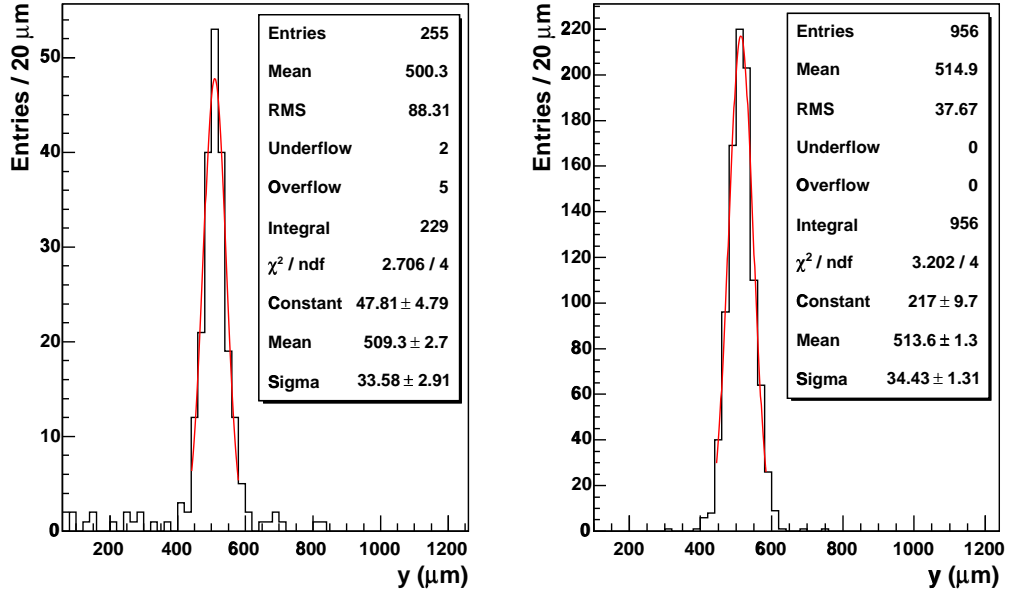
Figure 4.6: Primary vertex y-position in bin -3 cm $< z < -2$ cm with no cuts (left) and with cuts applied (right).

be useful for lifetime analysis. Taking 100,000 events from the same run and again binning the primary vertices in 1 cm bins in z, the x and y distributions are fitted with a Gaussian as in Figures 4.5 and 4.6. The mean positions (μ_x and μ_y) and standard deviations (σ_x and σ_y) are plotted against z in Figures 4.7 and 4.8 respectively. The range of z-values considered, -50 cm $< z < +50$ cm, is sufficient as the active interaction region has a Gaussian width of approximately 25 cm in the beam direction. The mean positions have been fitted with a straight line. It can be seen that the tilt of the beam, $\frac{dx}{dz}$ and $\frac{dy}{dz}$, is non-negligible and needs to be measured in order to calculate impact parameters with respect to the appropriate beam position.

The standard deviations have been fitted with parabolas. This is the expected behaviour for a beam of particles with a Gaussian distribution whose width varies with z [21] and there does seem to be good agreement in the fit range. The fits were performed in the range -30 cm $< z < +30$ cm to avoid the uncertain measurements at high $|z|$. The measured beam width varies between roughly 40–50 μm for most of the interaction region in both x and y. The minimum value for both fits is 39–40 μm at roughly $z = 0$. The beam shape therefore seems to be approximately circular in $r\phi$. The distribution of measured primary vertices is actually a convolution of the implicit primary vertex distribution and the primary vertex resolution. This implies the following equation in the $r\phi$ plane

$$\sigma^2_{\text{observed}} = \sigma^2_{\text{implicit}} + \sigma^2_{\text{vertex}}$$

where σ_{observed} is the observed beam width, σ_{implicit} is the implicit beam width and σ_{vertex} is the primary vertex resolution. σ_{vertex} is usually 15–30 μm [33], although the primary vertices considered here should be at the lower end of this range due to the quality cuts applied. The implicit beam width is therefore lower than the observed beam width and is estimated to have a minimum value of approximately 30 μm.

The refitted primary vertices investigated in Section 4.1 had a rough width of 70–80 μm and a high incidence of bad measurements. It is therefore clear that calculating impact parameters with respect to a measured beam position is preferable to refitting the primary vertex after excluding tracks matched to τs in $Z^0 \to \tau^+\tau^-$ events.

The method given above for measuring the beam position requires a large number of events per measurement, requiring a lot of computing resources. It was possible

82
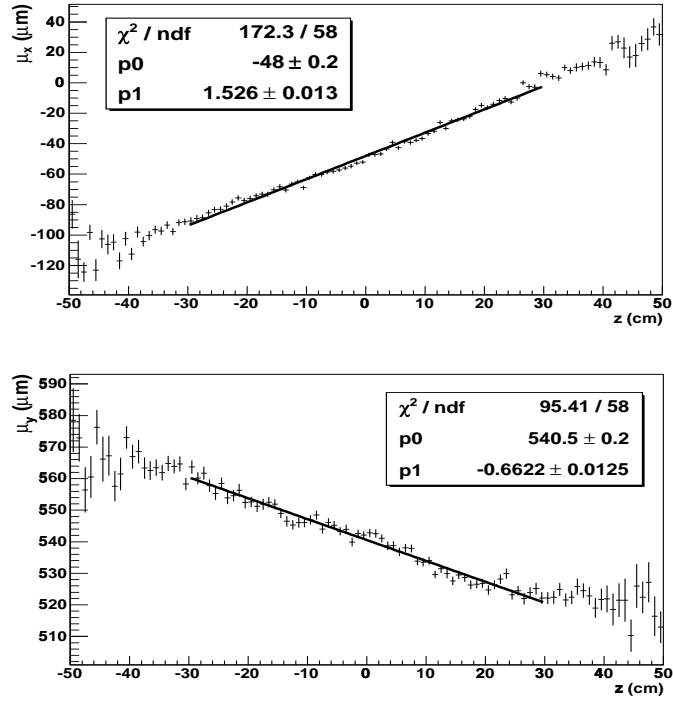
Figure 4.7: Mean x (top plot) and mean y (bottom plot) plotted as a function of z, run 180138.
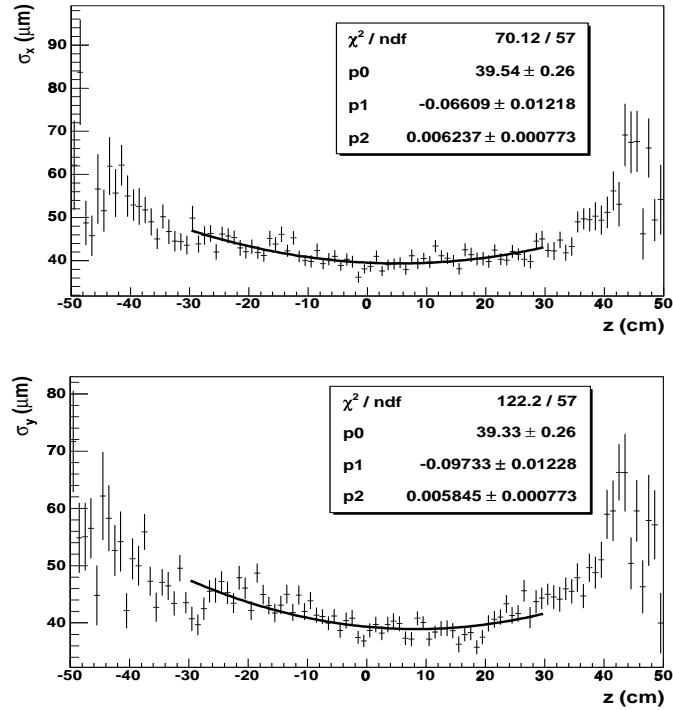
Figure 4.8: σ_x (top plot) and σ_y (bottom plot) plotted as a function of z, run 180138.
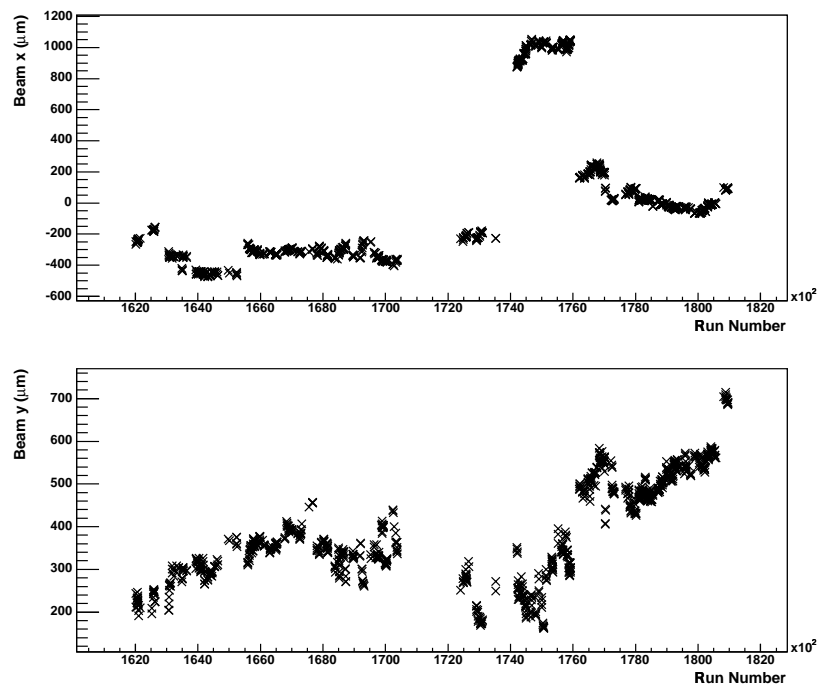
Figure 4.9: Beam position at $z = 0$ in x (upper plot) and y (lower plot) plotted against run number.

to measure the beam position for 438 separate runs, requiring at least 80,000 events per run to ensure an accurate measurement. Using this information, the variation of the beam position at $z = 0$ with time is shown in Figure 4.9. Jumps in value of order 100 μm can be seen between runs. This indicates the need to measure the beam positions per run as an overall measurement for the DØ dataset would clearly be meaningless.

After calculating the beamspots shown in Figure 4.9, it became standard during the offline reconstruction of data to perform a linear fit to the 3-dimensional coordinates for all primary vertices in each new run [34]. This technique is a lot quicker than considering primary vertices in separate z-bins. The linear fit was also performed for all earlier runs in the DØ dataset, thus providing a list of beam positions for every recorded run.

Figure 4.10 shows the difference between the beam position at $z = 0$ calculated with the binning technique described above and with the direct linear fit used in the standard DØ event reconstruction. The two techniques show very good agreement. While the binning method has provided valuable information about the shape of the

84

Entries / 0.4 μm (upper plot)

Entries	438
Mean	-0.4918
RMS	2.864
Underflow	1
Overflow	0
Integral	437
χ^2 / ndf	31.09 / 39
Constant	28.46 ± 1.872
Mean	-0.4665 ± 0.1169
Sigma	2.293 ± 0.1044

δ_x (μm)

Entries / 0.4 μm (lower plot)

Entries	438
Mean	-0.3453
RMS	2.679
Underflow	0
Overflow	2
Integral	436
χ^2 / ndf	27.21 / 41
Constant	30.06 ± 1.923
Mean	-0.4423 ± 0.1097
Sigma	2.174 ± 0.0894

δ_y (μm)
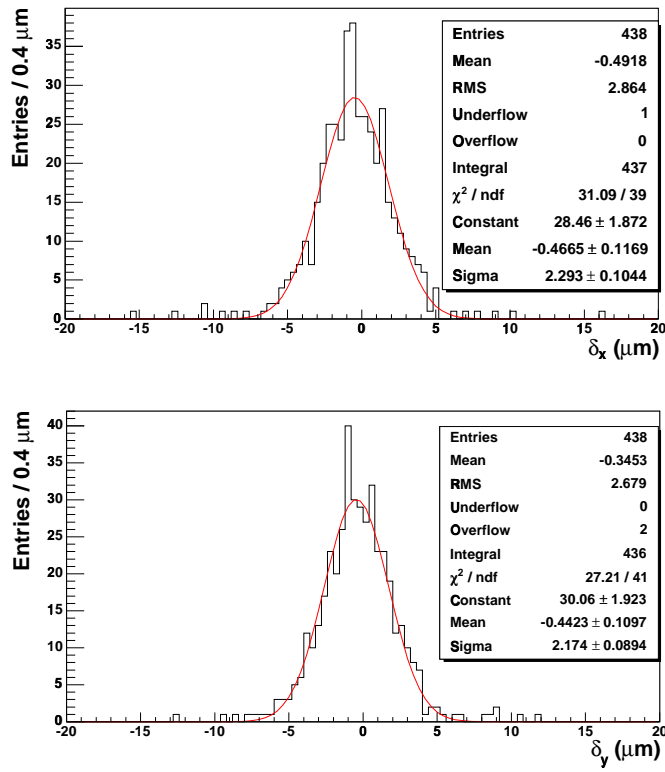
Figure 4.10: Differences in x (upper plot) and y (lower plot) between mean vertex positions calculated at $z = 0$ using the binning method described here and a direct linear fit to 3-dimensional vertex coordinates.

beam, the beam positions from the linear fit can be used for all data produced at DØ and will be used for calculating all impact parameters in this analysis.

4.3   Impact Parameters in Data and Monte Carlo

Having found a method for measuring unbiased impact parameters in events with lifetime, it is useful to look at impact parameters for tracks from leptonic τ decays in Monte Carlo. To check whether any observed behaviour will also be noticeable in data, it is first necessary to make a comparison of impact parameters in data and Monte Carlo. A reliable sample of $Z^0 \rightarrow \mu^+\mu^-$ events can be selected in data as this is a relatively clean channel with low background contribution. Samples of $Z^0 \rightarrow \mu^+\mu^-$ events are therefore selected in Monte Carlo with the full detector reconstruction and data. The cuts used to select $Z^0 \rightarrow \mu^+\mu^-$ events are as follows:

- Two reconstructed muons of 'medium' quality. In this analysis, a muon of

medium quality has at least one A-layer scintillator hit, at least two A-layer wire hits, at least one B or C-layer scintillator hit and at least two B or C-layer wire hits.

- Each muon must be matched to a central track with at least two hits from separate SMT superlayers and seven hits from separate CFT superlayers. A local muon is matched to a central track if the local muon and central track can be successfully combined in a track fit.

- The track matched to each muon must have $p_{\rm T} > 15$ GeV/c. The $p_{\rm T}$ of the central track is used for the $p_{\rm T}$ cut as it is more accurately measured than the local muon $p_{\rm T}$.

- Each muon must be within the full acceptance of the muon chambers. The position measured in the muon chambers must be $|\eta| < 1.8$ but the region $|\eta| < 1.25, 4.25 < \phi < 5.15$ is excluded. This region is only partially instru-mented as it contains mechanical supports for the DØ detector.

- Both muons are isolated in the tracker and calorimeter. To isolate a muon in the tracker, the tranverse momenta for tracks within $\delta R < 0.5$ of the matched track are summed, where $\delta R = \sqrt{\delta\phi^2 + \delta\eta^2}$. This sum ($\Sigma {\rm p}_{\rm T}^{\rm track}(0.5)$) is required to be less than 3.5 GeV/c. To isolate a muon in the calorimeter, the transverse energies of EM calorimeter cells between $0.1 < \delta R < 0.4$ from the matched track are summed. This sum ($\Sigma {\rm E}_{\rm T}^{\rm cal}(0.1, 0.4)$) is required to be less than 2.5 GeV.

- The difference in the measured time at the muon A-layer between the muons must be less than 9 ns. This cut rejects background from cosmic rays in data.

- The measured charge of the two muons must be opposite.

- $\delta\phi > 2$ between the two tracks.

- The invariant mass of the dimuon system must exceed 65 GeV/c^2.

- In Monte Carlo, the reconstructed muons are matched to generated muons by requiring $\delta R < 0.1$ between the matched track and the generated muon position.

The dimuon invariant mass is calculated using the momenta of the two matched tracks. Figure 4.11 compares the dimuon invariant mass in data and Monte Carlo. Both
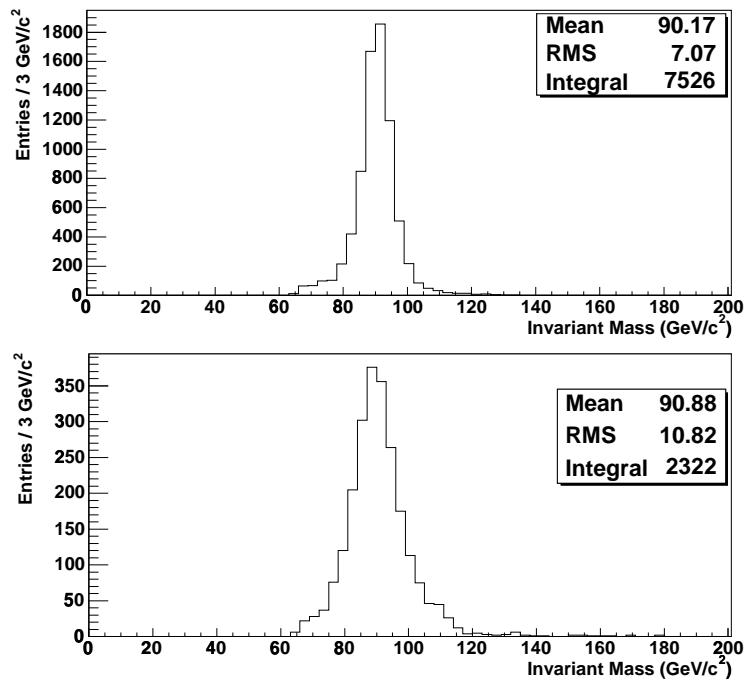
Figure 4.11: Invariant mass of dimuon system in $Z^0 \rightarrow \mu^+\mu^-$ events from Monte Carlo (upper plot) and data (lower plot).

plots have a similar shape, indicating that the data sample is dominated by genuine $Z^0 \rightarrow \mu^+\mu^-$ events. However, the Z^0 peak is substantially wider in data, indicating that the tracking resolution is underestimated in Monte Carlo. The rapidity and transverse momentum of the Z^0 in Monte Carlo and data are shown in Figure 4.12. These quantities are calculated with the reconstructed muon track information in both samples and in the case of the Monte Carlo, they are also calculated using the Z^0 truth information.

Figure 4.13 shows impact parameters calculated with respect to the beam position in $Z^0 \rightarrow \mu^+\mu^-$ data and Monte Carlo. In Monte Carlo, the beam is simulated with a central value of (0,0) in xy and no tilt. The simulated beam width varies as z^2 about a minimum of 30 μm in both x and y. The impact parameter distributions show Gaussian behaviour and the agreement between data and Monte Carlo is very close, with very similar values for the Gaussian width. As $Z^0 \rightarrow \mu^+\mu^-$ is a channel with no lifetime in the decay, the width of the impact parameter distribution takes contributions from the implicit beam width and the tracking resolution. It is possible that these two factors combine in different amounts to produce the same width in data and Monte Carlo but for now, the similar Gaussian widths are taken to indicate
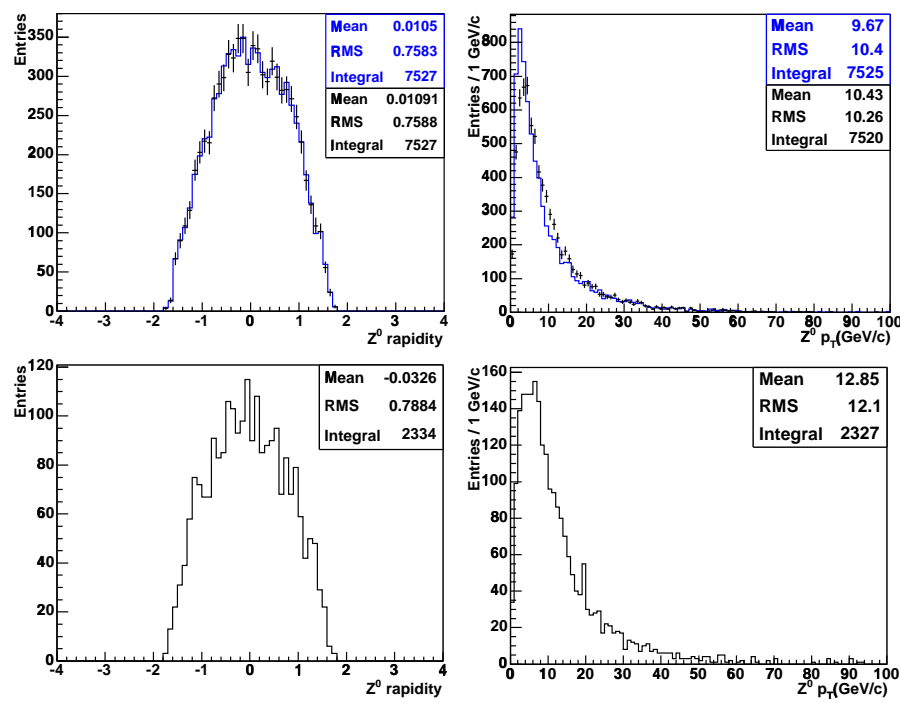
Figure 4.12: Rapidity (left) and transverse momentum (right) of the Z^0 boson in $Z^0 \to \mu^+\mu^-$ events from Monte Carlo (upper plot) and data (lower plot). In the Monte Carlo plots, the blue line is calculated from truth information while the black points with errors are calculated from reconstructed muon tracks.

that data and Monte Carlo are in good agreement.

In Figure 4.14, the impact parameter of the first muon is plotted against the impact parameter of the second muon for the selected $Z^0 \to \mu^+\mu^-$ samples. The impact parameters tend towards the line $x = -y$ in both plots, although this trend is most noticeable in the plot from Monte Carlo. The spread of points along $x = -y$ is caused by the width of the beam while the spread of points transverse to $x = -y$ is caused by the resolution of tracking.

A sample of $Z^0 \to \tau^+\tau^- \to l^\pm l^\mp$ events is selected to investigate the behaviour of signed impact parameters in leptonic τ decays, where l is a lepton. Truth information is used to match tracks with $p_T > 10\ \mathrm{GeV}/c$, at least two SMT hits and at least seven CFT hits to generated leptons from τ decays. The match requires $\delta R < 0.1$ between a track and a generated lepton. The tracks must also have a ϕ separation greater than 2. The p_T cut represents a compromise between making a fair comparison with the tracks in the $Z^0 \to \mu^+\mu^-$ samples and having reasonable statistics for this study.
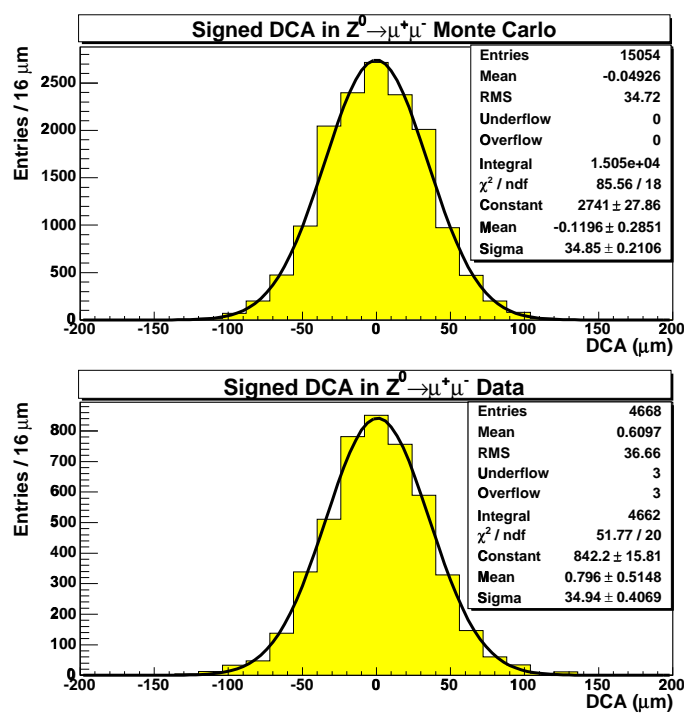
Figure 4.13: Signed impact parameters with respect to the beam position in $Z^0 \rightarrow \mu^+\mu^-$ events from Monte Carlo (upper plot) and data (lower plot).

Figure 4.15 shows the rapidity and transverse momentum of the Z^0 in the selected $Z^0 \rightarrow \tau^+\tau^- \rightarrow l^\pm l^\mp$ sample using the Z^0 truth information.

Figure 4.16 shows the signed impact parameter of the first lepton plotted against the signed impact parameter of the second lepton. The first lepton is always the product of the τ^+ while the second lepton is always the product of the τ^-. The tendency towards $x = -y$ seen in the corresponding plots for $Z^0 \rightarrow \mu^+\mu^-$ is not observed. This implies a contribution from lifetime large enough to smear out the effects of the beam width and tracking resolution. A comparison of Figures 4.14 and 4.16 suggests it may be useful to look at the sum of the two signed impact parameters in back-to-back systems as a discriminant for events with lifetime. The observed trend towards $x = -y$ in events without lifetime suggests that these events tend towards a low sum of signed impact parameters while events with lifetime have more of an extended distribution.

The absolute sum of the signed impact parameters is shown in Figure 4.17 for the selected $Z^0 \rightarrow \mu^+\mu^-$ samples in data and Monte Carlo. The absolute value is plotted because the sign reveals no useful information and the statistics are approximately
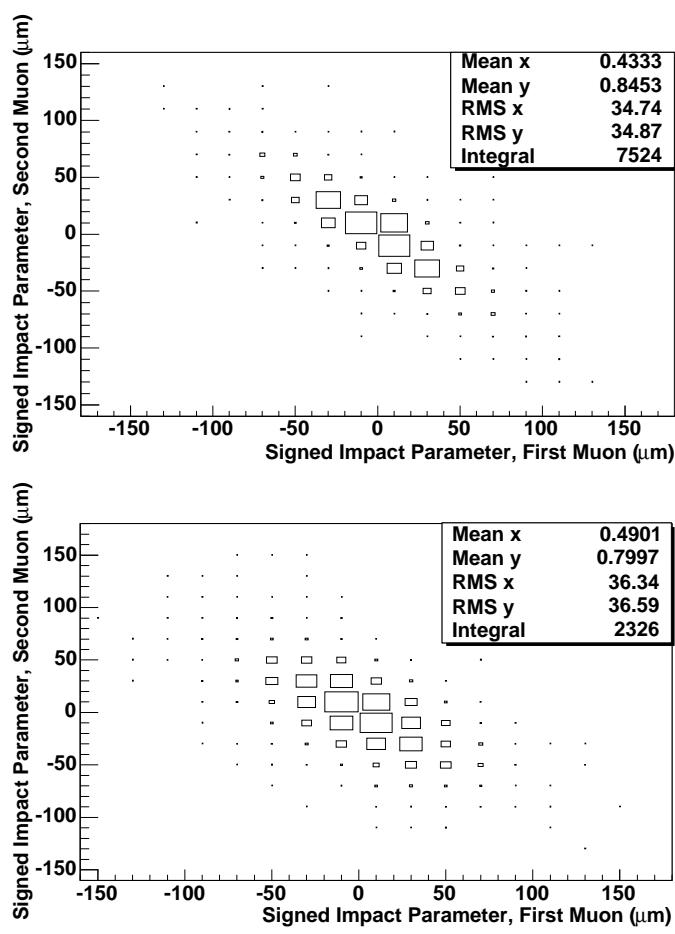
Figure 4.14: Signed impact parameter of first muon against signed impact parameter of second muon in $Z^0 \to \mu^+ \mu^-$ events from Monte Carlo (upper plot) and data (lower plot).
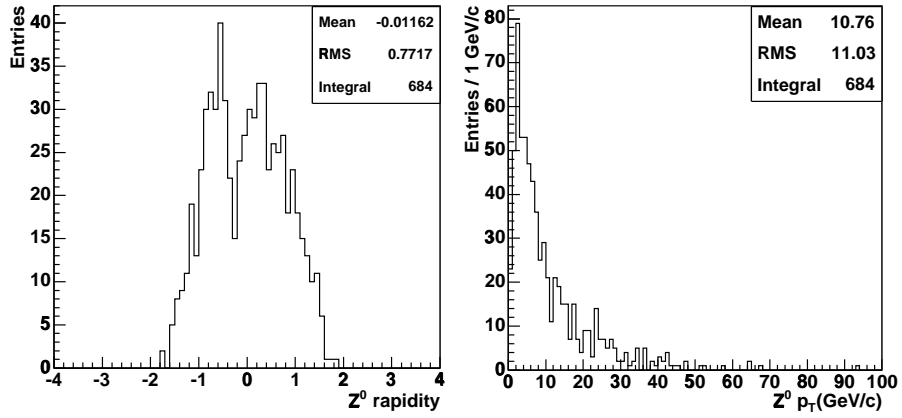
Figure 4.15: Rapidity (left) and transverse momentum (right) of the Z^0 boson in $Z^0 \to \tau^+ \tau^- \to l^\pm l^\mp$ events from Monte Carlo.
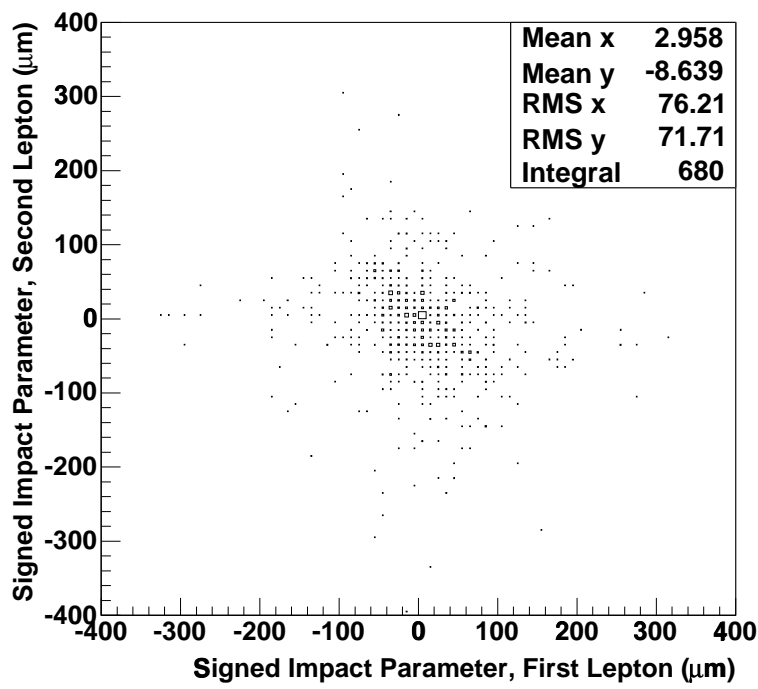
Figure 4.16: Signed impact parameter of first lepton against signed impact parameter of second lepton in $Z^0 \rightarrow \tau^+\tau^-$ Monte Carlo events with two leptonic decays.

doubled in each bin. Both distributions look roughly Gaussian and have been fitted as such with a fixed mean value of 0. In both cases, the distribution is narrower than the individual impact parameter distribution shown in Figure 4.13, although this effect is much more pronounced for the $Z^0 \rightarrow \mu^+\mu^-$ Monte Carlo. By summing the impact parameters, the contribution from the beam width is reduced as the two muons are correlated. The widths in Figure 4.17 are more a reflection of the tracking resolution and the difference between the widths in data and Monte Carlo again points to an underestimation of the tracking resolution in Monte Carlo.

Figure 4.18 shows the absolute sum of signed impact parameters in the selected $Z^0 \rightarrow \tau^+\tau^- \rightarrow l^\pm l^\mp$ Monte Carlo sample. This distribution is much wider than both of the distributions shown in Figure 4.17 and does not look Gaussian. An exponential fit has instead been applied and there is a good fit. Decay lifetimes have an exponential distribution so this suggests that the lifetime of the τ decay is the dominant effect. Despite the differences between the absolute sum of signed impact parameters in $Z^0 \rightarrow \mu^+\mu^-$ data and Monte Carlo, the large effect seen in Figure 4.18 resulting from the τ lifetime suggests that the absolute sum of signed impact parameters could be a useful discriminating variable for back-to-back systems decaying with lifetime. In

91

Mean		13.17
RMS		12.16
Integral		7527
χ^2 / ndf		252.2 / 13
Gauss Norm	3589 ± 59.22	
Gauss Mean	0 ±	0
Gauss Sigma	16.17 ± 0.1878	

Mean		22.96
RMS		20.15
Integral		2334
χ^2 / ndf		49.82 / 14
Gauss Norm	650.2 ± 18.38	
Gauss Mean	0 ±	0
Gauss Sigma	28.03 ± 0.5325	
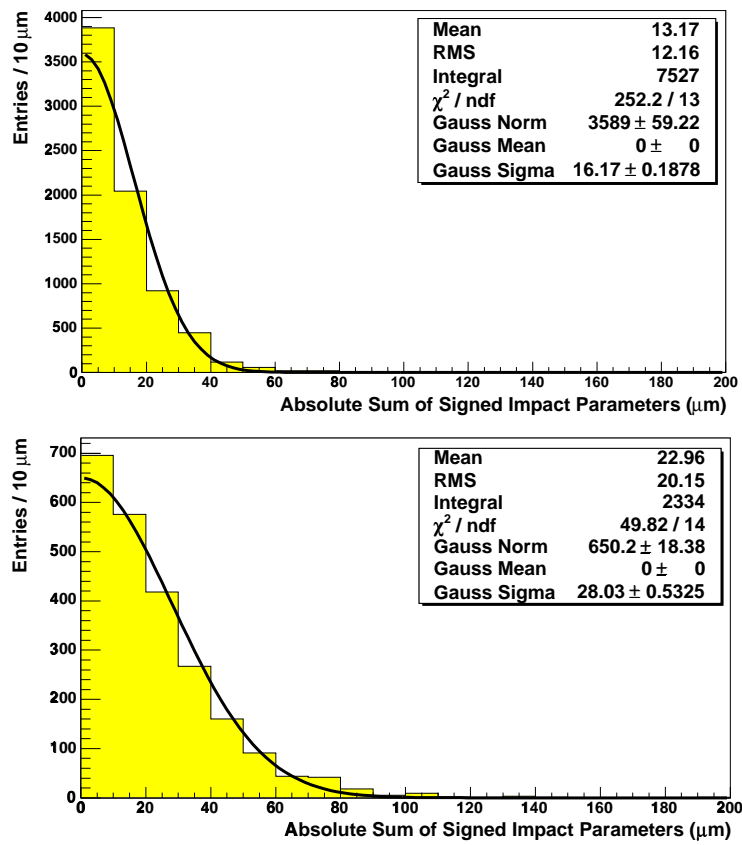
Figure 4.17: Absolute sum of signed impact parameters in $Z^0 \rightarrow \mu^+\mu^-$ events from Monte Carlo (upper plot) and data (lower plot).

Mean	65.44
RMS	68.17
Integral	680
χ^2 / ndf	22.34 / 16
Norm	211.1 ± 12.9
Exp	-0.01593 ± 0.0007572
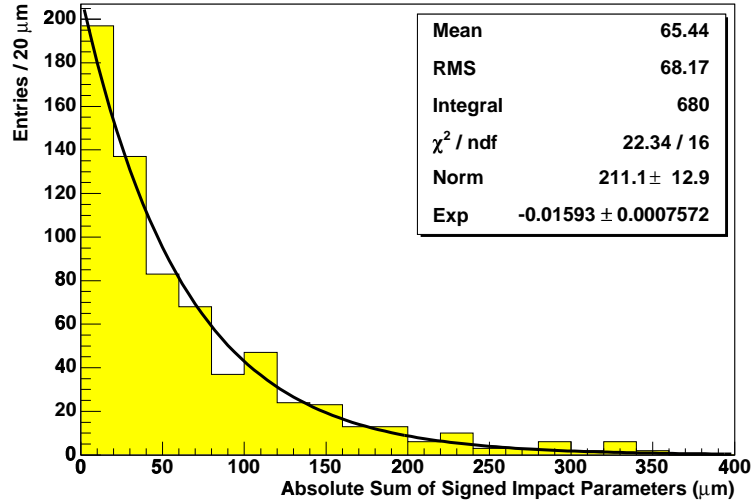
Figure 4.18: Absolute sum of signed impact parameters in $Z^0 \rightarrow \tau^+\tau^-$ Monte Carlo events with two leptonic decays.

order to confirm that this is the case, a sample of $Z^0 \rightarrow \tau^+\tau^- \rightarrow e^\pm\mu^\mp$ events is selected from data collected at DØ in Chapter 5. The decision to select this channel

is motivated by the mixed lepton flavours in the final state. This avoids background from Drell-Yan dilepton production that would be seen in events with two τs decaying to two electrons or two muons.
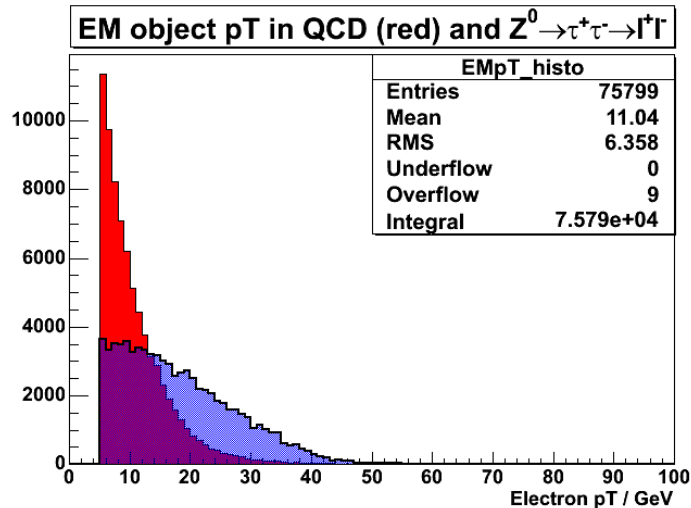
Figure 4.19: p_T of electron object in QCD (red) and $Z^0 \to \tau^+\tau^- \to l^\pm l^\mp$ (blue).

Selecting $Z^0 \to \tau^+\tau^- \to e^\pm\mu^\mp$ events at DØ presents a challenge due to the large amount of hadronic activity at the Tevatron in Run II. The leptons produced in the τ decays have a p_T distribution tending towards lower p_T, where the fake leptons produced in jets in QCD events are most likely. This is shown in Figure 4.19 where the p_T for electrons in $Z^0 \to \tau^+\tau^- \to l^\pm l^\mp$ and QCD Monte Carlo events are shown. The electrons are selected by imposing standard electron object cuts in the calorimeter (introduced in the next chapter) and requiring $p_T > 5$ GeV/c. Measurements of the dijet inclusive cross-section as a function of the invariant mass of the dijet system indicate that the total dijet inclusive cross section is very large, of order $10^5 - 10^6$ pb [35], whereas the Standard Model prediction for $\sigma(p\bar{p} \to Z^0).\text{Br}(Z^0 \to \tau^+\tau^-)$ [46] multiplied by the branching ratio to $e\mu$ is approximately 15 pb. An important priority for the event selection will therefore be high rejection for QCD background.

Chapter 5

Inspection of $Z^0 \to \tau^+\tau^- \to e^\pm\mu^\mp$ Events in Data

This chapter describes the selection of $Z^0 \to \tau^+\tau^- \to e^\pm\mu^\mp$ events in order to observe lifetime effects in the sum of impact parameters distribution. The event selection is described in Section 5.1. The estimated signal in the selection is then calculated with a technique called the 'matrix method' in Section 5.3. In order to have confidence in the signal purity, a cross section times branching ratio measurement for $Z^0 \to \tau^+\tau^- \to e^\pm\mu^\mp$ is calculated. .

5.1 $Z^0 \to \tau^+\tau^- \to e^\pm\mu^\mp$ Event Selection

The data used in this analysis represents 141.4 pb^{-1} of luminosity taken with eμ triggers between 4th October 2002 and 7th September 2003. Data has been excluded from periods when problems were observed in the central tracker, the calorimeter or the muon detectors. There are known to have been problems with the Level 1 muon triggers and the muon readout during two other periods which have also been excluded. Collected data is grouped into 'luminosity blocks' representing of order 60 seconds of $p\bar{p}$ collisions. Luminosity blocks are categorised as good or bad to indicate whether or not they can be correctly normalised to give an accurate integrated luminosity [14]. Only good luminosity blocks are used in this event selection.

The list of applied triggers changed during the period of time represented by the dataset used in this analysis. Selected events are therefore required to have fired one

of two different eμ triggers. The two triggers are

MU_A_EM10 A muon must be detected at trigger Level 1 using the muon scintillator detectors. The Level 1 muon can be anywhere within the muon detectors ($|\eta| < 2$). An EM calorimeter tower is also required to be detected at Level 1 with a transverse energy (E_T) of at least 5 GeV. At trigger Level 3, an electron must be reconstructed with $|\eta| < 3$ and $E_T > 10$ GeV. MU_A_EM10 was included in DØ trigger list 11.

MATX_EM6_SHT7 This trigger has the same requirement for Level 1 muons as MU_A_EM10. An EM calorimeter tower is required, this time with an E_T of at least 6 GeV. An electron must be reconstructed at Level 3 with $|\eta| < 3.6$ and $E_T > 7$ GeV. Requirements are also put on the shape of the energy deposits in the EM calorimeter for the Level 3 electron. MATX_EM6_SHT7 was included in DØ trigger list 12.

Both triggers ran unprescaled. $Z^0 \rightarrow \tau^+ \tau^- \rightarrow e^\pm \mu^\mp$ events are expected to feature well-reconstructed electron and muon objects that are roughly back-to-back. As shown in Chapter 4, the expected p_T distribution for both leptons is expected to overlap with the p_T distribution for fake leptons produced in QCD events, which have a large production cross-section. Selected events are therefore required to have a fully reconstructed electron and a fully reconstructed muon with cuts designed for good quality and high background rejection.

5.1.1 Electron Cuts

The first electron selection cuts described are the standard cuts used in most electron-based analyses at DØ [36]. They are designed to match calorimeter signatures to the expected behaviour of the electron. The fraction of the total E_T deposited in the calorimeter found in the EM calorimeter (the 'EM fraction') must be greater than 90%. Eight parameters are used in an 'H-matrix' to compare observed EM calorimeter shower characteristics with the expected values. The first four out of these eight parameters are the fraction of the total EM energy deposited in each of the four layers of the EM calorimeter. The remaining four parameters are the total EM energy deposited, the z-position of the primary vertex, the transverse width of the

shower in ϕ and the transverse width of the shower in z. The H-matrix comparison produces a χ^2 value that is required to be less than 20.

'EM isolation' provides a measure of how collimated an electron object is. EM isolation is defined to be the amount of E_T from EM calorimeter cells between $0.2 < \delta R < 0.4$ from the cluster centroid divided by the amount of E_T from EM calorimeter cells in the central cone $\delta R < 0.2$. In this selection, EM isolation is required to be less than 0.15. The final standard cut described here is the requirement that the electron is in the fiducial region of the calorimeter. This requirement keeps electrons away from the edges of the calorimeter in η and the ϕ-cracks between calorimeter towers to reduce detection inefficiencies.
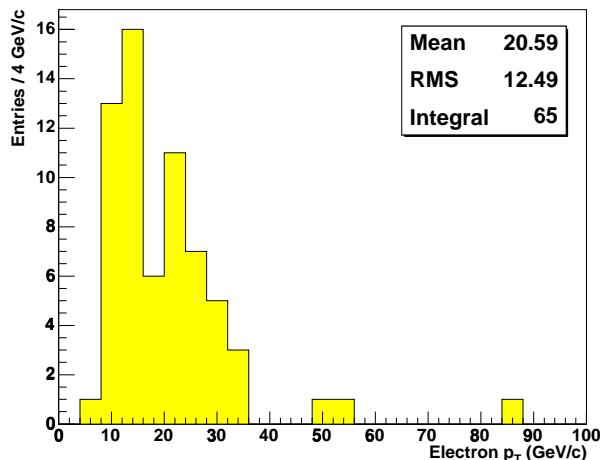
Figure 5.1: Electron candidate p_T in the final $Z^0 \to \tau^+\tau^- \to e^\pm\mu^\mp$ selection with all cuts applied except electron $p_T > 10$ GeV/c.

The electrons in this analysis are restricted to the central region of the calorimeter by requiring $|\eta| < 1.1$. As QCD events are more prominent in the forward region, this cut is expected to reduce the background. Similarly, the electron is required to have $p_T > 10$ GeV/c to get rid of background at low p_T and to satisfy the trigger requirement. Figure 5.1 shows the electron p_T distribution in the final $Z^0 \to \tau^+\tau^- \to e^\pm\mu^\mp$ selection before applying the electron p_T cut but with all other cuts applied. The very low p_T bins are suppressed by the trigger p_T requirement.

The selected electron must match Level 1 calorimeter tower and Level 3 electron objects corresponding to the eμ trigger fired. The trigger objects are matched with $\delta\phi < 0.4$ at Level 1 and $\delta R < 0.4$ at Level 3.

The electron is required to be matched to a track by cutting on a χ^2 probability where the χ^2 is defined as

$$\chi^2_{\mathrm{tm}} = \left(\frac{\delta z}{\sigma_z}\right)^2 + \left(\frac{\delta\phi}{\sigma_\phi}\right)^2 + \left(\frac{\frac{E_T}{p_T} - 1}{\sigma_{\frac{E_T}{p_T}}}\right)^2 \tag{5.1}$$

where δz and $\delta\phi$ are the differences between the EM cluster centroid position and the track position, $\frac{E_T}{p_T}$ is the transverse energy of the calorimeter cluster divided by the transverse momentum of the track and the σ values are the experimentally measured uncertainties of the relevant parameters [37]. Hadrons in QCD jets can cause fake electrons when the track from a charged hadron is reconstructed close to a calorimeter deposit from photons produced by neutral hadron decay. The incidence of such fakes is reduced by the $\frac{E_T}{p_T}$ component. The cut made is $p(\chi^2_{\mathrm{tm}}) > 0.01$. The matched track is also required to have at least two hits in the SMT and at least seven hits in the CFT to ensure that the track is well-measured.

5.1.2   Muon Cuts
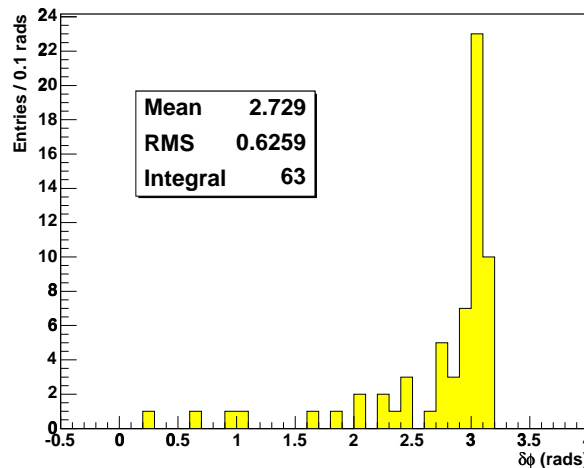
Figure 5.2: ϕ separation between the electron and the muon in the final $Z^0 \to \tau^+\tau^- \to e^\pm\mu^\mp$ selection with all cuts applied except $\delta\phi > 2$.

Muons in the final selection are also required to be of medium quality and to be within the full acceptance of the muon detectors. The muon in $Z^0 \to \tau^+\tau^- \to e^\pm\mu^\mp$ is roughly back-to-back with the electron due to the kinematics of Z^0 and τ decays. A cut of $\delta\phi > 2$ between the selected electron and muon is therefore also imposed.

The distribution of $\delta\phi$ in the final $Z^0 \to \tau^+\tau^- \to e^\pm\mu^\mp$ selection with all other cuts applied can be seen in Figure 5.2.
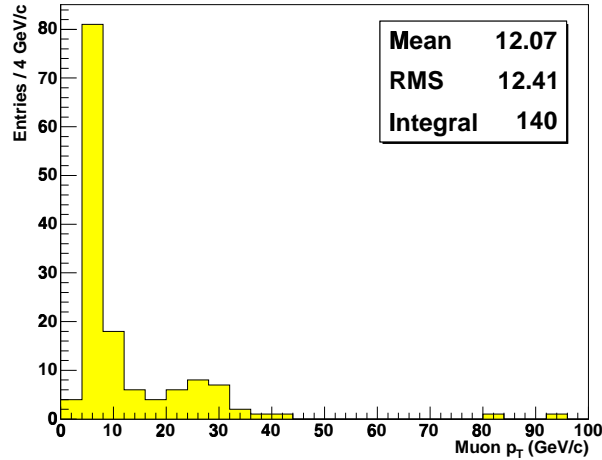
Figure 5.3: Muon candidate p_T in the final $Z^0 \to \tau^+\tau^- \to e^\pm\mu^\mp$ selection with all cuts applied except muon $p_T > 8$ GeV/c.

The muon in the $Z^0 \to \tau^+\tau^- \to e^\pm\mu^\mp$ selection is required to be matched to a central track. The central track must have at least two hits in the SMT and at least seven hits in the CFT. The p_T of the matched central track is then required to be at least 8 GeV/c. This is lower than the p_T requirement for the electron as the muon trigger requirement does not have a p_T cut and it is desirable to maximise statistics in the final sample. The p_T of the matched track is used as the central tracker measures p_T more accurately than the muon detectors. The muon p_T distribution in the final $Z^0 \to \tau^+\tau^- \to e^\pm\mu^\mp$ selection with all cuts except muon p_T is shown in Figure 5.3. The data are selected from a preselection sample with the cut muon $p_T > 5$ GeV/c so the lower bins are suppressed. The muon p_T as measured in the preselection is calculated from a combination of the matched track p_T and the p_T measured by the muon detectors. This explains why the lower bin is not completely empty. There is a distinct peak at low p_T from QCD background.

The muon must be matched to a Level 1 muon object by requiring it to be in the same or an adjacent trigger region of the muon detector in η. The electron and muon are required to be oppositely charged.

The isolation of muons in the tracker and calorimeter was introduced in Chapter 4. The standard isolation cuts used in other muon-based analyses at DØ are $\Sigma p_T^{track}(0.5) <$

3.5 GeV/c in the central tracker and $\Sigma E_T^{cal}(0.1, 0.4) < 2.5$ GeV in the EM calorimeter. Isolation provides good rejection of fake muons from hadrons 'punching through' the calorimeter and also of genuine muons in jets while retaining a high efficiency for signal muons. The next section describes work done to improve the rejection of QCD background by studying various isolation cuts.

5.2   Tuning the Muon Isolation Cut

To study the behaviour of isolation in signal muons, data samples of $Z^0 \to \mu^+ \mu^-$ and J/$\psi \to \mu^+ \mu^-$ events are selected. To make a comparison with the behaviour of muons in jets, a data sample of QCD events is also selected

5.2.1   Data Sample Selection

The $Z^0 \to \mu^+ \mu^-$ sample is selected by requiring two fully reconstructed muons of medium quality and in the full acceptance of the muon detector. Both muons must be matched to a track with at least two SMT hits and at least seven CFT hits. In order to reject events caused by cosmic ray muons crossing the detector, the difference in the measured time at the muon detector A layer must be smaller than 9 ns between the two muons. The muons must be oppositely charged and have a ϕ separation greater than $\frac{\pi}{2}$ rads.

It is then necessary to adopt a 'tag and test' approach, in which a 'tag' muon is isolated to reject background and improve sample purity while the other muon has no applied isolation cut. This muon is the 'test' muon and can be used to calculate isolation efficiencies. Both muons in an event can be tag muons.

The tag muon is given the standard DØ isolation cuts of $\Sigma p_T^{track}(0.5) < 3.5$ GeV/c and $\Sigma E_T^{cal}(0.1, 0.4) < 2.5$ GeV. The invariant masses for tagged dimuons are plotted and the number of tagged dimuons in the Z^0 peak, n_{tag}, is found by taking the integral in the range 72–108 GeV/c^2. The background from processes other than $Z^0 \to \mu^+ \mu^-$ in this range is negligible. The efficiency of an isolation cut can be found by applying the cut to the test muon, plotting a histogram of the invariant mass for surviving dimuons and finding the number of dimuons in the Z^0 peak in the same way as before. This
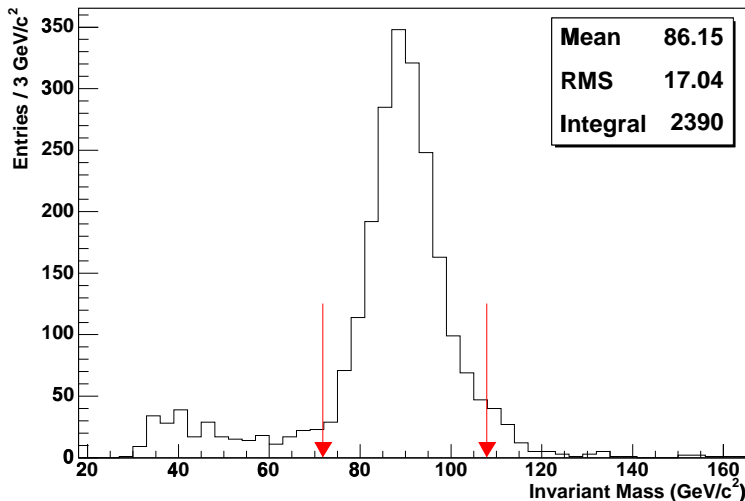
Figure 5.4: The dimuon invariant mass distribution for tagged $Z^0 \rightarrow \mu^+\mu^-$ events in which the cut $\Sigma E_T^{cal}(0.1, 0.4) < 1.5$ GeV has been applied to the test muon. The mass window for events contributing to the isolation efficiency is indicated by two red arrows at 72 GeV/c^2 and 108 GeV/c^2

number corresponds to the number of tagged dimuon systems in which the test muon passed the isolation cut, n_{pass}. The isolation efficiency, ϵ_{iso}, is then given by

$$\epsilon_{iso} = n_{pass}/n_{tag} \tag{5.2}$$

An example of the Z^0 peak for tagged dimuons passing an isolation cut of $\Sigma E_T^{cal}(0.1, 0.4) < 1.5$ GeV on the test muon is shown in Figure 5.4. The mass window used is indicated by the two arrows. Four different isolation quantities were tested and these are described after the $J/\psi \rightarrow \mu^+\mu^-$ and QCD event selections are introduced.

To select $J/\psi \rightarrow \mu^+\mu^-$ events, two muons are selected with $p_T < 15$ GeV/c. The two muons must be matched to a central track with at least two SMT hits and at least seven CFT hits. The muons must also be of medium quality and fall within the full acceptance of the muon detectors. The muons are required to have opposite charge and must also be separated in R by at least 0.5 so as not to interfere with the isolation measurement of the other muon in the event.

Once again, the standard isolation cuts are used to tag one of the muons in the event. The invariant mass of the tagged dimuon system is again plotted, although this time the sample is split into 1 GeV/c bins of p_T for the test muon. A Gaussian plus a parabola is fitted to the J/ψ mass peak in the region 2.5–4 GeV/c^2 for each tagged

100
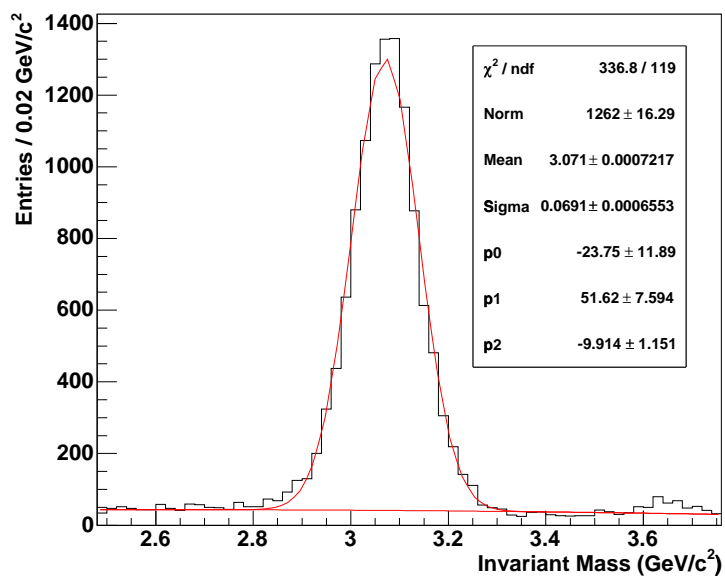
Figure 5.5: The dimuon invariant mass distribution for tagged $J/\psi \to \mu^+\mu^-$ events in which the test muon has $3 \leq p_T < 4$ GeV/c and passes the cut $\Sigma E_T^{cal}(0.1, 0.4) < 1.5$ GeV.

invariant mass distribution. The parabola models the background so the area under the J/ψ mass peak is found by integrating over just the Gaussian in the fit region. This gives the number of tagged dimuons from J/ψ events. As before, the efficiency of an isolation cut is found by applying the cut to the test muon, plotting the dimuon invariant mass for the remaining sample and fitting to the resulting J/ψ mass peak to return the number of test muons passing the cut. The ratio of passed and tagged dimuons gives the efficiency value. Figure 5.5 shows the plotted invariant mass for tagged dimuons from J/ψ events in which the test muon has a p_T between 3 and 4 GeV/c and passes the cut $\Sigma E_T^{cal}(0.1, 0.4) < 1.5$ GeV.

To select a sample of QCD events, just one muon is required in the event selection. The muon must be medium quality and in the full acceptance of the muon detectors. There must be a central track matched to the muon with $p_T > 8$ GeV/c, at least two SMT hits and at least seven CFT hits. To specify QCD events, the muon is required to have $\delta\phi > 2$ with a jet object in the calorimeter. The jet object must pass the following standard DØ calorimeter cuts to be included in the event.

- The fraction of total calorimeter E_T deposited in the EM layers must be between 5% and 95%.

101

- The fraction of total calorimeter E_T deposited in the coarse-hadronic layers must be less than 40%.

- The ratio of energy in the most energetic cell to the next most energetic cell must be less than 10.

- The number of calorimeter towers with 90% of the total calorimeter E_T must be greater than 1

The jet is also required to have $E_T > 10$ GeV. In order to exclude $W \rightarrow \mu\nu$ events, the event missing E_T must be less than 10 GeV. In order to veto on $Z^0 \rightarrow \mu^+\mu^-$ events, the event is excluded if another muon with medium quality is found within the full acceptance of the muon detectors. The event selection cuts for this sample are designed to select QCD events with kinematics similar to the signal $Z^0 \rightarrow \tau^+\tau^- \rightarrow e^\pm\mu^\mp$. This should provide insight into the QCD background for this process. The QCD sample is separated into bins of test muon p_T with a width of 4 GeV/c and the isolation efficiencies are found by applying the isolation cut to the muon and measuring the fraction that pass.

5.2.2   Inspection of Isolation Quantities

Four separate muon isolation variables were tested in the $Z^0 \rightarrow \mu^+\mu^-$ and J/$\psi \rightarrow \mu^+\mu^-$ samples. The two standard isolation variables, $\Sigma E_T^{cal}(0.1, 0.4)$ and $\Sigma p_T^{track}(0.5)$, were tested as well as $\Sigma E_T^{cal}(0.1)$, the sum of E_Ts for all calorimeter cells within $\delta R < 0.1$ of the test muon, and $\Sigma E_T^{cal}(0.4)$, the sum of E_Ts for all calorimeter cells within $\delta R < 0.4$ of the test muon. For each cut variable, isolation efficiencies were evaluated for a range of cut limits between 0 GeV and 5 GeV in 0.1 GeV steps. Muons are rejected if the cut variable is higher than the cut limit. The isolation efficiencies are shown in Figure 5.6 where the red points are efficiencies from the J/$\psi \rightarrow \mu^+\mu^-$ sample, evaluated for test muon p_T between 3 and 4 GeV/c, and the blue points are efficiencies from the $Z^0 \rightarrow \mu^+\mu^-$ sample. Only statistical errors are shown.

The plots for $\Sigma E_T^{cal}(0.1)$ and $\Sigma E_T^{cal}(0.4)$ show definite disparity between the two data samples with the J/ψ efficiencies being distinctly higher. Even though muons are minimum ionising particles, they can still leave deposits as they pass through the calorimeter. $\Sigma E_T^{cal}(0.1)$ is the transverse energy in the calorimeter within a tight cone
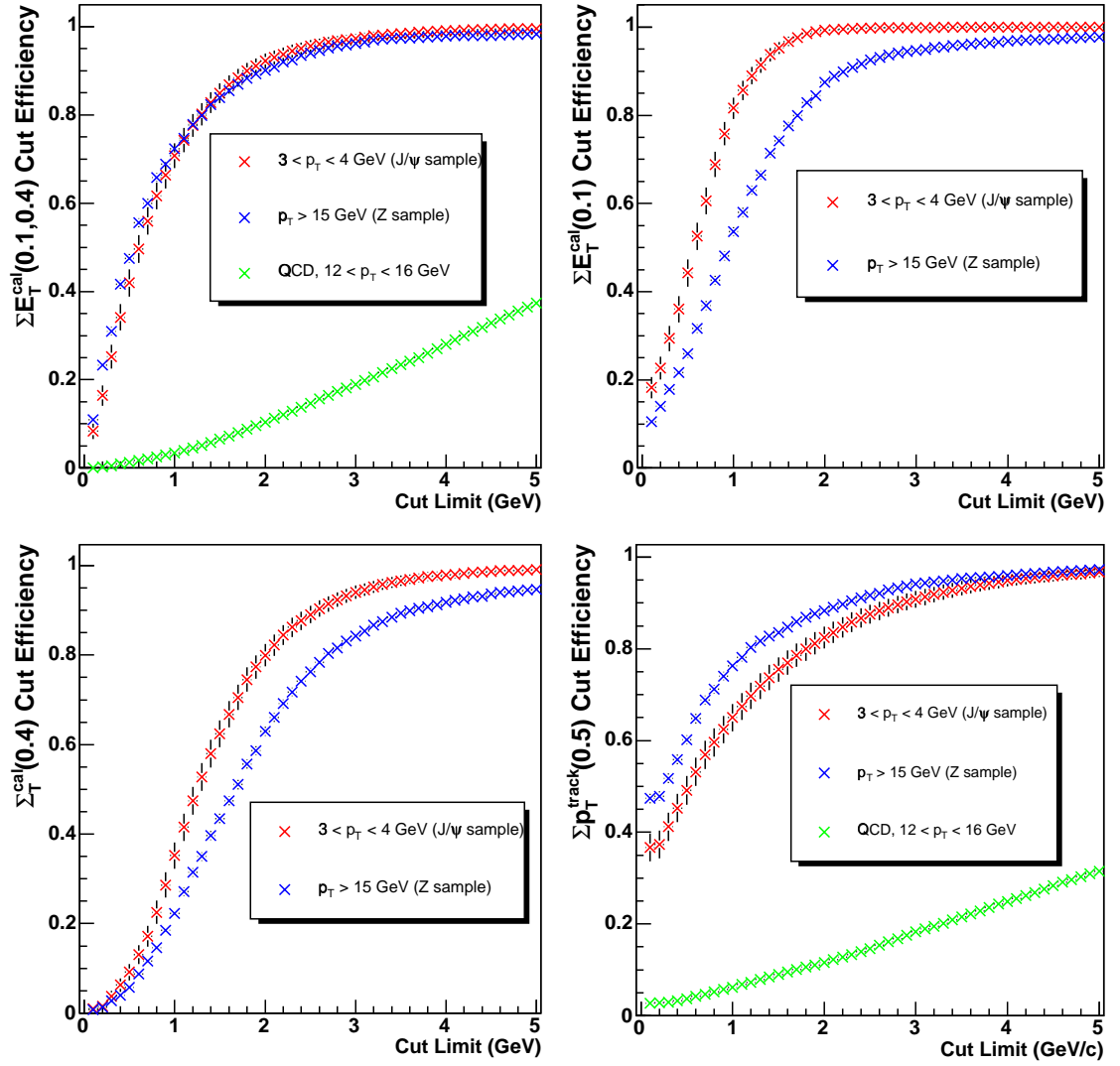
Figure 5.6: Muon isolation efficiency against cut limit for four different cut variables. Variables used are $\Sigma E_T^{cal}(0.1, 0.4)$ (top left), $\Sigma E_T^{cal}(0.1)$ (top right), $\Sigma E_T^{cal}(0.4)$ (bottom left) and $\Sigma p_T^{track}(0.5)$ (bottom right).

around the muon and so the difference in efficiencies is probably caused by the higher-p_T muons from Z^0 decays leaving more energy in the calorimeter than their lower-p_T counterparts from J/ψ decays. Similarly, $\Sigma E_T^{cal}(0.4)$ incorporates these deposits while $\Sigma E_T^{cal}(0.1, 0.4)$ avoids this effect by cutting out the $\delta R < 0.1$ region completely. It is desirable to use isolation cuts in the $Z^0 \to \tau^+\tau^- \to e^\pm\mu^\mp$ selection that function well independently of p_T. Figure 5.6 therefore confirms that $\Sigma E_T^{cal}(0.1, 0.4)$ and $\Sigma p_T^{track}(0.5)$ are good choices. While they do show some disparity between the two dimuon data samples, this is not as pronounced as for $\Sigma E_T^{cal}(0.1)$ and $\Sigma E_T^{cal}(0.4)$.

Having decided to use $\Sigma E_T^{cal}(0.1, 0.4)$ and $\Sigma p_T^{track}(0.5)$ for isolating the muons in the $Z^0 \to \tau^+\tau^- \to e^\pm\mu^\mp$ event selection, it is also interesting to see these distributions compared with the isolation efficiencies from QCD events. These are plotted in green in Figure 5.6 and represent efficiencies from the test muon p_T bin 12–16 GeV/c. The muon isolation efficiencies in QCD behave in a roughly linear fashion and it is clear that cuts at smaller values of $\Sigma E_T^{cal}(0.1, 0.4)$ and $\Sigma p_T^{track}(0.5)$ than employed as standard will increase the QCD background rejection. It is also important to keep the isolation efficiency high for signal muons. Reducing the cut limits to $\Sigma E_T^{cal}(0.1, 0.4) <$ 1.5 GeV and $\Sigma p_T^{track}(0.5) < 1.5$ GeV/c is a good compromise for signal efficiency versus background rejection on the basis of Figure 5.6.

The effect of these cuts in the $Z^0 \to \tau^+\tau^- \to e^\pm\mu^\mp$ data sample is shown in Figure 5.7. The top plots show the distribution of each isolation variable in the $Z^0 \to \tau^+\tau^- \to e^\pm\mu^\mp$ selection with all cuts applied except for both isolation cuts. The bottom plots show the distribution of each isolation variable in the selection with all other cuts applied, including the other isolation cut. The cuts can be seen to be reasonably correlated although using both cuts eliminates more background than just using one.

In order to gauge the purity of the selected $Z^0 \to \tau^+\tau^- \to e^\pm\mu^\mp$ sample, electron p_T and muon p_T are compared with expected distributions from $Z^0 \to \tau^+\tau^- \to e^\pm\mu^\mp$ Monte Carlo in Figure 5.8. The expected distributions have been found using the DØ fast Monte Carlo simulator PMCS and are normalised to the number of entries in the $Z^0 \to \tau^+\tau^- \to e^\pm\mu^\mp$ data sample. PMCS smears the generator-level information instead of performing the full detector simulation. The cuts applied are described in Section 6.1 and do not include lepton selection or trigger cuts. For now, these are assumed to be independent of p_T and therefore do not affect the shape of the p_T
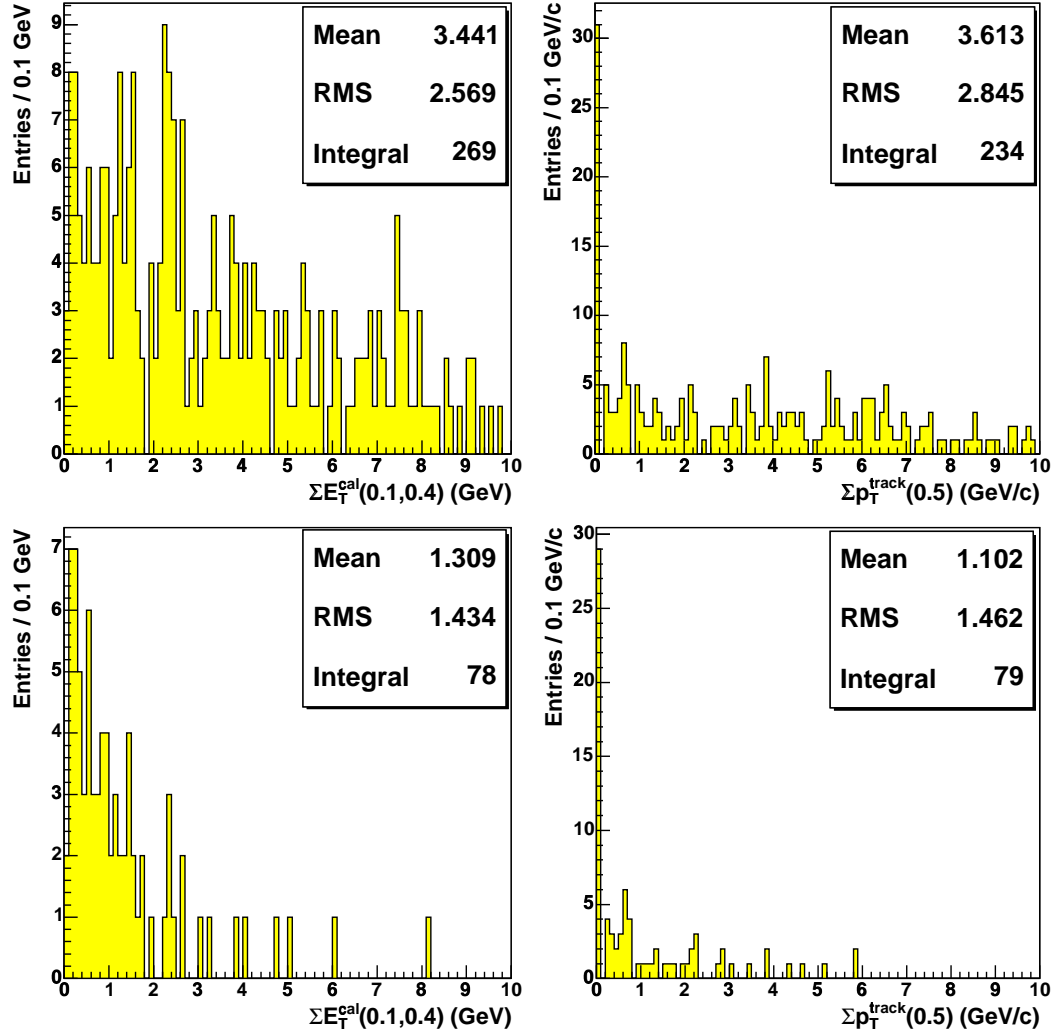
Figure 5.7: Muon isolation distributions in the final $Z^0 \to \tau^+\tau^- \to e^\pm\mu^\mp$ event selection. Distributions shown are $\Sigma E_T^{cal}(0.1, 0.4)$ with all other non-isolation cuts (top left), $\Sigma E_T^{cal}(0.1, 0.4)$ with all other cuts (bottom left), $\Sigma p_T^{track}(0.5)$ with all other non-isolation cuts (top right) and $\Sigma p_T^{track}(0.5)$ with all other cuts (top left).
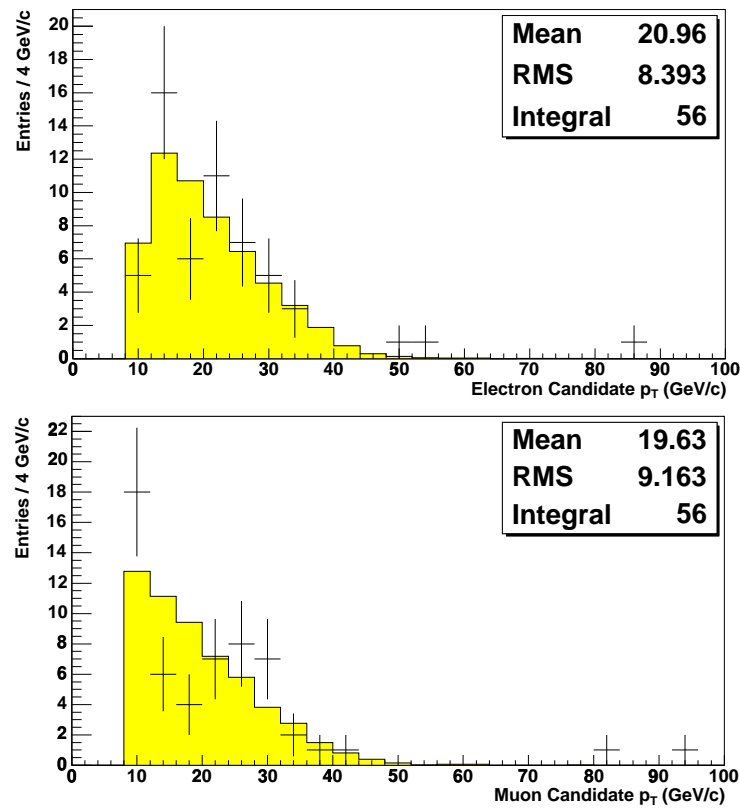
Figure 5.8: Electron candidate p_T (top) and muon candidate p_T (bottom) distributions from the $Z^0 \rightarrow \tau^+\tau^- \rightarrow e^\pm\mu^\mp$ selection (points with error bars) compared with expected p_T distributions from PMCS Monte Carlo $Z^0 \rightarrow \tau^+\tau^- \rightarrow e^\pm\mu^\mp$.

distribution. This assumption is tested later on.

The electron p_T shows reasonable agreement between data and the expected behaviour but the muon p_T distribution seems to indicate contamination from background at low p_T. It is difficult to have confidence in the sample purity based on this observation.

5.3   Signal Estimation with the Matrix Method

The 'matrix method' is a technique for calculating the amount of signal in a mixed sample of signal and background. The number of events in the sample is given by

$$N = n_{sig} + n_{bkg} \tag{5.3}$$

where n_{sig} is the number of signal events and n_{bkg} is the amount of background. If a cut is now applied to the sample then the new number is given by

$$N' = \epsilon_{sig}n_{sig} + \epsilon_{bkg}n_{bkg} \tag{5.4}$$

106

where ϵ_{bkg} and ϵ_{sig} are the cut efficiencies for the background and signal respectively. Equations 5.3 and 5.4 can be rearranged to give

$$n_{sig} = \frac{N' - \epsilon_{bkg}N}{\epsilon_{sig} - \epsilon_{bkg}} \qquad (5.5)$$

The amount of signal can therefore be calculated if the signal and background cut efficiencies are known.

In the $Z^0 \to \tau^+\tau^- \to e^\pm\mu^\mp$ selection, there is assumed to be a contribution from QCD background. The muon isolation efficiency for both signal and QCD background was calculated in Section 5.2 so it may be possible to calculate the amount of genuine $Z^0 \to \tau^+\tau^- \to e^\pm\mu^\mp$ using the matrix method. It is important to understand how the muon isolation efficiencies behave with muon p_T. The efficiencies from J/ψ events were calculated in bins of the test muon p_T but the efficiencies from the $Z^0 \to \mu^+\mu^-$ sample were calculated for any test muon p_T above 15 GeV/c. To remedy this, the same tagged dimuons from Z^0 events are used but the sample is broken down into bins of test muon p_T and the isolation efficiency for each bin is calculated.
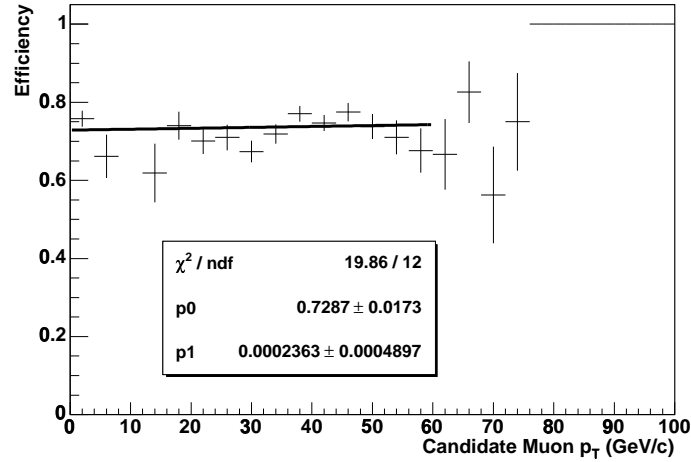
Figure 5.9: Isolation efficiency for signal muons vs. p_T. The two points at low p_T come from J/$\psi \to \mu^+\mu^-$ events while the other points come from $Z^0 \to \mu^+\mu^-$

Figure 5.9 shows the signal muon isolation efficiency against p_T. Efficiencies from the J/$\psi \to \mu^+\mu^-$ selection are shown in the first two points at low p_T while the rest of the efficiencies come from $Z^0 \to \mu^+\mu^-$. A straight line has been fitted in the range 0–60 GeV/c and the paremeters are shown. The efficiencies look flat with p_T and a p_T independent fit to the efficiencies yields an overall efficiency of 0.736 ± 0.008.

There will also be a systematic error arising from the requirement that the tag muon is isolated in each event. Other studies to measure the standard muon isolation efficiency have found this effect to give of order a 1% error [38]. The isolation cut used here is tighter and so the effect may be more pronounced. A systematic error of 2% is applied to give the overall efficiency 0.736 ± 0.017.
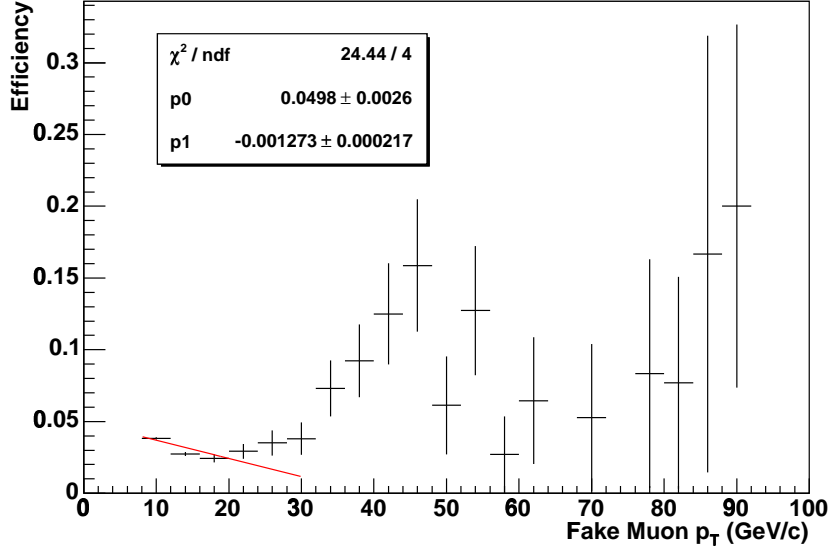
Figure 5.10: Isolation efficiency for muons in QCD events vs. p_T.

The muon isolation efficiencies found in the QCD sample as a function of p_T are shown in Figure 5.10. The distribution falls slightly at low p_T and then rises again from around 20–30 GeV/c. These characteristics are consistent with other studies [39] that have shown the rising isolation efficiency at high p_T to be due to $W \rightarrow \mu\nu$ contamination. This makes it difficult to interpret the behaviour with p_T of the low p_T isolation efficiency. The line drawn in Figure 5.10 is a linear fit in the range 8–30 GeV/c and clearly has a negative gradient. However, it is unclear whether the efficiency would continue to drop as p_T increases if there was no contamination from $W \rightarrow \mu\nu$ events. A constant fit in the same range gives the p_T independent efficiency 0.0349 ± 0.0007. For the time being, a value of 0.035 ± 0.02 will be used to be conservative. The quoted error incorporates all points in the fit range.

Figure 5.11: Muon p_T in the $Z^0 \to \tau^+\tau^- \to e^\pm\mu^\mp$ sample (histograms, black points) before (top plot) and after (middle plot) applying muon isolation cuts. Matrix method estimated background in the $Z^0 \to \tau^+\tau^- \to e^\pm\mu^\mp$ sample after applying muon isolation cuts is shown in the middle plot (blue points with errors). Bottom plot shows matrix method estimation of signal muon p_T distribution (blue points with errors) compared with expected muon p_T distribution from PMCS Monte Carlo (histogram).

QCD Muon Isolation Efficiency	Number of Events
Fitted Slope	64.12 ± 10.61
Fitted Flat	64.43 ± 10.73
0.035 ± 0.02	64.41 ± 12.17

Table 5.1: Estimated number of $Z^0 \to \tau^+\tau^- \to e^\pm\mu^\mp$ events using the matrix method and applying different parameterisations for the QCD muon isolation efficiency.

5.3.1 The Matrix Method in Data

The top two plots in Figure 5.11 show the muon p_T distribution in the selected $Z^0 \to \tau^+\tau^- \to e^\pm\mu^\mp$ sample before and after applying the muon isolation cuts, with all other cuts applied. The p_T distribution before isolation is heavily peaked towards low p_T. The p_T distribution after isolation still has a peak at low p_T although it is not as pronounced, indicating that the isolation cuts reject most of the QCD background, but there is still a non-negligible contribution. By taking the bin contents from these two plots and applying Equation 5.5 bin-by-bin with the p_T independent muon isolation efficiencies discussed above, the p_T distribution is estimated for muons in signal $Z^0 \to \tau^+\tau^- \to e^\pm\mu^\mp$ events before the isolation cuts have been applied. This is shown in the bottom plot in Figure 5.11, compared with the expected muon p_T distribution from PMCS Monte Carlo introduced in the last section. The expected distribution has been normalised to the number of events in the estimated muon p_T distribution. The background subtracted by the matrix method from the muon p_T distribution after muon isolation is also shown in the middle plot. This is found by multiplying the number of background events calculated in the $Z^0 \to \tau^+\tau^- \to e^\pm\mu^\mp$ sample before applying the muon isolation cuts (n_bkg in Equation 5.3) by the isolation efficiency for QCD muons (ϵ_bkg in Equation 5.4). The background peaks at low p_T, suggesting the removal of QCD background. There is good agreement between the matrix method estimated p_T distribution in $Z^0 \to \tau^+\tau^- \to e^\pm\mu^\mp$ and the expected p_T distribution. This indicates that the matrix method is effective in estimating the signal muon p_T distribution and subtracting the QCD background contribution.

The matrix method estimated muon p_T distribution in Figure 5.11 assumes a QCD muon isolation efficiency of 0.035 ± 0.02. The behaviour with p_T of the QCD muon

isolation efficiency shown in Figure 5.10 is inconclusive so the matrix method procedure is repeated using the fitted p_T dependent and p_T independent distributions for QCD muon isolation efficiency. The number of signal $Z^0 \to \tau^+\tau^- \to e^\pm\mu^\mp$ events is found in all cases and these are shown in Table 5.3.1. There is very little difference between the results as the QCD background acts at low p_T, where the fit values are closer together. The use of a QCD muon isolation efficiency of 0.035 ± 0.02 is justified as the error on the number of events accommodates the number of events using the two other parameterisations.

The isolation efficiencies for muons in QCD events and signal $Z^0 \to \tau^+\tau^- \to e^\pm\mu^\mp$ events are assumed to be independent of muon p_T. The overall isolation efficiency values can therefore be used in the matrix method to provide an estimated signal distribution for any variable, providing that the muon isolation efficiencies in QCD events and signal $Z^0 \to \tau^+\tau^- \to e^\pm\mu^\mp$ events are also independent of that variable. Electron p_T distributions before and after applying the muon isolation cuts to the $Z^0 \to \tau^+\tau^- \to e^\pm\mu^\mp$ sample with all other cuts applied are shown in the top two plots in Figure 5.12. The middle plot also shows the background electron p_T distribution estimated by the matrix method in the $Z^0 \to \tau^+\tau^- \to e^\pm\mu^\mp$ sample after the muon is isolated. The background is mainly in the lower two p_T bins, again indicating the removal of QCD background from the selected $Z^0 \to \tau^+\tau^- \to e^\pm\mu^\mp$ sample. The bottom plot shows the matrix method estimated electron p_T distribution for signal $Z^0 \to \tau^+\tau^- \to e^\pm\mu^\mp$ events before muon isolation cuts are applied compared with the expected distribution from PMCS Monte Carlo with selection efficiencies measured in data. The expected electron p_T distribution has been normalised to the number of events in the matrix method estimated distribution. The two distributions show good agreement.

The absolute sum of signed impact parameters in the $Z^0 \to \tau^+\tau^- \to e^\pm\mu^\mp$ sample plotted before and after the muon isolation cuts are applied are shown in Figure 5.13 in the top and middle plots respectively. Variable binning has been employed to minimise the effect of low statistics in the bins at high values. The matrix method is applied bin-by-bin to estimate the signal distribution for the absolute sum of signed impact parameters and this is shown by the points with error bars in the bottom plot. It is assumed here that the muon isolation efficiencies in QCD events and
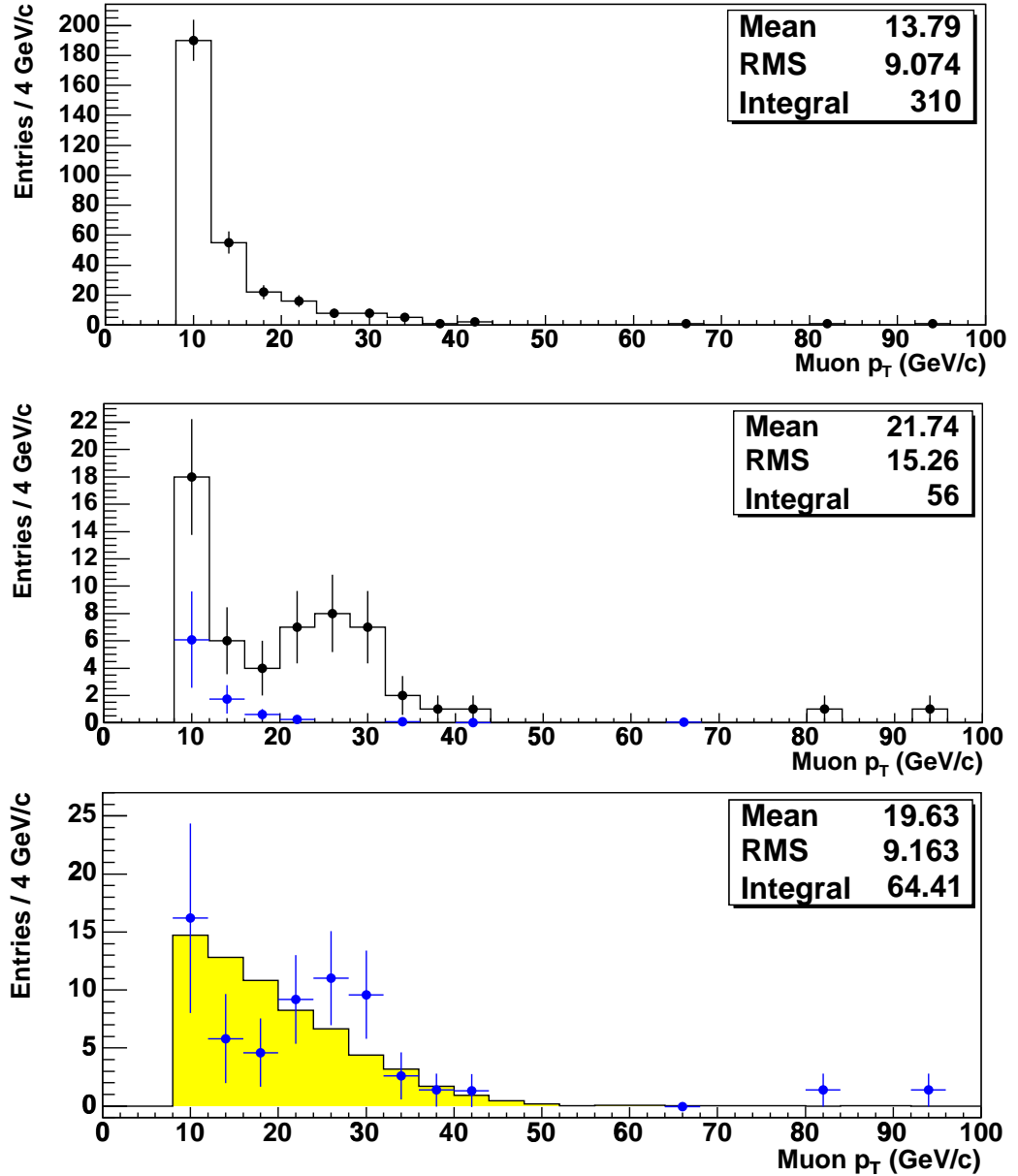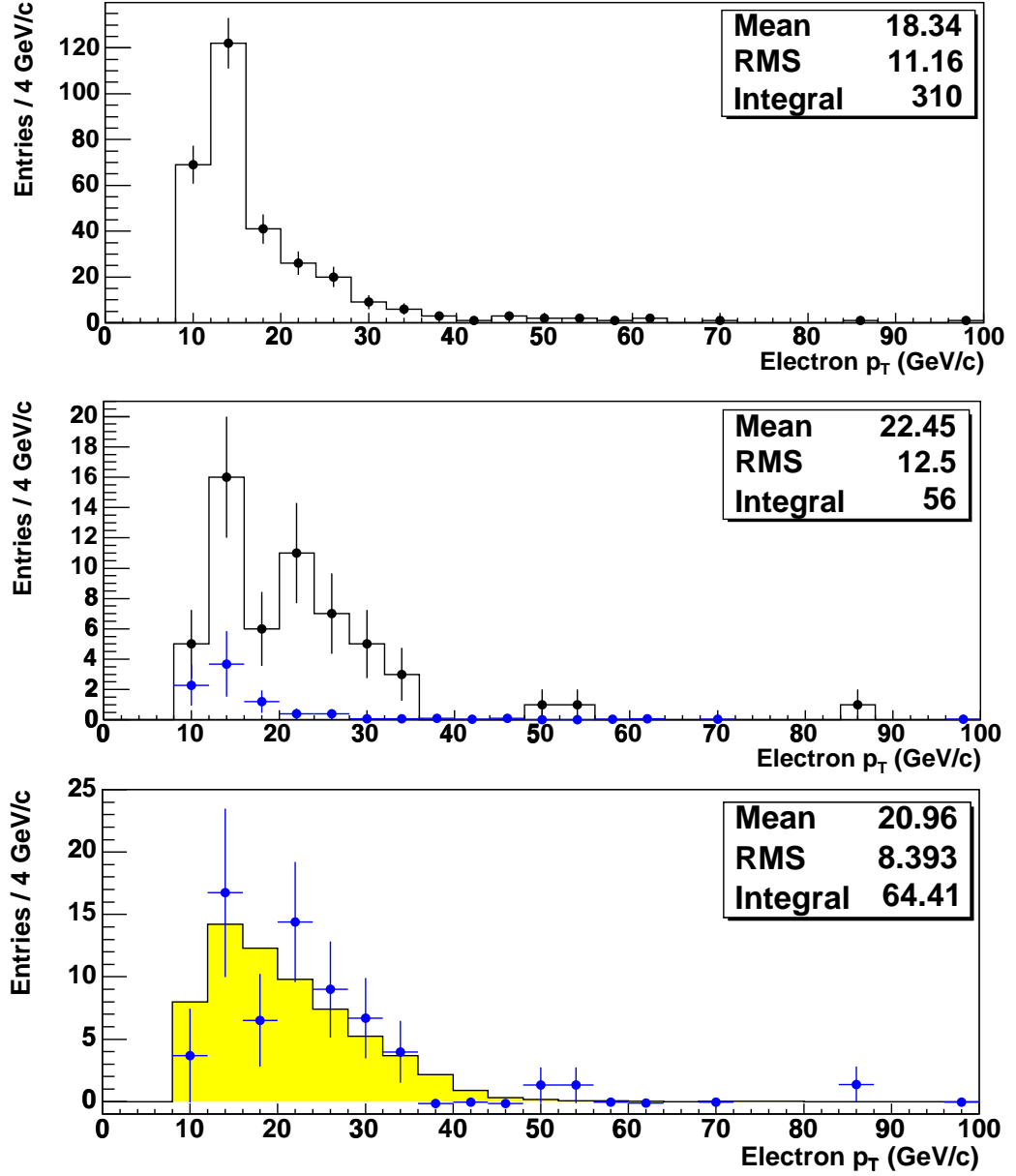
Figure 5.12: Electron p_T in the $Z^0 \to \tau^+\tau^- \to e^{\pm}\mu^{\mp}$ sample (histograms, black points) before (top plot) and after (middle plot) applying muon isolation cuts. Matrix method estimated background in the $Z^0 \to \tau^+\tau^- \to e^{\pm}\mu^{\mp}$ sample after applying muon isolation cuts is shown in the middle plot (blue points with errors). Bottom plot shows matrix method estimation of signal electron p_T distribution (blue points with errors) compared with expected electron p_T distribution from PMCS Monte Carlo (histogram).
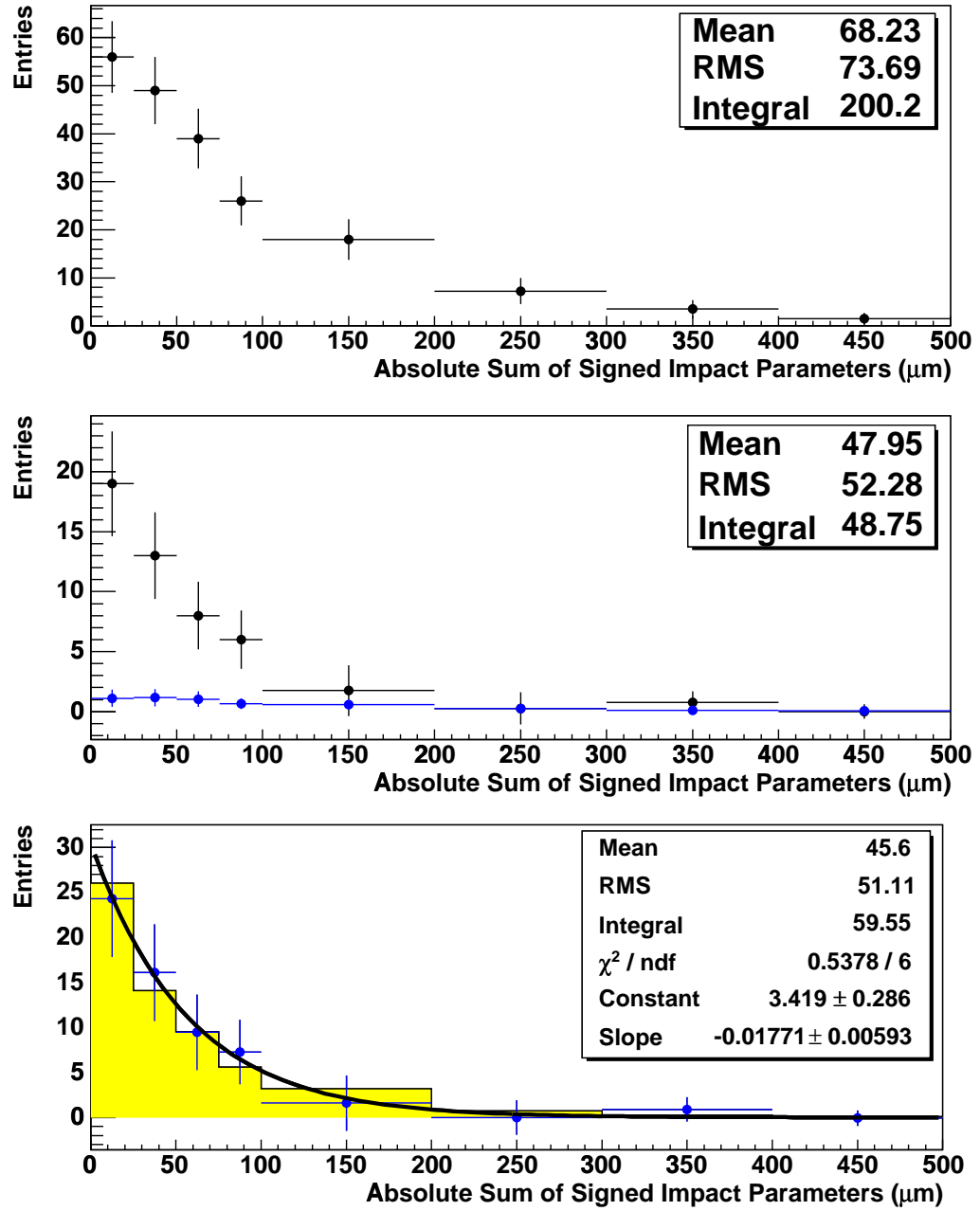
Figure 5.13: The absolute sum of signed impact parameters in the $Z^0 \to \tau^+\tau^- \to e^\pm\mu^\mp$ sample (histograms, black points) before (top plot) and after (middle plot) applying muon isolation cuts. Estimated background subtracted by the matrix method from the $Z^0 \to \tau^+\tau^- \to e^\pm\mu^\mp$ sample after applying muon isolation cuts is shown in the middle plot (blue points with errors). Bottom plot shows matrix method estimation of signal distribution (blue points with errors) compared with expected distribution from Monte Carlo $Z^0 \to \tau^+\tau^- \to l^\pm l^\mp$ with full detector simulation (histogram).

signal $Z^0 \rightarrow \tau^+\tau^- \rightarrow e^\pm\mu^\mp$ events are independent of the absolute sum of signed impact parameters. The histogram shown in the bottom plot is the distribution from $Z^0 \rightarrow \tau^+\tau^- \rightarrow l^\pm l^\mp$ events shown in Figure 4.18 plotted with variable bins. Impact parameters are not modelled by PMCS so this comparison is used. The distributions of absolute sum of signed impact parameters from Monte Carlo and data are in reasonable agreement. An exponential has been fitted to the matrix method estimated signal distribution and the parameters are shown in the bottom plot. The value of the exponent is (-0.0177 ± 0.0059) μm^{-1} , within errors of the exponent from the fit shown in Figure 4.18.

The agreement between the sum of signed impact parameters from Monte Carlo and data is much better for the $Z^0 \rightarrow \tau^+\tau^-$ samples compared here than the agreement between the $Z^0 \rightarrow \mu^+\mu^-$ samples compared in Chapter 4. This makes sense as the τ lifetime dominates the sum of signed impact parameters distribution, making any tracking resolution or beam width effects less significant.

The absolute sum of signed impact parameters distribution observed in the $Z^0 \rightarrow \tau^+\tau^- \rightarrow e^\pm\mu^\mp$ sample before muon isolation cuts are applied is noticeably wider than the matrix method estimated distribution for signal $Z^0 \rightarrow \tau^+\tau^- \rightarrow e^\pm\mu^\mp$ events. This is reflected in the quoted RMS values in each plot. The middle plot in Figure 5.13 also indicates the distribution of matrix method estimated background in the $Z^0 \rightarrow \tau^+\tau^- \rightarrow e^\pm\mu^\mp$ sample after muon isolation is applied. There is a slight peak at low values but the distribution is fairly wide. This indicates contamination from $c\bar{c}$ and $b\bar{b}$ events which also feature decays with lifetime. It is envisaged that a lifetime-based cut for τ identification purposes using the absolute sum of signed impact parameters would need to have an upper limit to exclude QCD events containing decays with lifetime as well as a lower limit to exclude decays with no lifetime.

The matrix method technique appears to have yielded a signal $Z^0 \rightarrow \tau^+\tau^- \rightarrow e^\pm\mu^\mp$ sample with reasonable purity. In order to give increased confidence in the sample purity, the estimated number of $Z^0 \rightarrow \tau^+\tau^- \rightarrow e^\pm\mu^\mp$ events is used to calculate $\sigma(p\bar{p} \rightarrow Z^0).Br(Z^0 \rightarrow \tau^+\tau^-)$ and a comparison is made with Standard Model predictions.

Chapter 6

Calculation of
$\sigma(\text{p}\bar{\text{p}} \to \text{Z}^0).\text{Br}(Z^0 \to \tau^+\tau^-)$

In a dataset with a total integrated luminosity of $\int \mathcal{L}\text{dt}$, a process with a production cross-section times branching ratio $\sigma.\text{Br}$ produces a number of events given by

$$N_{\text{prod}} = \sigma.\text{Br} \times \int \mathcal{L}\text{dt} \tag{6.1}$$

The number of observed events (N_{obs}) from this process after applying selection cuts is then given by

$$N_{\text{obs}} = N_{\text{prod}} \times A \tag{6.2}$$

where A is the acceptance for the event selection. The acceptance receives contributions from the geometrical acceptance and efficiencies arising from the event selection cuts. The geometrical acceptance is the fraction of events in which the relevant particles lie within the geometrical region defined by the cuts.

In this analysis, the acceptance will be calculated as

$$A = A_{\text{gk}} \times \epsilon(\text{e}) \times \epsilon(\mu) \tag{6.3}$$

where A_{gk} is a combined geometrical acceptance and kinematic acceptance taking into account the lepton p_{T} cuts and $\delta\phi$ cut between the electron and the muon. A_{gk} will also accommodate the branching fraction for two τs to decay to an electron and a muon. $\epsilon(\text{e})$ is the overall electron selection efficiency and $\epsilon(\mu)$ is the overall muon selection efficiency. In this analysis, the term 'selection efficiency' incorporates the efficiency for the electron or muon to satisfy trigger requirements. $\epsilon(\text{e})$ and $\epsilon(\mu)$ are

treated as uncorrelated for this calculation. The evaluation of A_{gk}, $\epsilon(e)$ and $\epsilon(\mu)$ are described in the following sections.

Combining Equations 6.1, 6.2 and 6.3 yields the expression

$$\sigma(\mathrm{p\bar{p}} \to Z^0).\mathrm{Br}(Z^0 \to \tau^+\tau^-) = \frac{N_{obs}}{\int \mathcal{L}dt \times A_{gk} \times \epsilon(e) \times \epsilon(\mu)} \tag{6.4}$$

While the motivation for calculating $\sigma(\mathrm{p\bar{p}} \to Z^0).\mathrm{Br}(Z^0 \to \tau^+\tau^-)$ is to provide an indication of the purity of the signal $Z^0 \to \tau^+\tau^- \to e^{\pm}\mu^{\mp}$ sample estimated by the matrix method, it is worth noting that this constitutes the first measurement of $\sigma(\mathrm{p\bar{p}} \to Z^0).\mathrm{Br}(Z^0 \to \tau^+\tau^-)$ in this channel at a hadronic collider detector.

6.1 Evaluation of the Geometrical and Kinematic Acceptance

A large sample of $Z^0/\gamma^* \to \tau^+\tau^-$ events generated by the PYTHIA Monte Carlo generator and smeared by PMCS is used to find A_{gk}. The invariant mass of the Z^0/γ^* propagator is found from truth information and events outside the mass window 66–116 GeV/c^2 are excluded. The effect of virtual photon exchange in this mass range is negligible [40] so all events are considered to be the non-physical process $Z^0 \to \tau^+\tau^-$. The sample contains 2,116,437 $Z^0 \to \tau^+\tau^-$ events in total after the invariant mass cut. The Z^0/γ^* propagator invariant mass is shown in Figure 6.1 with the mass window indicated.

The geometrical and kinematic cuts from the $Z^0 \to \tau^+\tau^- \to e^{\pm}\mu^{\mp}$ selection are applied to the smeared leptons in the $Z^0 \to \tau^+\tau^-$ sample. These cuts are

- Electron $p_T > 10$ GeV/c.

- Electron $|\eta| < 1.1$.

- Muon found in the full muon detector acceptance.

- Muon $p_T > 8$ GeV/c.

- $\delta\phi > 2$ between the electron and the muon

116
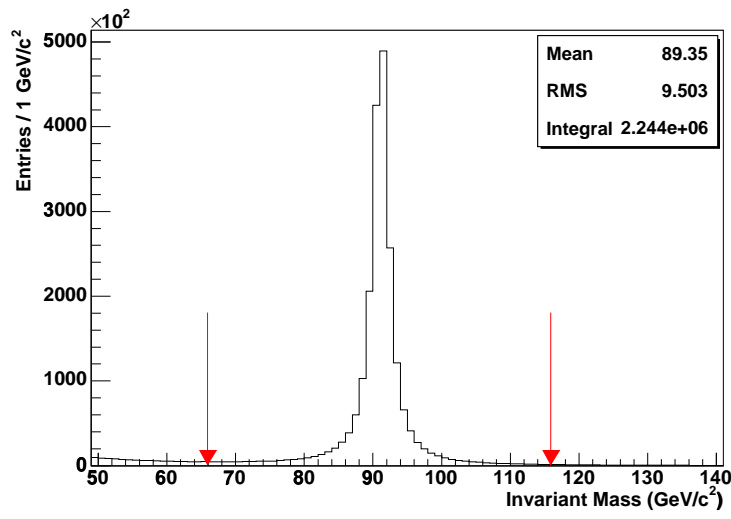
Figure 6.1: Generated invariant mass of the Z^0/γ^* in PYTHIA $Z^0/\gamma^* \to \tau^+\tau^-$ Monte Carlo.

PMCS does not simulate the faking of electron and muon signatures in the detector so the selected electron and muon must come from $Z^0 \to \tau^+\tau^- \to e^\pm\mu^\mp$. The branching fraction for two τs decaying to an electron and a muon are therefore also included here. After applying just the geometrical cuts (the η cut on the electron and the detector acceptance cut on the muon), 29,049 $Z^0 \to \tau^+\tau^- \to e^\pm\mu^\mp$ events remain in the sample. The ratio of the number of events before and after the geometrical cuts gives a geometrical acceptance of 0.01373 ± 0.00008, where the error is statistical. After then applying the kinematic cuts, 14,187 events remain in the sample. The ratio of the number of events before and after the kinematic cuts gives a kinematic acceptance of 0.488 ± 0.004, again with a statistical error. By taking the number of events before and after all geometrical and kinematic cuts are applied, A_{gk} is found to be

$$A_{gk} = 0.00670 \pm 0.00006$$

where the error is statistical.

6.2 Evaluation of the Overall Electron Selection Efficiency

The efficiency $\epsilon(e)$ is the efficiency of selecting an electron that satisfies all of the cuts in the $Z^0 \to \tau^+\tau^- \to e^\pm\mu^\mp$ event selection given that the electron has already satisfied the p_T and η requirements. $\epsilon(e)$ can be broken down further into three efficiencies.

$\epsilon_{cal}(e)$ The efficiency for an electron to produce a triggered electron object of the desired quality in the calorimeter.

$\epsilon_{track}(e)$ The efficiency for an electron to produce a track of the desired quality in the central tracker.

$\epsilon_{match}(e)$ The efficiency for the calorimeter electron to match the central track.

Two samples of $Z^0 \to e^+e^-$ events are selected from the same dataset used for the $Z^0 \to \tau^+\tau^- \to e^\pm\mu^\mp$ selection in order to measure $\epsilon_{track}(e) \times \epsilon_{match}(e)$ and $\epsilon_{cal}(e)$.

6.2.1 Measuring $\epsilon_{track}(e) \times \epsilon_{match}(e)$

$Z^0 \to e^+e^-$ events are selected by requiring a well-measured tag electron roughly back-to-back in ϕ with a test electron measured only in the calorimeter. The test electron has the same trigger and calorimeter-based quality cuts applied as the signal electron in the $Z^0 \to \tau^+\tau^- \to e^\pm\mu^\mp$ event selection and is therefore used to measure $\epsilon_{track}(e) \times \epsilon_{match}(e)$ by finding the fraction of test electrons that are matched to a track with at least two SMT hits and at least seven CFT hits. Both $\epsilon_{track}(e)$ and $\epsilon_{match}(e)$ are taken into account as this electron must have produced a well-measured track and the track must be matched to the calorimeter electron.

The tag and test electrons must both pass the following cuts

- $|\eta| < 1.1$.

- EM fraction $> 90\%$.

- EM isolation < 0.15.

- H-matrix $\chi^2 < 20$.

- In fiducial region of calorimeter.

The tag electron has $p_T > 25$ GeV/c and is matched to a track. The test electron has $p_T > 10$ GeV/c and matches the Level 1 and Level 3 trigger objects required in the appropriate eμ trigger for the current run. The tag and test electrons must have a ϕ separation of at least 2 rads. The low p_T cut on the test electron leads to QCD background in the selected sample. To deal with this, the tag electron is required to be isolated in the tracker with $\Sigma p_T^{\text{track}}(0.5) < 1.5$ GeV/c.

The efficiency of the test electron being matched to a track is shown in Figure 6.2 plotted against the p_T of the test electron. The efficiencies from data taken with DØ trigger lists 11 and 12 are shown separately as well as showing the efficiencies from the entire dataset combined. For all plots, the efficiencies in the p_T range corresponding to electrons from the Z^0 peak look independent of p_T but there is a substantial drop in efficiency towards low p_T. There are currently no suitable cross-checks for this efficiency at low p_T and it is not well-modelled in Monte Carlo. This can be seen in Figure 6.3, where the same procedure for calculating $\epsilon_{\text{track}}(e) \times \epsilon_{\text{match}}(e)$ has been applied to fully reconstructed $Z^0 \rightarrow e^+e^-$ Monte Carlo events. In this case, the electrons had no trigger requirement imposed and they were matched with $\delta R < 0.1$ to generator-level electrons.

In order to better understand the drop in efficiency at low p_T, the invariant mass of the dielectron system is compared for selected events in which the test electron passes and fails the track-match requirement. The invariant mass is calculated using calorimeter-based information from both electrons. The top plot in Figure 6.4 shows the comparison for events with the test electron in the p_T range 36–48 GeV/c^2 and the bottom plot shows the comparison for events with the test electron in the p_T range 8–20 GeV/c^2. In both plots, the two distributions are normalised to the same integral in order to compare the distribution shapes. The invariant mass distributions for the test electron passing and failing the track-match requirement with the test electron in the higher p_T range show good agreement and indicate that the two electrons come from the Z^0 peak. The invariant mass distributions for the test electron passing and failing the track-match requirement with the test electron in the lower p_T range also show reasonable agreement and indicate that the two electrons come either from the lower invariant mass Z^0/γ^* tail (Drell-Yan events) or from background contamination
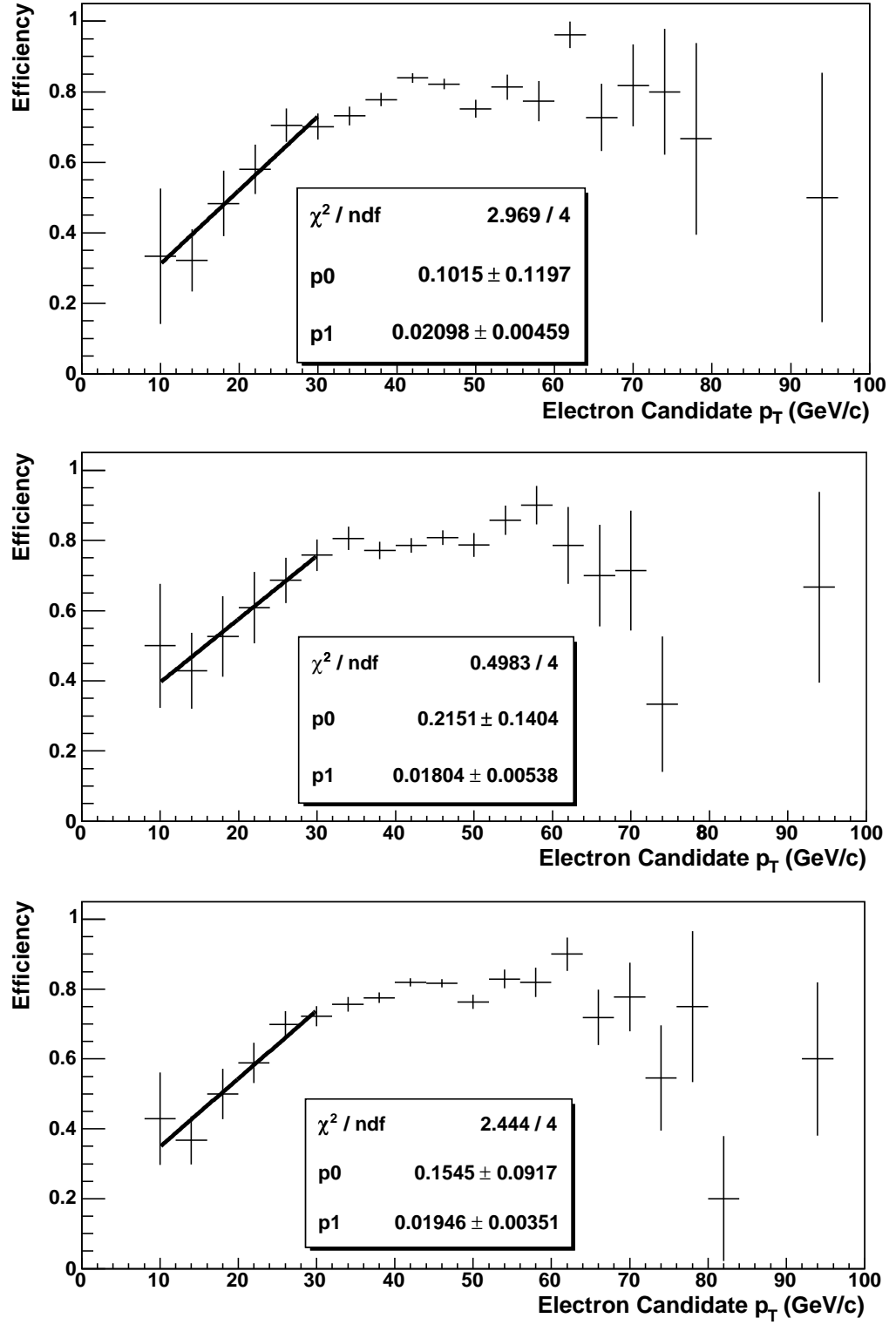
Figure 6.2: $\epsilon_{\text{track}}(e) \times \epsilon_{\text{match}}(e)$ against p_{T} for data taken with DØ trigger list 11 (top plot), trigger list 12 (middle plot) and both trigger lists (bottom plot).
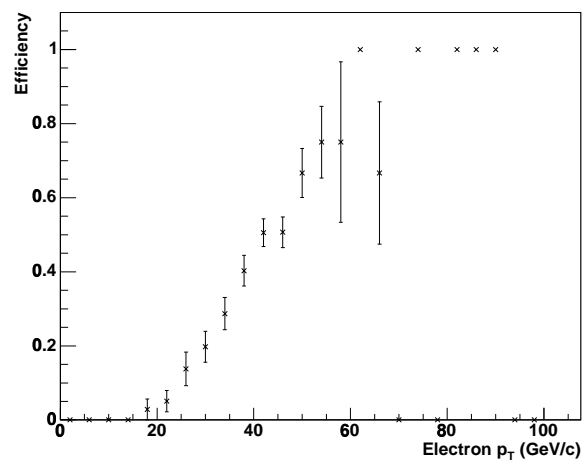
Figure 6.3: $\epsilon_{\text{track}}(e) \times \epsilon_{\text{match}}(e)$ against p_{T} in $Z^0 \to e^+ e^-$ Monte Carlo.
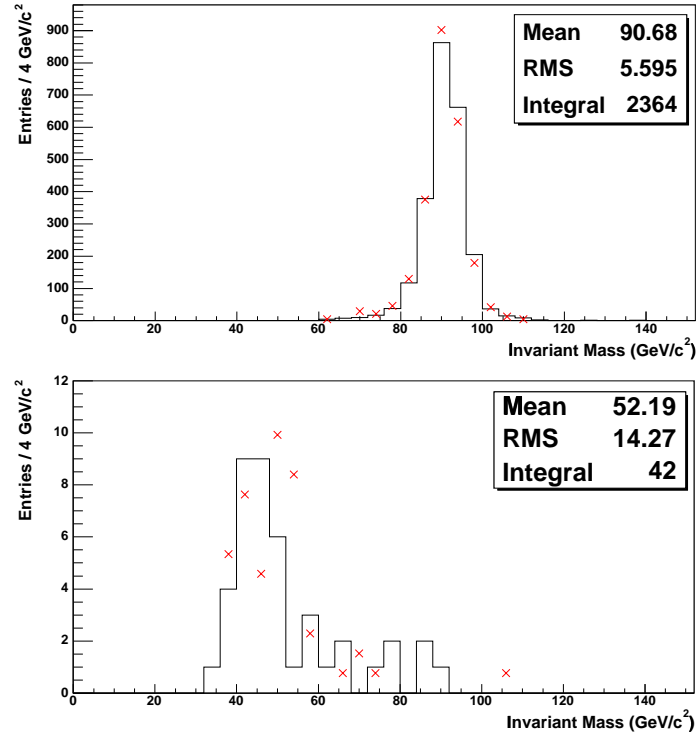
Figure 6.4: Dielectron invariant mass for selected $Z^0 \to e^+ e^-$ events in which the test electron passes (histogram) and fails (red crosses) the track-match requirement for test electron p_{T} 36–48 GeV/c^2 (top plot) and 8–20 GeV/c^2 (bottom plot).

at low p_{T}. It is therefore unclear whether the drop in efficiency at low p_{T} is a genuine effect for signal electrons.

The efficiencies in Figure 6.2 have been fitted with a p_{T} dependent linear fit in the range 10–30 GeV. The fit parameters are displayed on each plot, where 'p1' is the gra-

Trigger List Used	Fit Value
11	0.806 ± 0.007
12	0.797 ± 0.010
Both	0.798 ± 0.006

Table 6.1: $\epsilon_{\text{track}}(\text{e}) \times \epsilon_{\text{match}}(\text{e})$ values found with p_{T} independent fits to the efficiencies shown in Figure 6.2 in the p_{T} range 30–70 GeV

dient and 'p0' is the intercept. A p_{T} independent fit to the efficiencies in the p_{T} range 30–70 GeV gives the values shown in Table 6.1. For the p_{T} dependent and p_{T} independent fits, the fit parameters from the separate trigger list plots and the combined plot agree within errors. It is therefore reasonable to use the efficiencies taken over the entire dataset in the cross section calculation. Due to the uncertainties surrounding the low p_{T} behaviour of $\epsilon_{\text{track}}(\text{e}) \times \epsilon_{\text{match}}(\text{e})$, two different parameterisations will be considered for the cross section calculation. The p_{T} dependent parameterisation describes the observed behaviour, with p_{T} dependence in the p_{T} range 10–30 GeV/c and p_{T} independence above 30 GeV/c. The p_{T} independent parameterisation uses the fit values from Table 6.1 over the entire p_{T} range. The parameterisation used to calculate the value of $\sigma(\text{p}\bar{\text{p}} \to \text{Z}^0).\text{Br}(Z^0 \to \tau^+\tau^-)$ will be decided later. The difference between $\sigma(\text{p}\bar{\text{p}} \to \text{Z}^0).\text{Br}(Z^0 \to \tau^+\tau^-)$ calculated with the p_{T} dependent parameterisation and the p_{T} independent parameterisation will be used as a systematic error.

6.2.2 Measuring $\epsilon_{\text{cal}}(\text{e})$

$Z^0 \to e^+e^-$ events are selected by requiring a well-measured tag electron roughly back-to-back in ϕ with a well-measured test track. Selected events are required to have fired a single electron trigger and the tag electron must match this trigger at all levels. All other electrons in the event are therefore unbiased by the trigger. The efficiency $\epsilon_{\text{cal}}(\text{e})$ is found by seeing what fraction of test tracks are within $\delta R < 0.4$ of a calorimeter electron with the same trigger and calorimeter-based selection cuts as the signal electrons in the $Z^0 \to \tau^+\tau^- \to e^\pm\mu^\mp$ event selection. The δR cut is very loose in order to avoid incorporating the efficiency ϵ_{match}, which forms part of the efficiency measured in the previous section.

Trigger List Used	Fit Value
11	0.739 ± 0.009
12	0.725 ± 0.014
Both	0.733 ± 0.008

Table 6.2: $\epsilon_{\mathrm{cal}}(\mathrm{e})$ values found with p_{T} independent fits to the efficiencies shown in Figure 6.5 in the p_{T} range 10–60 GeV

The tag electron and the calorimeter electron must pass the following cuts

- $|\eta| < 1.1$.

- EM fraction $> 90\%$.

- EM isolation < 0.15.

- H-matrix $\chi^2 < 20$.

- In fiducial region of calorimeter.

The tag electron must have $p_{\mathrm{T}} > 25$ GeV/c and be matched to a track. The test track is required to have $p_{\mathrm{T}} > 10$ GeV/c, at least two SMT hits and at least seven CFT hits. The tag electron and test track must have $\delta\phi > 2$. The p_{T} cut for the test track is low to accommodate signal electrons but this allows QCD background into the selected sample. To reduce QCD contamination, the tag electron and test track are isolated in the central tracker with $\Sigma\mathrm{p}_{\mathrm{T}}^{\mathrm{track}}(0.5) < 1.5$ GeV/c and only events with no jets passing the standard DØ jet cuts are considered.

The calorimeter electron must have $p_{\mathrm{T}} > 10$ GeV/c and is required to match the electron trigger requirements for the eμ trigger used in the current run.

The measured values of $\epsilon_{\mathrm{cal}}(\mathrm{e})$ are plotted against p_{T} in Figure 6.5. The three plots shown correspond to efficiencies measured in data taken with trigger list 11, data taken with trigger list 12 and the entire dataset. There is a slight p_{T} dependence observed and the plots show a p_{T} dependent fit over the p_{T} range 10–60 GeV/c with the fit parameters displayed. p_{T} independent fits have also been applied in the same range and the resulting efficiency values are shown in Table 6.2. For the p_{T} dependent and p_{T} independent fits, the fit parameters from the separate trigger list plots and the
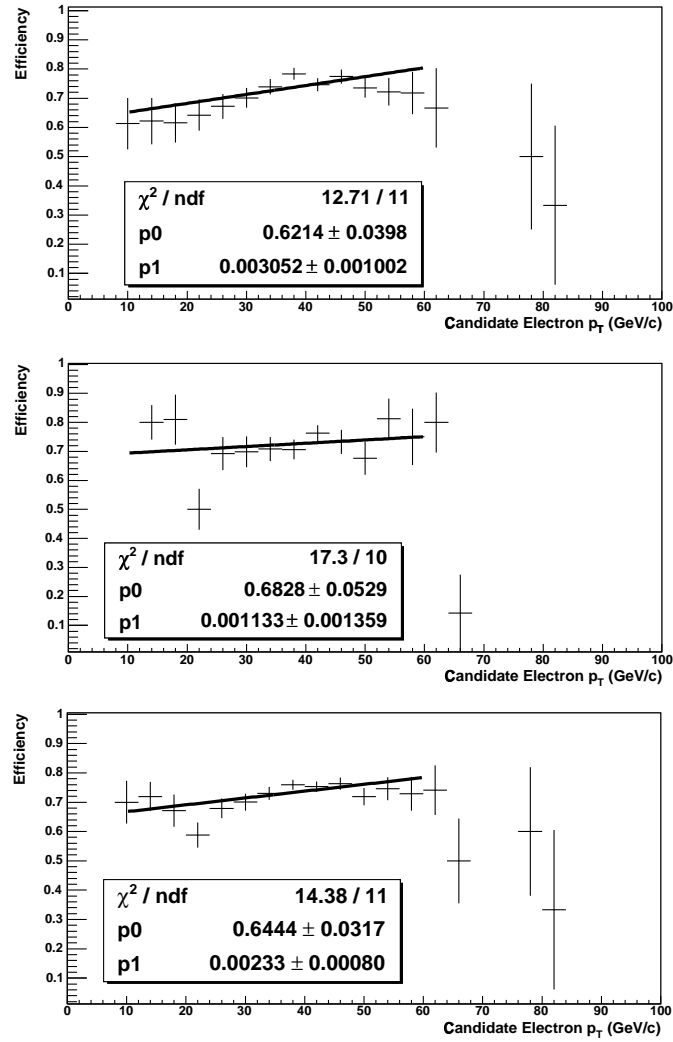
Figure 6.5: $\epsilon_{cal}(e)$ against p_T for data taken with DØ trigger list 11 (top plot), trigger list 12 (middle plot) and both trigger lists (bottom plot).

combined plot agree within errors. The efficiencies evaluated over the entire dataset will therefore be used for the cross section calculation.

There are no suitable cross-checks available for $\epsilon_{\text{cal}}(e)$ in the low p_T range so it is unclear whether the observed p_T dependence is a genuine effect for signal electrons or a result of background contamination in the $Z^0 \rightarrow e^+e^-$ selection. To account for this uncertainty, both p_T dependent and p_T independent parameterisations will be considered for the cross-section measurement. The difference between $\sigma(\text{p}\bar{\text{p}} \rightarrow Z^0).\text{Br}(Z^0 \rightarrow \tau^+\tau^-)$ evaluated with the p_T dependent and the p_T independent parameterisations will be used as a systematic error.

6.2.3 Combining the Electron Efficiencies

Both $\epsilon_{\text{track}}(e) \times \epsilon_{\text{match}}(e)$ and $\epsilon_{\text{cal}}(e)$ have been measured and have been observed to depend on the electron p_T. $\epsilon(e)$ therefore can not be calculated simply by taking the product of these two efficiencies.
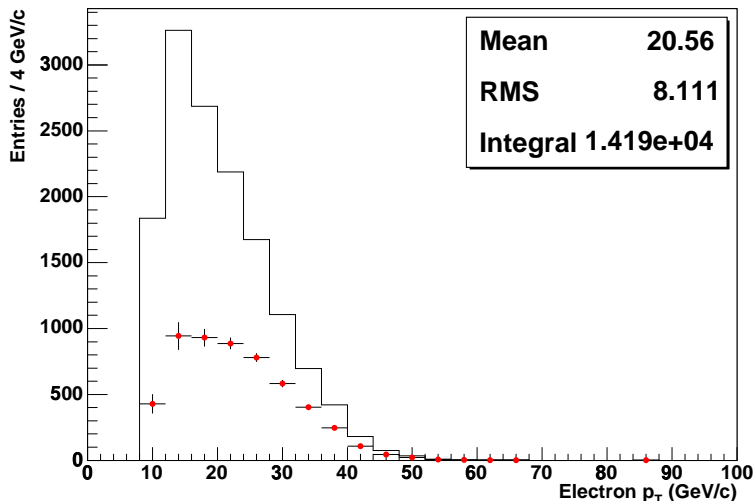
Figure 6.6: Electron p_T from PMCS Monte Carlo $Z^0 \rightarrow \tau^+\tau^- \rightarrow e^\pm\mu^\mp$ events before (histogram) and after (points with errors) bin-by-bin multiplication of measured p_T-dependent signal electron selection efficiencies.

The sample of PMCS Monte Carlo $Z^0 \rightarrow \tau^+\tau^- \rightarrow e^\pm\mu^\mp$ events selected in Section 6.1 is used to produce the signal electron p_T distribution after just the geometrical and kinematic cuts have been applied. This distribution contains 14,186 entries. The p_T distribution is multiplied bin-by-bin with the parameterisations for $\epsilon_{\text{track}}(e) \times \epsilon_{\text{match}}(e)$

and $\epsilon_{\text{cal}}(e)$ and the new number of entries is found. Using the p_T independent parameterisations for both $\epsilon_{\text{track}}(e) \times \epsilon_{\text{match}}(e)$ and $\epsilon_{\text{cal}}(e)$, this number is 8305.5 ± 81.6 entries. The quoted error incorporates the fit parameter uncertainties for the applied efficiencies and the statistical error on the number of entries. The electron p_T distributions before and after multiplying out the p_T dependent electron selection efficiencies are shown in Figure 6.6. The electron p_T distribution after applying the selection efficiencies is a good indication of how the signal electron p_T distribution should look in selected $Z^0 \to \tau^+ \tau^- \to e^\pm \mu^\mp$ events in data.

The overall electron selection efficiency is then found by dividing the number of entries in the electron p_T distribution after the bin-by-bin multiplication by the number of entries beforehand. In the p_T independent case, this gives

$$\epsilon(e) = 0.5855 \pm 0.0076$$

The quoted error does not include the systematic errors from varying the parameterisations of $\epsilon_{\text{track}}(e) \times \epsilon_{\text{match}}(e)$ and $\epsilon_{\text{cal}}(e)$. These will be factored into the cross-section calculation later on.

6.3 Evaluation of the Overall Muon Selection Efficiency

The efficiency $\epsilon(\mu)$ is the efficiency of selecting a muon that satisfies all of the cuts in the $Z^0 \to \tau^+ \tau^- \to e^\pm \mu^\mp$ event selection given that the muon has already satisfied the p_T and muon detector acceptance requirements. As with $\epsilon(e)$, $\epsilon(\mu)$ can be broken down further into three efficiencies.

$\epsilon_{\text{local}}(\mu)$ The efficiency for a muon to produce a triggered muon object of the desired quality in the muon system.

$\epsilon_{\text{track}}(\mu)$ The efficiency for a muon to produce a track of the desired quality in the central tracker.

$\epsilon_{\text{match}}(\mu)$ The efficiency for the local muon to match the central track.

Two samples of $Z^0 \to \mu^+ \mu^-$ events are selected from the same dataset used for the $Z^0 \to \tau^+ \tau^- \to e^\pm \mu^\mp$ selection in order to measure $\epsilon_{\text{track}}(\mu)$ and $\epsilon_{\text{local}}(\mu) \times \epsilon_{\text{match}}(\mu)$.

6.3.1 Measuring $\epsilon_{\text{track}}(\mu)$

A selection of $Z^0 \to \mu^+\mu^-$ events is found by requiring a well-measured tag muon and a test muon that passes all of the cuts from the $Z^0 \to \tau^+\tau^- \to e^{\pm}\mu^{\mp}$ event selection that are measured only in the muon detectors. Information from the central tracker is not used to avoid biasing the measured efficiency. The tag and test muon are required to be roughly back-to-back in ϕ. $\epsilon_{\text{track}}(\mu)$ is then measured as the fraction of test muons that are within $\delta R < 0.5$ of a central track with $p_{\text{T}} > 10$ GeV/c, at least two SMT hits and at least seven CFT hits. Using δR to associate the test muon with a central track avoids using the standard muon track-matching and so $\epsilon_{\text{match}}(\mu)$ is not a factor in this test. $\epsilon_{\text{match}}(\mu)$ will form part of the efficiency evaluated in the next section.

The tag muon is required to be matched to a central track and the track p_{T} must be greater than 25 GeV/c. The test muon is required to be in the full muon detector acceptance and be of medium quality. The same Level 1 muon trigger requirement is applied to the test muon as used in the $e\mu$ triggers. In the $Z^0 \to \tau^+\tau^- \to e^{\pm}\mu^{\mp}$ event selection, the p_{T} of the track matched to the muon is used for the p_{T} cut as it is better measured than the local muon p_{T}. The test muon therefore has no p_{T} cut applied. The tag and test muons must satisfy $\delta\phi > 2$. To avoid QCD background contamination, the tag muon is isolated in the calorimeter with $\Sigma E_{\text{T}}^{\text{cal}}(0.1, 0.4) < 1.5$ GeV/c and in the central tracker with $\Sigma p_{\text{T}}^{\text{track}}(0.5) < 1.5$ GeV/c. The test muon is also isolated in the calorimeter with $\Sigma E_{\text{T}}^{\text{cal}}(0.1, 0.4) < 1.5$ GeV/c. To avoid cosmic ray muons contributing to the sample, the difference in the measured time in the muon A-layer scintillators must be smaller than 10 ns for the tag and test muons.

The muon trigger requirement in the $e\mu$ trigger is the same in both trigger lists used in the $Z^0 \to \tau^+\tau^- \to e^{\pm}\mu^{\mp}$ dataset. $\epsilon_{\text{track}}(\mu)$ is therefore measured over the dataset as a whole. Figure 6.7 shows $\epsilon_{\text{track}}(\mu)$ plotted against the local p_{T} of the test muon. There is no p_{T} dependence and a p_{T} independent fit gives a value of 0.710 ± 0.004 for $\epsilon_{\text{track}}(\mu)$.
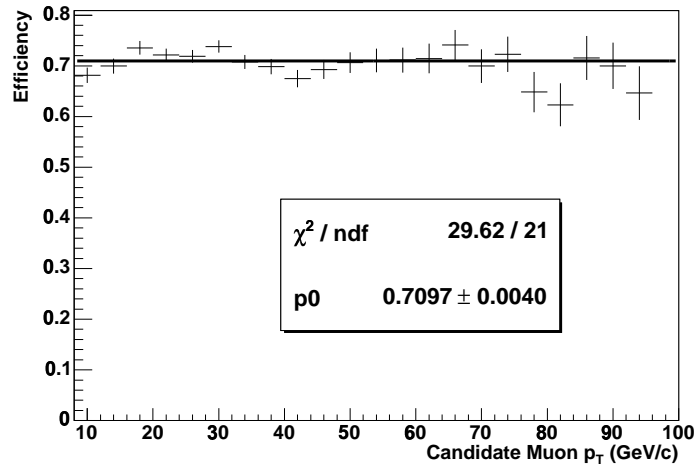
Figure 6.7: $\epsilon_{\text{track}}(\mu)$ plotted against the test muon p_T.

6.3.2 Measuring $\epsilon_{\text{local}}(\mu) \times \epsilon_{\text{match}}(\mu)$

A sample of $Z^0 \to \mu^+\mu^-$ events is selected by finding a well-measured tag muon roughly back-to-back with a test track. Only events firing a single muon trigger are considered and the tag muon is required to match the single muon trigger at all levels. All other muons in the event are therefore unbiased by the trigger. $\epsilon_{\text{local}}(\mu) \times \epsilon_{\text{match}}(\mu)$ is measured by finding the fraction of test tracks that are matched to a local muon passing all trigger and muon system-based cuts for the signal muon in the $Z^0 \to \tau^+\tau^- \to e^{\pm}\mu^{\mp}$ event selection.

The tag muon must be matched to a central track that has a measured $p_T > 25 \text{ GeV}/c$. The test track must have $\delta\phi > 2$ with the tag muon and $p_T > 10 \text{ GeV}/c$. The test track must also have at least two SMT hits and seven CFT hits. To reduce QCD contamination, the tag muon and test track are isolated in the calorimeter with $\Sigma E_T^{\text{cal}}(0.1, 0.4) < 1.5 \text{ GeV}/c$ and isolated in the central tracker with $\Sigma p_T^{\text{track}}(0.5) < 1.5 \text{ GeV}/c$. To reduce background from cosmic ray muons, the measured time of the tag muon in the muon A-layer scintillators must be greater than 7 ns after the time of the $p\bar{p}$ collision. The acolinearity of the test track with the track matched to the tag muon is defined as the difference in ϕ added to the difference in θ between the two tracks. A cosmic ray muon traversing the detector will cause two tracks that are very colinear. To further reduce cosmic ray background, the acolinearity between the track matched to the tag muon and the test track must be greater than 0.05 rads.

$Z^0 \to \tau^+\tau^- \to \mu^\pm + \text{jet}$ is another possible source of background and the test track has a cut of $\Sigma E_T^{\text{cal}}(0.1) < 7$ GeV/c to reduce this contribution.

For a local muon to be matched to the test track, it must be within the full acceptance of the muon detectors and be of medium quality. The local muon must also be matched to a Level 1 muon trigger object matching the muon trigger requirement in the eμ triggers.
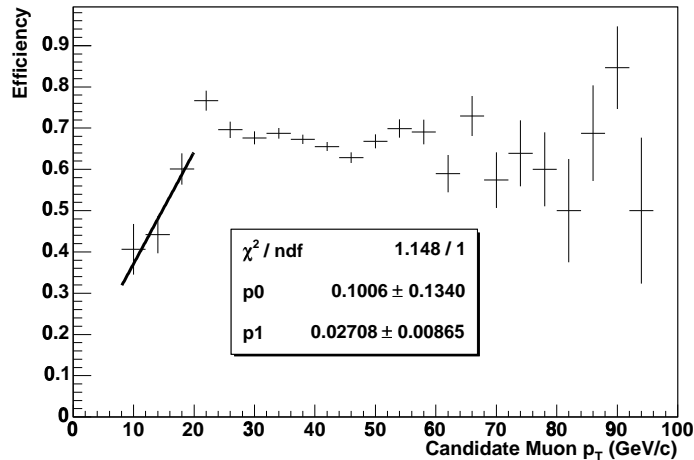
Figure 6.8: $\epsilon_{\text{local}}(\mu) \times \epsilon_{\text{match}}(\mu)$ plotted against the test track p_T.

$\epsilon_{\text{local}}(\mu) \times \epsilon_{\text{match}}(\mu)$ is plotted against the p_T of the test track in Figure 6.8. The measured efficiencies show p_T dependent behaviour at low p_T while the efficiencies in the higher p_T range, corresponding to muons coming from the Z^0 peak, look independent of p_T. A p_T dependent fit to $\epsilon_{\text{local}}(\mu) \times \epsilon_{\text{match}}(\mu)$ in the range 8–20 GeV/c is shown in Figure 6.8. A p_T independent fit in the p_T range 20–60 GeV/c is also performed and the value obtained is 0.672 ± 0.005. As the observed drop in efficiency occurs in the low p_T region, there are no suitable cross-checks for this behaviour currently available.

As with the measured signal electron efficiencies, p_T dependent and p_T independent parameterisations will be considered for the calculation of $\sigma(\text{p}\bar{\text{p}} \to Z^0).\text{Br}(Z^0 \to \tau^+\tau^-)$. The p_T dependent parameterisation will use the measured p_T dependent fit paremeters in the test track p_T range 8–20 GeV/c and the measured p_T independent fit value in the p_T region above 20 GeV/c. The p_T independent parameterisation will use the measured p_T independent fit value over the entire p_T range for the test track. The difference between the calculated values of $\sigma(\text{p}\bar{\text{p}} \to Z^0).\text{Br}(Z^0 \to \tau^+\tau^-)$ using the p_T

dependent and p_T independent parameterisations will be used as the systematic error to account for the uncertainty in the low p_T range.

6.3.3   Combining the Muon Efficiencies
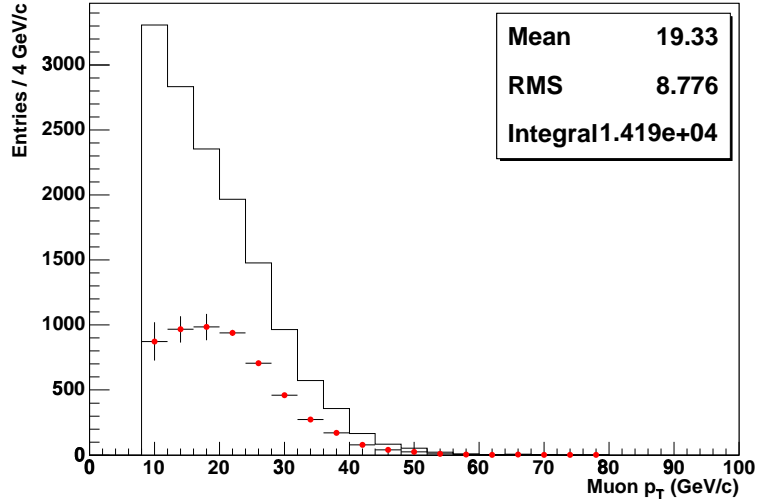
Figure 6.9: Muon p_T from PMCS Monte Carlo $Z^0 \to \tau^+\tau^- \to e^\pm\mu^\mp$ events before (histogram) and after (points with errors) bin-by-bin multiplication of measured p_T-dependent signal muon selection efficiencies.

The technique used to combine the signal electron selection efficiencies by using a p_T distribution from PMCS Monte Carlo will also be used to combine the signal muon selection efficiencies. After applying the geometrical and kinematic cuts described in Section 6.1, a muon p_T distribution containing 14,187 entries is obtained. The p_T independent values of $\epsilon_{local}(\mu) \times \epsilon_{match}(\mu)$ and $\epsilon_{track}(\mu)$ are multiplied bin-by-bin with the muon p_T distribution. The remaining p_T distribution contains 6778.5 ± 62.2 entries. The quoted error takes into account the fit parameter uncertainties for the applied efficiencies and the statistical error on the number of entries. The muon p_T distributions before and after multiplying out the p_T dependent muon selection efficiencies are shown in Figure 6.9. The muon p_T distribution after applying the selection efficiencies indicates the required signal muon p_T distribution in selected $Z^0 \to \tau^+\tau^- \to e^\pm\mu^\mp$ events in data. Dividing the number of entries after applying the bin-by-bin multiplication by the number of entries beforehand in the p_T independent case gives the overall signal muon selection efficiency

$$\epsilon(\mu) = 0.4778 \pm 0.0059$$

The error quoted does not include the systematic error from varying the parameteri-sation of $\epsilon_{\text{local}}(\mu) \times \epsilon_{\text{match}}(\mu)$. This will be taken into account later on.

6.4 Background Contribution to the $Z^0 \rightarrow \tau^+\tau^- \rightarrow$ $e^\pm\mu^\mp$ Data Sample

In order to calculate $\sigma(p\bar{p} \rightarrow Z^0).\text{Br}(Z^0 \rightarrow \tau^+\tau^-)$, it is necessary to estimate the number of background events contributing to the 64.4 ± 12.1 $Z^0 \rightarrow \tau^+\tau^- \rightarrow e^\pm\mu^\mp$ events found in data using the matrix method. As the matrix method estimates the signal sample size by eliminating events with a muon in a jet, the background contribution is expected to come from processes with an electron in a jet and an isolated muon or processes where both the electron and the muon are not in jets, both of which would not bias the conversion factor. Electrons in jets are either genuine electrons or hadrons faking the electron signature in the detector. The considered processes are single W or Z events containing electroweak muon production and an electron in a jet, $W^+W^- \rightarrow e^\pm\mu^\mp$ and $t\bar{t} \rightarrow e^\pm\mu^\mp$.

As the electron track-match is not well-modelled in Monte Carlo, the entire $Z^0 \rightarrow \tau^+\tau^- \rightarrow e^\pm\mu^\mp$ event selection excluding trigger requirements, muon isolation cuts and the electron track-match is applied to Monte Carlo samples for the considered processes. The muon isolation is excluded as the matrix method predicts the number of $Z^0 \rightarrow \tau^+\tau^- \rightarrow e^\pm\mu^\mp$ events in data before the muon isolation cuts were applied. Studies have shown [37] that the fake electron track-match efficiency for electrons in jets in the considered region $|\eta| < 1.1$ is approximately 2%. The number of selected $e^\pm\mu^\mp$ candidates from single W or Z events is normalised to a luminosity of 141.4 pb^{-1} and multiplied by 2% to produce roughly the expected number of events contributing to the $Z^0 \rightarrow \tau^+\tau^- \rightarrow e^\pm\mu^\mp$ signal in data. All processes contribute less than 0.1 events and are considered negligible except for $Z^0 \rightarrow \mu^+\mu^-$ which contributes 0.2 events.

The measured p_{T} independent efficiency $\epsilon_{\text{track}}(e) \times \epsilon_{\text{match}}(e)$ for an electron to produce a track in the central tracker and for the track to be matched to the calorimeter electron was measured in Section 6.2.1 to be 0.798 ± 0.006. The number of selected $Z^0 \rightarrow \tau^+\tau^- \rightarrow e^\pm\mu^\mp$ candidates from $W^+W^- \rightarrow e^\pm\mu^\mp$ and $t\bar{t} \rightarrow e^\pm\mu^\mp$ events is
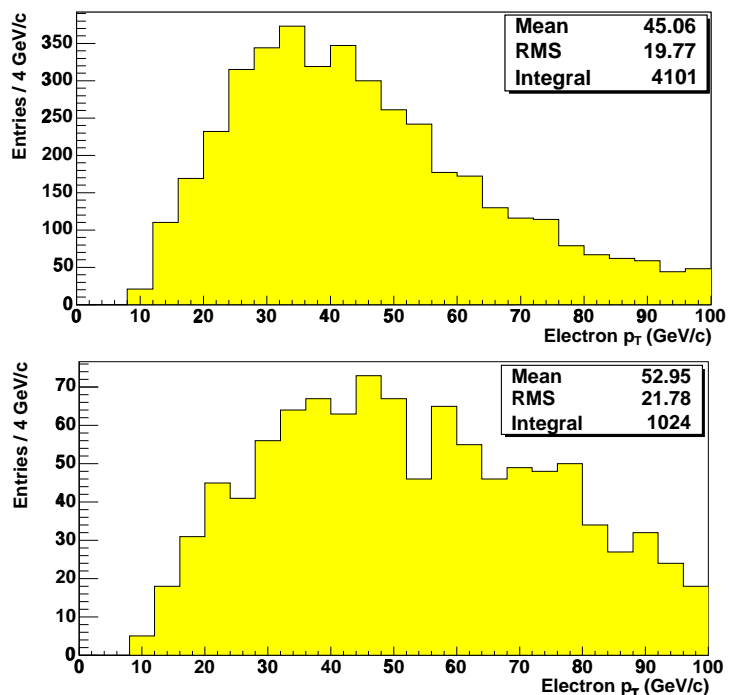
Figure 6.10: Electron p_T from $W^+W^- \to e^\pm\mu^\mp$ (top plot) and $t\bar{t} \to e^\pm\mu^\mp$ (bottom plot) Monte Carlo where events pass the $Z^0 \to \tau^+\tau^- \to e^\pm\mu^\mp$ event selection excluding trigger, muon isolation and electron track-match cuts.

normalised to a luminosity of 141.4 pb^{-1} and multiplied by 0.798 ± 0.006 to give 3.9 ± 1.3 and 2.3 ± 0.7 events respectively. The normalisation is based on current DØ measurements of the W^+W^- [42] and $t\bar{t}$ [43] production cross-sections. The errors on the number of events come mainly from the uncertainties on these cross-section values. The electron p_T distributions in the selected $W^+W^- \to e^\pm\mu^\mp$ and $t\bar{t} \to e^\pm\mu^\mp$ events are shown in Figure 6.10. The muon p_T distributions are not shown as they are very similar. The leptons are shown to be much harder in general than the leptons produced in genuine $Z^0 \to \tau^+\tau^- \to e^\pm\mu^\mp$ events. The trigger efficiencies for the leptons measured in this analysis were evaluated as part of the same efficiency as the lepton identification efficiency in the appropriate DØ subdetector. These efficiencies are therefore inappropriate for correcting the number of selected $W^+W^- \to e^\pm\mu^\mp$ and $t\bar{t} \to e^\pm\mu^\mp$ events for the effects of trigger selection. As the lepton p_T distribution for these processes has been shown to be much harder than in $Z^0 \to \tau^+\tau^- \to e^\pm\mu^\mp$, however, it is acceptable to borrow trigger efficiencies from other studies looking at higher p_T leptons.

The efficiency for triggering an offline muon with $p_T > 15$ GeV/c with the same Level 1 muon trigger requirement as the $Z^0 \to \tau^+\tau^- \to e^\pm\mu^\mp$ event selection is given in [44] as (85 $\pm$ 2.0)% The muon quality cuts used in [44] are looser than those used here so the trigger efficiency will therefore be lower. A value of (92.5 $\pm$ 7.5)% is taken to cover all values higher than the quoted efficiency. The two separate Level 1 electron requirements for trigger lists 11 and 12 are given efficiencies of (97.0 $\pm$ 1.0)% and (96.0 $\pm$ 1.0)% respectively for offline electrons with $p_T > 20$ GeV/c in [45]. A value of (96.5 $\pm$ 1.5) % is used here to take into account the Level 1 electron efficiencies from both trigger lists. Given that an offline electron has passed the Level 1 requirement, the Level 3 efficiency is shown to rise sharply to 100% above the Level 3 p_T threshold. In the eμ triggers, these thresholds are 10 GeV/c and 7 GeV/c so a value of 100 % is assumed. Applying these efficiencies to the number of $W^+W^- \to e^\pm\mu^\mp$ and $t\bar{t} \to e^\pm\mu^\mp$ events gives an expected number of events seen in the $Z^0 \to \tau^+\tau^- \to e^\pm\mu^\mp$ selection of 3.5 $\pm$ 1.2 and 2.1 $\pm$ 0.7 events respectively.

Subtracting the estimated number of $Z^0 \to \mu^+\mu^-$, $W^+W^- \to e^\pm\mu^\mp$ and $t\bar{t} \to e^\pm\mu^\mp$ from the matrix method predicted number of $Z^0 \to \tau^+\tau^- \to e^\pm\mu^\mp$ events in data gives an estimate of the genuine number of $Z^0 \to \tau^+\tau^- \to e^\pm\mu^\mp$ events observed in data of

$$\mathrm{N_{obs}} = 58.6 \pm 12.2$$

The purity of the matrix method estimated $Z^0 \to \tau^+\tau^- \to e^\pm\mu^\mp$ data selection is therefore roughly 91%.

6.5 Calculation of $\sigma(\mathrm{p\bar{p}} \to \mathrm{Z}^0).\mathrm{Br}(Z^0 \to \tau^+\tau^-)$

The selection efficiencies found for electrons and muons are observed to have p_T dependencies at low p_T. It is unclear whether this is a genuine effect for signal leptons or whether this is an effect from background contamination. In order to decide whether to use p_T dependent or p_T independent selection efficiencies to calculate the central value of $\sigma(\mathrm{p\bar{p}} \to \mathrm{Z}^0).\mathrm{Br}(Z^0 \to \tau^+\tau^-)$, comparisons are made between the matrix method estimated p_T distributions for electrons and muons in signal $Z^0 \to \tau^+\tau^- \to e^\pm\mu^\mp$ and the expected p_T distributions mentioned in Sections 6.2.3 and 6.3.3 using p_T dependent and p_T independent selection efficiencies. The expected p_T distributions are

normalised to luminosity using the Standard Model NNLO prediction [46] of

$$\sigma(p\bar{p} \to Z^0).Br(Z^0 \to l^+l^-) = 252 \pm 9 \text{ pb}$$

These comparisons are shown in Figure 6.11. Electron p_T distributions are shown on the left and muon p_T distributions are shown on the right. The expected p_T distributions using p_T dependent selection efficiencies are shown in the top plots and those using p_T independent efficiencies are shown in the bottom plots. For electrons and muons, the comparison using p_T independent efficiencies shows much better agreement than the comparison using p_T dependent efficiencies. The p_T independent efficiencies are therefore used to calculate the central value of $\sigma(p\bar{p} \to Z^0).Br(Z^0 \to \tau^+\tau^-)$. The large uncertainties on the matrix method estimated p_T distributions means that the expected distributions using p_T dependent efficiencies cannot be excluded as possibilities. The systematic error from varying the parameterisation of the selection efficiencies will take this uncertainty into account.
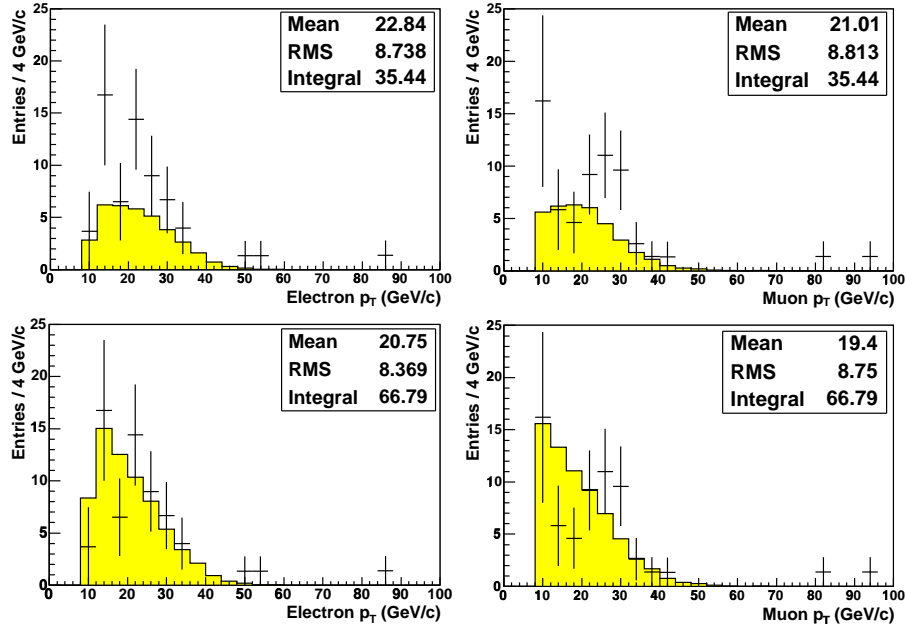
Figure 6.11: Comparison of lepton p_T distribution in signal $Z^0 \to \tau^+\tau^- \to e^\pm\mu^\mp$ estimated by the matrix method (points with errors) with expected lepton p_T distribution from PMCS adjusted for selection efficiencies and normalised to the Standard Model prediction (histogram). Electron p_T (left plots) and muon p_T (right plots) are shown and expected p_T distributions from p_T dependent (top plots) and p_T independent (bottom plots) selection efficiencies are used.

The parameters measured in this chapter and Chapter 5, using p_T independent efficiencies, are summarised in Table 6.3. Substituting these values into Equation 6.4 gives the following result

$$\sigma(\text{p}\bar{\text{p}} \rightarrow Z^0).\text{Br}(Z^0 \rightarrow \tau^+\tau^-) = (221 \pm 46(\text{stat.}) \pm 4(\text{syst.}) \pm 14(\text{lum.})) \text{ pb}$$

where the systematic error comes from all uncertainties involved with the overall acceptance, the statistical error comes from the uncertainty on N_{obs} and the luminosity error is the standard 6.5% luminosity error [15]. The systematic error from varying the parameterisations of the electron and muon selection efficiencies have not yet been been included.

Parameter	Measured Value
N_{obs}	58.6 ± 12.2
$\int \mathcal{L}\text{dt}$	(141.1 ± 9.2) pb^{-1}
A_{gk}	0.00670 ± 0.00006
$\epsilon(\text{e})$	0.5855 ± 0.0076
$\epsilon(\mu)$	0.4778 ± 0.0059

Table 6.3: Measured parameters used to calculate $\sigma.Br$

It is necessary to quantify the uncertainty arising from the p_T dependent behaviour of the electron and muon selection efficiencies at low p_T. Recalculating the central value of $\sigma.Br$ by using the p_T dependent parameterisation for $\epsilon_{\text{cal}}(\text{e})$, $\epsilon_{\text{track}}(\text{e}) \times \epsilon_{\text{match}}(\text{e})$ or $\epsilon_{\text{local}}(\mu) \times \epsilon_{\text{match}}(\mu)$ while maintaining the p_T independent parameterisations for the other efficiencies yields 234 pb, 324 pb and 270 pb respectively. $\sigma.Br$ increases in all cases, suggesting that it would be inappropriate to quote a symmetric systematic error from the central value of 221 pb. Using p_T dependent parameterisations for all three efficiencies, the central value of $\sigma.Br$ is found to be 416 pb. As before, it would be inappropriate to quote a symmetric error from this central value as this is the highest extreme of the $\sigma.Br$ range caused by the p_T dependent behaviour. Taking the values of 221 pb and 416 pb to be the lower and upper extremes of the range of uncertainty, a central value halfway between the two (319 pb) and a symmetric systematic error of half the difference (98 pb) is assumed.

Taking the new central value and combining the systematic error from varying parameterisations with the given systematic error above gives the following result

$$\sigma(\mathrm{p\bar{p}} \to \mathrm{Z}^0).\mathrm{Br}(Z^0 \to \tau^+\tau^-) = (319 \pm 66(\mathrm{stat.}) \pm 98(\mathrm{syst.}) \pm 21(\mathrm{lum.}))\ \mathrm{pb}$$

The statistical and luminosity errors are both proportional to the central value and have been recalculated accordingly. The systematic error for this measurement is large and comes mostly from the uncertainty surrounding the behaviour of the signal lepton selection efficiencies at low p_T. Given more time, it would be interesting to reduce these uncertainties by performing more detailed studies into low p_T leptons. Leptons from the decays of the J/ψ or Υ as well as from the Z^0 may be a good source of information for such a study. The statistical error is also high and this measurement will benefit from running over a larger dataset in the future.

The current best measurement of $\sigma(\mathrm{p\bar{p}} \to \mathrm{Z}^0).\mathrm{Br}(Z^0 \to \tau^+\tau^-)$ at DØ is

$$\sigma(\mathrm{p\bar{p}} \to \mathrm{Z}^0).\mathrm{Br}(Z^0 \to \tau^+\tau^-) = (261 \pm 16(\mathrm{stat.}) \pm 17(\mathrm{syst.}) \pm 16(\mathrm{lum.}))\ \mathrm{pb}$$

measured in the channel $Z^0 \to \tau^+\tau^- \to \mu^\pm +$ anything [49]. The measurement presented here is in agreement both with this value and also with the Standard Model prediction given above. This gives increased confidence in the estimated distributions of p_T and the absolute sum of signed impact parameters in $Z^0 \to \tau^+\tau^- \to e^\pm\mu^\mp$ given by the matrix method in Chapter 5.

Chapter 7

Conclusions

Work on the DØ Silicon Microstrip Tracker between September 2001 and February 2003 has been described in Chapter 3. The efficiency per silicon detector of finding a 1d hit within $5\sigma_{\mathrm{hit}}$ of a track crossing position, ϵ, has been investigated to study the performance of the SMT. It has been found that ϵ is dependent on the displacement of the silicon detector from the nominal interaction point of DØ. The dependency has been shown to come from tracking and be linked to the fraction of track crossings per silicon detector featuring a merged cluster, f_{merged}. This indicates that tracking performance is affected by merged clusters and it is proposed that an algorithm to split clusters be implemented in the future. The values of ϵ presented are reasonably high, indicating good SMT performance, except where problems are observed in the F-disks due to grassy noise.

A study of signed impact parameters in the channel $Z^0 \to \tau^+\tau^- \to e^{\pm}\mu^{\mp}$, undertaken between February 2003 and September 2004, has been presented in Chapters 4, 5 and 6. This work has been shown to depend on accurate vertex measurements and makes a good addition to the work done with the SMT. Using the matrix method, the estimated distributions of p_{T} and the absolute sum of signed impact parameters in signal $Z^0 \to \tau^+\tau^- \to e^{\pm}\mu^{\mp}$ events have been found and shown to be in good agreement with expectation from Monte Carlo. This study indicates that the absolute sum of signed impact parameters may be a useful variable for discriminating back-to-back systems featuring decays with lifetime. This could be used as an additional cut in τ-based analyses.

Using 141.4 pb^{-1} of data collected at DØ at $\sqrt{s} = 1.96$ TeV between 4th October

2002 and 7th September 2003, the production cross-section of the Z^0 boson multiplied by the branching fraction to two τs has been measured to be

$$\sigma(\text{p}\bar{\text{p}} \to \text{Z}^0).\text{Br}(Z^0 \to \tau^+\tau^-) = (319 \pm 66(\text{stat.}) \pm 98(\text{syst.}) \pm 21(\text{lum.})) \text{ pb}$$

in the channel $Z^0 \to \tau^+\tau^- \to e^{\pm}\mu^{\mp}$. This agrees well with current DØ measurements in other channels and the Standard Model predicted value, giving increased confidence in the estimated distributions of p_T and the absolute sum of signed impact parameters in $Z^0 \to \tau^+\tau^- \to e^{\pm}\mu^{\mp}$ given by the matrix method.

Bibliography

[1] G. Hesketh, *A Measurement of the Z^0 Boson Production Cross Section Times Muon Branching Fraction in $p\bar{p}$ Collisions at 1.96 TeV*, Ph.D. thesis, The University of Manchester (2003).

[2] B. R. Martin and G. Shaw, *Particle Physics*, 2nd Edition, John Wiley & Sons (1999).

[3] I. J. R. Aitchison and A. J. G. Hey, *Gauge Theories in Particle Physics*, Adam Hilger Ltd. (1983).

[4] R. K. Ellis, W. J. Stirling and B. R. Webber, *QCD and Collider Physics*, Cambridge University Press (1996).

[5] S. Eidelman et al., *The Review of Particle Physics*, Phys. Lett. **B592** (2004) 1.

[6] S. Mishra, *High Luminosity Operation of the Fermilab Accelerator Complex*, FERMILAB-Conf-03/194 (2003).

[7] *Fermilab's Chain of Accelerators*,
http://www.fnal.gov/pub/inquiring/physics/accelerators/chainaccel.html

[8] D. Adams et al., *The DØ Upgrade Central Fiber Tracker*, DØ Note 4164 (2003).

[9] The DØ Collaboration, *The DØ Detector*, Nucl. Instr. and Methods, A338, 185(1994).

[10] The DØ Collaboration, *The DØ Upgrade: The Detector and Its Physics*, FERMILAB-Pub-96/357-E (1996).

[11] A. Gordeev et al., *Technical Design Report of the Forward Preshower Detector for the DØ Upgrade*, DØ Note 3445 (1998).

[12] J. Kotcher, *Design, Performance and Upgrade of the DØ Calorimeter*, FERMILAB-Conf-95/007-E (1995).

[13] G. C. Blazey, *The DØ Run II Trigger*, FERMILAB-Conf-97/395-E (1997).

[14] M. Begel, *DØ Luminosity in Run II: Online Bookkeeping*, DØ Note 4137 (2003).

[15] T. Edwards et al., *The Updated DØ Luminosity Determination*, DØ Note 4328 (2004).

[16] A. Lo, C. Miao and R. Partridge, *Luminosity Monitor Technical Design Report*, DØ Note 3320 (1997).

[17] DØ Upgrade Collaboration, *DØ Silicon Tracker Technical Design Report*, DØ Note 2169 (1994).

[18] A. Schwartzman and M. Narain, *Primary Vertex Selection*, DØ Note 3906 (2001).

[19] G. F. Knoll, *Radiation Detection and Measurement*, Chapter 11, 2nd Edition, John Wiley & Sons (1989).

[20] K. Anikeev et al., *B Physics at the Tevatron: Run II and Beyond*, FERMILAB-Pub-01/197 (2002).

[21] S. Holmes, *A Practical Guide to Modern High Energy Particle Accelerators*, FERMILAB-Conf-87/160 (1987).

[22] A. Juste, *Silicon Tracker Design*, online presentation:
http://d0server1.fnal.gov/projects/silicon/daqshifters_061101.ppt

[23] M. Narain, *DØ SMT Local Coordinate System and Indexing Scheme*, online presentation:
http://www-d0.fnal.gov/meena/d0_private/silicon/coords/smt-numb/sld001.htm

[24] *SMT Tutorials, Instructions & Docs*, online tutorials:
http://d0server1.fnal.gov/projects/Silicon/www/SMT_files/docs/smt_tutorials.htm

[25] R.Yarema, *A Beginners Guide to the SVXII*, FERMILAB-TM-1892 (1994).

[26] G. M. Guglielmo, M. Litmaath and C. Moore, *DØ Run II Data Distributor Design*, DØ Note 3624 (2001).

[27] H. Fox, *Online Calibration of the DØ Vertex Detector*, online presentation: http://www-d0.fnal.gov/ fox/SmtCalib/SmtCalibWWW.htm

[28] S. Dean, *Users Guide for the SDAQ Browser*, DØ Note 4624 (2004).

[29] S. Dean and G. Hesketh, *d0ve_smt_detail User Guide*, DØ Note 4078 (2003).

[30] F. Lehner, *The phenomenology of the micro discharge effects on DØ silicon modules*, DØ Note 3804 (2000).

[31] A. Bean, J. King, V. Kheyfets, *Silicon Cloud Diffusion Studies in the DØ Monte Carlo*, DØ Note 2268 (2004).

[32] G. Borissov et al., *The P14 Tracker Realignment* DØ Note 4161 (2003).

[33] Brad Abbott for the DØ Collaboration, *DØ Results and Run II Status*, Proceeding for the 9th International Symposium on Heavy Flavor Physics, Pasadena, California, 10-13 Sep 2001, AIP Conf. Proc. 618(1) 57.

[34] Guennadi Borissov, *Beamspot Utilities*, online documentation: http://www-d0.fnal.gov/Run2Physics/ckm/d0_private/tools/beamspot.html

[35] The DØ Collaboration, *Measurement of Inclusive Jet and Dijet Cross Sections in $p\bar{p}$ collisions at $\sqrt{s} = 1.96$ TeV*, DØ Note 4382 (2004).

[36] J. Zhu, *EM Certification Tools*, DØ Note 4171 (2003).

[37] D. Chapin et al., *Measurement of $Z \rightarrow e^+e^-$ and $W \rightarrow e^{\pm}nu$ Production Cross Sections with $|\eta| < 2.3$*, DØ Note 4403 (2004).

[38] B. Tuchming, Private communication (October 2004).

[39] F. Deliot, G. Hesketh and B. Tuchming, Private communication (October 2004).

[40] CDF II Collaboration (D. Acosta et al.) *First Measurements of Inclusive W and Z Cross Sections from Run II of the Tevatron Collider*, E-print number: hep-ex/0406078 (2004).

[41] A. Belyaev, T. Han and R. Rosenfeld $gg \to h \to \tau^+\tau^-$ *at the Upgraded Fermilab Tevatron*, JHEP **0307** (2003) 021,
E-print number: hep-ph/0204210 (2003).

[42] J. Elmsheuser and M. Hohlfeld, *Measurement of the WW production cross section in e^+e^-, $e^\pm\mu^\mp$ and $\mu^+\mu^-$ final states at DØ in Run II*, DØ Note 4231 (2003).

[43] *Measurement of the $t\bar{t}$ production cross section at $\sqrt{s} = 1.96$ TeV in lepton + jets final states using lifetime tagging*, DØ Note 4540 (2004).

[44] E. Nurse and P. Telford *Measurement of $\sigma.Br$ for $Z \to \mu\mu$ in $p\bar{p}$ collisions at $\sqrt{s} = 1.96$ TeV*, DØ Note 4231 (2003).

[45] Top Physics Group of the DØ Collaboration, *DØ Top Analysis and Data Sample for the Winter Conferences 2004*, http://www-d0.fnal.gov/Run2Physics/top/private/winter04/winter04_top_note_v0_3.ps

[46] The Standard Model NNLO expected $\sigma.Br$ value of 252 ± 9 pb is calculated using [47]. The central value uses the MRST2002 NNLO PDFs [48]. The 3.5% uncertainty assessed using the CTEQ6 error PDFs. The LEP value $Br(Z^0 \to l^+l^-) = 0.03366 \pm 0.00002$ is used.

[47] R. Hamberg, W. L. van Neerven and T. Matsuura, *A complete calculation of the order α_s^2 correction to the Drell-Yan K-factor*, Nucl. Phys. **B359** (1991) 343.

[48] A. D. Martin et al., *Uncertainties of predictions from parton distributions. I: experimental errors*,
E-print number: hep-ph/0211080.

[49] C. Galea, S. Nelson, A. Patwa and S. Protopopescu, *Measurement of the production cross section times branching ratio of $Z/\gamma^* \to \tau\tau$ in $p\bar{p}$ interactions at $sqrt(s) = 1.96$ TeV at DØ*, DØ Note 4550 (2004).